Dissertation

submitted to the

Combined Faculties for the Natural Sciences and for Mathematics

of the Ruperto-Carola University of Heidelberg, Germany

for the degree of

Doctor of Natural Sciences

presented by

Diplom-Physicist Christian Maier
born in Lugosch/Romania

Oral examination: December 4th, 2002

Emission Line Galaxies from CADIS: High Redshift Lyman-α Galaxies and Metal Poor Galaxies at Medium Redshift

Referees: Priv. Doz. Dr. Klaus Meisenheimer
Prof. Dr. Immo Appenzeller

Zusammenfassung

In dieser Arbeit werden metallarme Galaxien bei $0.4 < z < 0.7$ und Ly-α Galaxien bei $z > 4.7$ anhand eines Samples von 600 schwachen Emissionsliniengalaxien von dem Calar Alto Deep Imaging Survey (CADIS) gesucht und untersucht. CADIS weist Emissionsliniengalaxien mit Hilfe eines Fabry-Perot-Interferometers in drei Wellenlängenintervallen nach, die in Fenster minimaler Nachthimmelsemission bei 700 nm, 820 nm, und 920 nm platziert sind. Metallarme Galaxien bei $0.4 < z < 0.7$ werden anhand ihrer hohen Flussverhältnisse $[\mathrm{O\,III}]\lambda 5007/[\mathrm{O\,II}]\lambda 3727$ selektiert. Ihre Sauerstoffhäufigkeiten, die durch spekroskopische Nachbeobachtungen bestimmt wurden, zeigen, dass die Metallizität-Leuchtkraft Beziehung, die im lokalen Universum bekannt ist, auch bei $z = 0.6$ Gültigkeit besitzt. Ly-α Galaxien-Kandidaten werden aus dem Emissionsliniensample selektiert, das mehr als 97% Vordergrundgalaxien bei $z < 1.2$ enthält. Die Selektion erfolgt anhand des verschwindenen Flusses unterhalb der Lyman-Kante (kein B Fluss) und dem Nichtvorhandensein einer zweiten Emissionslinie in bestimmten Schmalbandfiltern. Bei zwei Ly-α Kandidaten konnte die Emissionslinie, die im Fabry-Perot gefunden wurde, spektroskopisch bestätigt werden. Der Vergleich der kumulativen Dichten der Ly-α Galaxien von CADIS mit denen von anderen Surveys bei $z > 3$ sowie mit Modellvorhersagen deutet an, dass helle Ly-α Galaxien so selten bei $z > 5$ sind, dass eine sich nicht entwickelnde Population ausgeschlossen werden kann.

Abstract

In this thesis, metal poor galaxies at $0.4 < z < 0.7$ and Ly-α galaxies at $z > 4.7$ have been searched for and investigated in a sample of 600 faint emission line galaxies from four fields of the Calar Alto Deep Imaging Survey (CADIS). Employing an imaging Fabry-Perot interferometer, CADIS detects emission lines in three waveband windows, free of night-sky emission lines, at 700 nm, 820 nm, and 920 nm. Metal poor galaxies at $0.4 < z < 0.7$ have been selected by their high $[\mathrm{O\,III}]\lambda 5007/[\mathrm{O\,II}]\lambda 3727$ ratios. Their oxygen abundances, determined by follow-up spectroscopy, indicate that the metallicity-luminosity relation which applies to galaxies in the local universe also holds at $z = 0.6$. Ly-α galaxy candidates from the emission line sample, which contains more than 97% of objects at $z < 1.2$, are selected by the absence of flux below the Lyman limit (B-band "dropouts"), and the non-detection of secondary emission lines in narrow band filters. For two Ly-α candidates, the emission line detected in the Fabry-Perot has been verified spectroscopically. The comparison of number counts of Ly-α galaxies from CADIS with those of other Ly-α surveys at $z > 3$, and with model predictions, indicates that bright Ly-α galaxies are so rare beyond $z = 5$ that a non-evolving population can be excluded.

Contents

Introduction

The existence and distribution of chemical elements and their isotopes is a consequence of nuclear processes that have taken place during the Big Bang and subsequently in stars and in the interstellar medium (ISM) where they are still ongoing.

During the first 20 minutes after the Big Bang universal cosmological nucleosynthesis at a temperature of the order of 10^9 K created all the hydrogen and deuterium, some ^{3}He, the major part of ^{4}He and some ^{7}Li, leading to primordial mass fractions $X \simeq 0.76$ for hydrogen, $Y \simeq 0.24$ for helium and $Z \simeq 0.00$ for all heavier elements (referred to by astronomers as *metals*). The existence of the latter in our present-day world is the result of nuclear reactions in stars followed by more or less violent expulsion of the products when the stars die.

The first 20 minutes are followed by a period of about 10^5 years during which the universe was radiation-dominated and the baryonic gas, consisting almost entirely of hydrogen and helium, was ionized and consequently opaque to radiation. But the expansion of the universe was accompanied by cooling, and when the temperature was down to a few thousand K (at $z \simeq 1500$), matter began to dominate and first helium and then hydrogen became neutral by recombination. The universe became transparent, background radiation was scattered for the last time, and is now received as black-body radiation with a temperature of 2.7 K. Eventually gas began to settle in the interiors of the pre-existing dark-matter halos, resulting in the formation of galaxies, stars and clusters of galaxies.

After the recombination epoch at $z \simeq 1500$ the universe remained mostly neutral until the first generation of stars and quasars re-ionized the intergalactic medium (IGM) and ended the cosmic *dark ages*. Thus, the first "primeval" galaxies and quasars became visible. In the past few years such galaxies have been detected (by their Ly-α emission) to redshifts up to ≈ 6, when the universe was only a few % of its present age.

Galaxies have a mixture of gas, and diffuse ISM, which consists of gas and dust. Stars inject energy, recycled gas and nuclear reaction products enriching the ISM from which other generations of stars form later. On the other hand, nuclear products may be lost from the ISM by galactic winds or diluted by infall of relatively unprocessed material. The effects of different sorts of stars on the ISM depend on their (initial) mass and whether they are single stars or interacting binaries. Some of the latter are believed to be the progenitors of Type Ia supernovae (SN Ia) which are important contributors to iron-group elements in the galaxies. Massive stars, with initial mass above about $10\,M_\odot$ are short

lived and complete their evolution in less than 5×10^7 yrs. They may eventually explode as Type Ib, Ic or II supernovae, ejecting elements up to the iron group and leading to a neutron star remnant. Some of the most massive stars may collapse into black holes, without an associated SN explosion. Massive stars constitute the main source of oxygen and other α-elements, which are ejected on short timescales. Also significant amounts of carbon and nitrogen are produced in massive stars. Intermediate mass stars, between 1 and $10\,M_\odot$, undergo complicated mixing processes and mass loss in advanced stages of evolution, culminating in the ejection of a planetary nebula while the cores becomes a white dwarf. Such stars are important sources of carbon, nitrogen and heavy elements. Finally, low mass stars ($M<1\,M_\odot$) have lifetimes longer than or comparable to the age of the universe. They contribute little to chemical enrichment or gas recycling, and merely serve to lock up an increasing fraction of material. On the other hand, they contribute to light and have imprinted in their chemical composition the conditions of the ISM at the time and place they have formed. The result of all these processes is that the Sun was born ~ 4.7 Gyrs ago (at $z \approx 0.4$) with mass fractions $X \simeq 0.70$, $Y \simeq 0.28$, $Z \simeq 0.02$.
The main goal of the **C**alar **A**lto **D**eep **I**maging **S**urvey (CADIS) is to find primeval galaxies at $\gtrsim 4.7$ by their Ly-α emission; from the Lyman-α lines of these galaxies one can infer star formation rates. CADIS finds also emission line galaxies at medium redshift ($0.2 < z < 1.2$); from their emission line ratios, metal abundances can be calculated. Since star formation and metal production are directly correlated, the study of emission line galaxies from the CADIS survey can offer clues about the history of chemical enrichment in the universe, both at high and medium redshift.

The Emission Line Survey of CADIS

1.1. Introduction

The **C**alar **A**lto **D**eep **I**maging **S**urvey (CADIS, see Meisenheimer et al. 1998) has been established in 1996 as the extragalactic key project of the Max-Planck Institut für Astronomie in Heidelberg. It combines a moderately deep multi-band survey ($10\,\sigma$ limit, $R_{lim} = 24$) with an emission line survey employing an imaging Fabry-Perot-Interferometer ($F_{lim} = 3 \cdot 10^{-20} Wm^{-2}$). The multi-band survey (see Wolf et al. 2001), with four broad-band filters B, R, J and K' plus 12 medium-band filters from 400 nm to 1000 nm, practically resembles low-resolution imaging spectroscopy (see Fig. 1.1, left).
This thesis will focus on the emission line survey of CADIS. Therefore, this chapter will address in detail the observational, data reduction and analysis aspects relevant to the study of emission line galaxies.

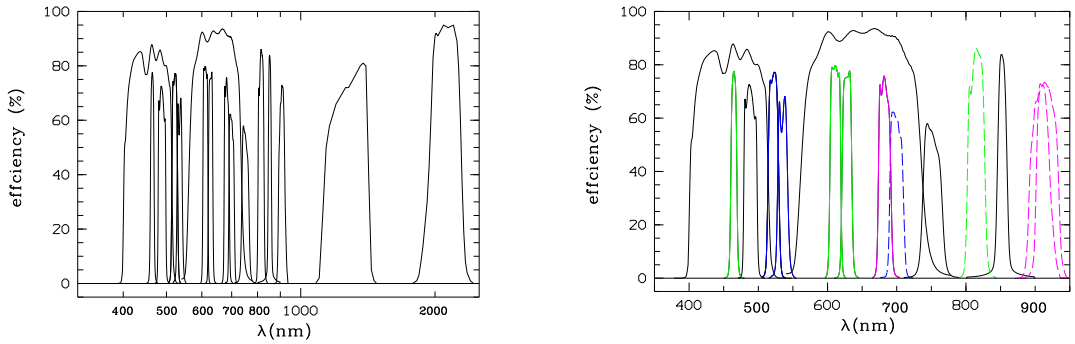

Figure 1.1 The CADIS filter set
Left panel: The complete optical and near-infrared CADIS filter set
Right panel: Optical broad and medium band filters: blue = pre-filter FP-A + veto-filter; green = pre-filter FP-B + veto-filter; magenta = pre-filters FP-C + veto-filter

1.2. CADIS Fields

The observations were performed on a number of fields at high galactic latitude ($|b| > 40°$). All CADIS fields are placed in zero-reddening areas, i.e. local minima of the IRAS $100\,\mu$m maps with undetected fluxes, which should limit the (galactic) extinction to $A_V < 0.1$. Each field position was also selected so that the central square of the field of $12 \times 12\,\square'$ contains no bright ($R \lesssim 15$) star or galaxy. We also excluded the position of known galaxy clusters. At present four (out of six) of the CADIS emission line survey fields are complete

observed and (almost) fully analysed. Coordinates and characteristics of these fields are given in Tab. 1.1. A seventh field, on the North Ecliptical Pole (NEP), is only used for the multi colour survey.

Table 1.1 CADIS fields. The observed and analysed FP-windows are indicated in bold.

Field	FP-Window	Center coordinates		Area
name	observed	$\alpha(2000)$ $(h\,m\,s)$	$\delta(2000)$ $(^\circ\ '\ '')$	$\square'$
01h	A, **B**, C	01 47 33.3	02 19 55	105
09h	**A, B, C**	09 13 47.5	46 14 20	98
10h	B	10 52 05.1	57 25 24	100
13h	A, C	13 47 42.3	05 37 34	100
16h	A, **B**, C	16 24 32.3	55 44 32	107
23h	**A, B, C**	23 15 46.9	11 27 00	103

1.3. Observations

In order to detect emission line objects, narrow band observations were done in three wavelength windows, which are relatively free from OH night-sky emission. In each of these windows, observations have been performed with a scanning Fabry-Perot-Interferometer (FPI) at 8 or 9 equally spaced wavelength steps, thus providing a spectral line scan over an interval of $12 - 15$ nm (henceforth called FP scan). The three wavelength windows are specified by A, B, and C, and are located at:
window FP-A : $\lambda = 702 \pm 6$ nm,
window FP-B : $\lambda = 820^{+4.5}_{-6}$ nm,
window FP-C : $\lambda = 918^{+10}_{-8}$ nm.
For selecting the correct interference order of the FPI, pre-filters with FWHMs of ~ 20 nm are used (see Fig. 1.1, right). FP-A and FP-C have been fine-tuned in such a way that for an Hα line falling in one of the wavelength settings of C, the corresponding [O III] $\lambda\,5007$ line should show up exactly in the corresponding setting of interval A for a galaxy at $z \approx 0.4$. This is very helpful for identifying emission line galaxies at this redshift (see for example object 09h-5068 in Fig. 1.2).
The FP observations in the B window were carried out with the CAFOS focal reducer at the 2.2-m telescope on Calar Alto, Spain; those in the A and C windows were carried out with the MOSCA focal reducer installed at the 3.5-m telescope at Calar Alto[1]. For a test concerning the search for Ly-α galaxies (see chapter 3), FP observations in window B in the 01h field were carried out as well with CAFOS as with MOSCA. Both focal reducers are equipped with Fabry-Perot (Queensgate) etalons in the parallel beam, with free apertures of 50 and 70 mm, and with air gaps of $\sim 8\,\mu$m. By choosing the appropriate interference order, the spectral resolving power for both etalons was set, to $\sim 750\,\mathrm{km\,s^{-1}}$. The actual spectral resolutions used were 1.8, 2.0, and 2.4 nm. Four prefilters with central

[1] For details concerning CAFOS and MOSCA see http://www.caha.es/CAHA/Instruments/index.html

wavelengths of 702 nm, 815 nm, 909 nm, and 916 nm were used for the three windows A, B, and C. Exposures were also done with the pre-filters alone in order to measure the continuum level surrounding emission lines found in the FP scans. At the 2.2-m telescope a flux limit of $F_{lim} = 3 \times 10^{-20}\,\mathrm{W\,m^{-2}}$ can be achieved after 3 hours of integration under typical conditions (seeing of $\sim 1''.4$), sufficient to detect the Lyman-α emission of a primeval galaxy with a star-forming rate (SFR) of $\sim 10\,\mathrm{M_\odot\,y^{-1}}$ at high redshift.
In order to decide which emission line was detected in the FP scan, we placed for each FPI band a set of medium band filters at wavelengths where secondary prominent lines would appear. Since these filters can exclude certain line classifications - e.g., the presence of a line in any of these filters excludes that the line detected in the FP scan is [O II] λ3727 or Lyα - they are named "veto" filters. For example, for the galaxy 16h-4908 in Fig. 1.2, an emission line is detected in FP-B. This line cannot be Ly-α or [O II] λ3727, since the [O II] λ3727, Hβ, and [O III] λ5007 lines show up in the veto filters V465, V611 and V628, and therefore the line seen in FP-B can be identified as Hα at $z = 0.25$. The veto filters (shown in Fig. 1.1, right) are part of the set of 16 medium and broad band filters, ranging from 400 to 2200 nm in wavelength, which provide additional information about the spectral energy distribution (SED) of the line emitter and its spectral type. One of the veto filters for C, V522, is the same as for FP-A, and another veto filter for C is provided by FP-A itself. Table 1.2 lists the redshift bins for emission lines detected in FP-A or FP-B, and the filters where the secondary lines are expected.

Table 1.2 Emission lines detected by CADIS in FP-A or FP-B, and corresponding (veto) filters for measuring their fluxes. Filter specifications are noted in term of *central wavelength / full width at half maximum*, both given in nm. [S II] denotes [S II]λ6721, [OIII] the [O III] λ5007, and [OII] the [O II] λ3727 line. As an example, if Hα is detected in FP-B, at about 820 nm, the [O III] λ5007, Hβ, and [O II] λ3727 lines show up in the veto filters V628, V611, and V465, specified as 628/17, 611/16, and 465/9.

redshift bin	FP line	FP Window	Filter used to observe				
			Hα	[OIII]	Hβ	[OII]	Lyα
0.210-0.226	[S II]	820 nm	-	611/16	-	-	-
0.240-0.257	Hα	820 nm	FP-B	628/17	611/16	465/9	-
0.392-0.415	[O III]	702 nm	909/30	FP-A	-	522/16	-
			+ FP-C				-
0.430-0.458	Hβ	702 nm			FP-A	535/14	-
0.625-0.648	[O III]	820 nm	-	FP-B	-	611/16	-
0.674-0.697	Hβ	820 nm	-	-	FP-B	628/17	-
0.870-0.901	[O II]	702 nm	-	-	-	FP-A	-
1.183-1.214	[O II]	820 nm	-	-	-	FP-B	-
4.732-4.826	Lyα	702 nm	-	-	-	-	FP-A
5.690-5.785	Lyα	820 nm	-	-	-	-	FP-B

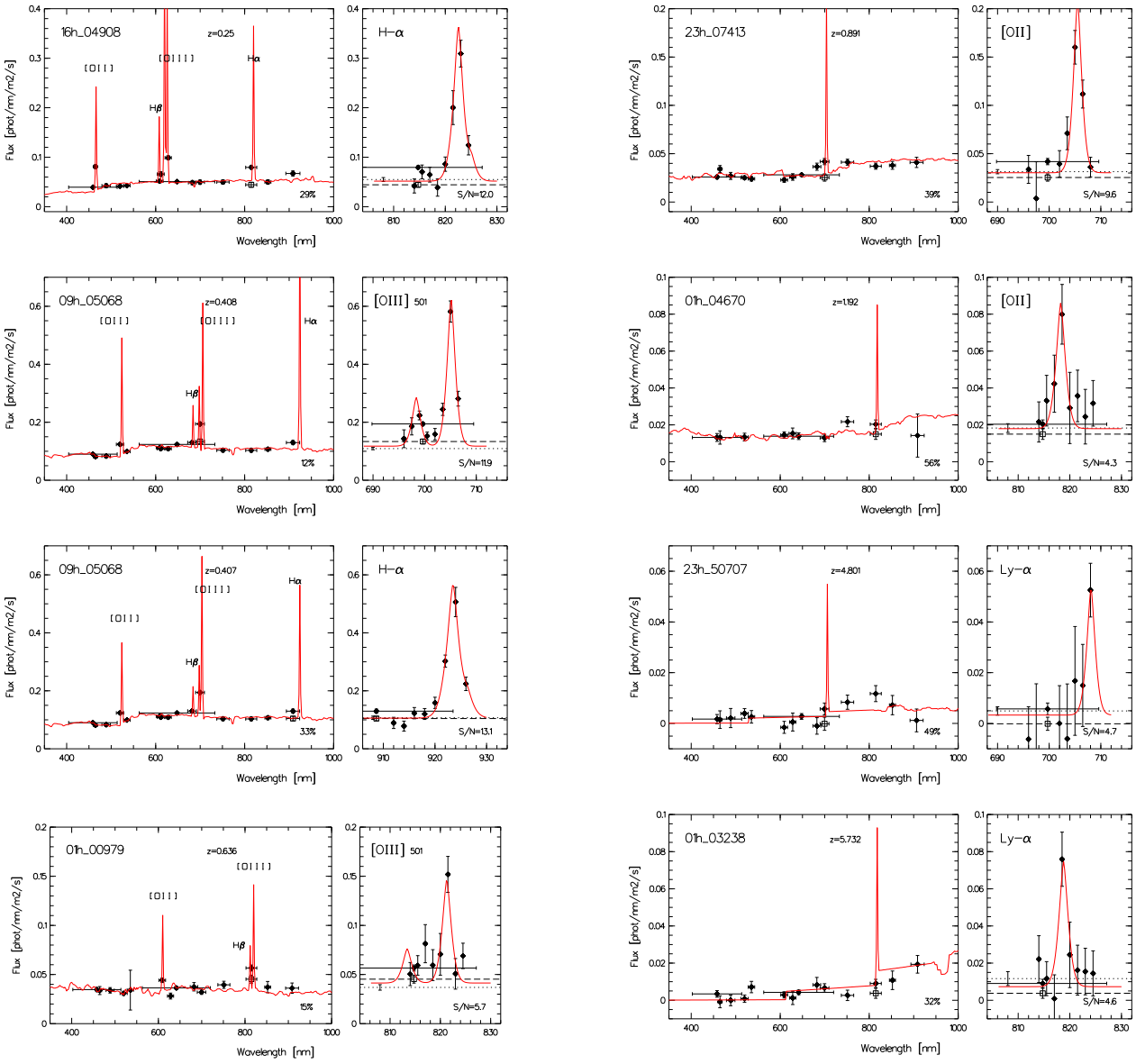

Figure 1.2 Examples of spectra of CADIS emission line galaxies. Photometry in all 14 optical CADIS filters fitted by a continuum-model is showed in the left panels, and the Fabry-Perot measurements with emission line fits to the observed flux data in the right panels, for galaxies from redshift 0.250 (top left) to redshift 5.732 (bottom right). For each line identification the fit to the continuum spectrum also provides a new continuum level at the wavelength of the FP window, which is marked in each of the line plots as a dotted horizontal line; the dashed lines mark the level of the continuum after the emission line flux has been subtracted from the pre-filter (see details in section 1.7). The numbers in the lower right edges of the right panels specify the signal-to-noise ratios, F_{line}/σ_{line}; F_{line} and σ_{line} are derived by fitting the Fabry-Perot instrument profile to the observed flux data points.

1.4. CADIS Data Reduction and Photometry

The CADIS data analysis is described in detail in Meisenheimer et al. (2002). Therefore I address here in detail only aspects relevant to emission line galaxies.
Special care has to be taken with the flat field correction of Fabry-Perot data. The insertion of the Fabry-Perot Etalon into the parallel beam of the focal reducers CAFOS and MOSCA introduces internal reflections, which may be distributed unevenly across the field; in fact, in CAFOS reflections at the etalon produce a bump of 20% in the central part of the field. On the other hand, the transmission characteristic through the combination Etalon + pre-filter is also radially dependent due to the change in transmitted wavelength with distance from the optical axis. Therefore, a direct measure of the transmission pattern is required. To this end, we introduce a mask with about 1000 holes into the focal plane in front of the focal reducer. Flat field exposures through this mask with constant illumination pattern both with the pre-filter alone and pre-filter + Etalon (tuned to the wavelength of the science exposure) allow then a point-wise description of relative transmission introduced by the Etalon, as ratio of the intensity contained in the images of each hole. The interpolation between the points results in the transmission pattern, $R(\lambda)$. However, also the fine structure of the flat fields through the narrow-band Fabry-Perot differs from that of the pre-filter due to interference fringes arising at the surface of the CCD detector. This fine structure is taken into account by dividing a dome flatfield taken through the Etalon, $D(\lambda)$, by a median filtered version of itself, $\mathsf{smooth}\_D(\lambda)$.
Altogether, the flat field for each wavelength setting of the Fabry-Perot Etalon, $FF(\lambda_i)$, is constructed as follows:

$$FF(\lambda_i) = \mathsf{smooth}\_TWI_{pf} \frac{D(\lambda_i)}{\mathsf{smooth}\_D(\lambda_i)} R(\lambda_i), \tag{1.1}$$

where smooth_TWI_{pf} is a median-filtered version of a twilight flat field through the pre-filter alone. The frame $FF(\lambda_i)$ is treated as a standard flat field for all science frames taken at the wavelength setting λ_i.
In summary, the data reduction includes bias subtraction, flatfielding, and removal of cosmic ray events and detector defects by overlaying dithered images, and by replacing the bad pixels by the kappa-sigma-clipped mean of pixel values in the other images.
After overlaying all images to the same world coordinate system, the images *for each wavelength setting and filter* are then summed. For each of these stacked sum frames the object search engine SExtractor (Bertin & Arnouts 1996) is applied, with thresholds adjusted to their seeing and exposure depth. The object positions are corrected for the distortion of the camera optics, and the lists from single-band detections are merged into one common "masterlist" with averaged positions. For merging, all objects are considered to be identical which fall into a common error circle of $1''$ radius.
The morphology parameters of an object are determined on the sum frame, where the object shows the highest signal-to-noise ratio, using the photometry package MPIAPHOT (Meisenheimer & Röser 1993). The photometry is performed on each individual frame, and we get an optimum signal-to-noise ratio by integrating the photons at the centroid object positions, with a Gaussian weight distribution, the width of which is determined such that the convolution of the seeing PSF with the weight function results in a common PSF for all frames. The obtained flux is then calibrated by tertiary spectroscopic standard

stars established in each CADIS field. For these standard stars we know the physical fluxes in every CADIS filter, and therefore the calibration of each image is independent of the photometric conditions during the exposure. Finally, the single frame flux values are S/N-weight averaged with errors derived from the counting statistics and from the scatter of the individual fluxes between the single images. Since the photometry weight function is normalized to give correct fluxes for stellar objects, the total fluxes of extended objects are underestimated, and need a correction factor according to their morphological parameters. The photometry in the narrow FP-bands is checked on diagrams in which the flux ratio $\bar{F}(\lambda_{FP})/\bar{F}(prefilter)$ is plotted as a function of magnitude for stellar objects (see example in Fig. 1.3). Obviously, the narrow (bright) end of the trumpet-shape distribution should fall close to the $\bar{F}(\lambda_{FP})/\bar{F}(prefilter) = 1$ line as the wavelength range covered by the FP scan is very small, and stellar spectra are rather flat around $\lambda = 700$, 815 and 920 nm. Since the analysis of the emission line objects depends on the assumption that a pure continuum object shows $\bar{F}(\lambda_{FP}) = \bar{F}(prefilter)$, we carry out an *a posteriori* re-calibration of the FP bands by adjusting the FP fluxes, at most by 5%.

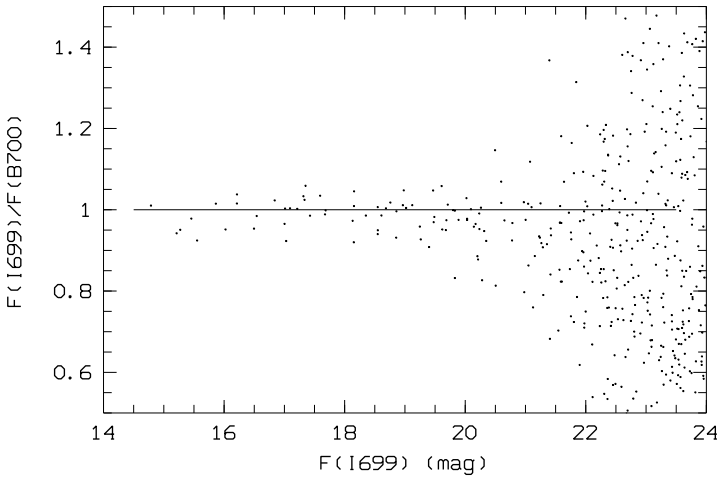

Figure 1.3 $\bar{F}(I699)/\bar{F}(B700)$ as a function of magnitude for stellar objects in 09h-field.

The CADIS data reduction and photometry ends in a photometrically calibrated catalogue, in which – for each survey field – the measured fluxes of all detected objects are combined. This final "flux table" serves as input for the scientific data analysis in which every object is classified either on the basis of its multi-colour information or from the detection of an emission line in one of the FP scans.

1.5. Selection of Emission Line Galaxies

The selection of emission line galaxy candidates is based on the fluxes in the FP images and in the pre-filter image. Candidates have to fulfill three criteria:

(S1) For at least one FP wavelength, the signal has to be larger than the upper limit F_{lim}/σ of the noise distribution, typically located near 5σ (see Tab. 1.3),

(S2) The signal-to-noise ratio of the line feature in the FP scans above the prefilter flux is higher than ~ 2.5, equivalent to about $2 \times 10^{-20}\,\mathrm{W\,m^{-2}}$, and

(S3) Objects have $F_{line}/\sigma_{line} > K_{line}$, where F_{line} is the emission line flux.

This procedure, which is described in detail in the following, yields a few hundred emission line galaxy candidates per field (see Tab. 1.3).
(S1) First a careful analysis of the blank sky noise in the FPI data is done in order to place a reasonable detection limit to each field and Fabry-Perot interval. The detection of an emission line in one of the FP-bands λ_i requires that the object exhibits a significant flux:

$$\bar{F}(\lambda_i) \geq \eta_f \cdot \hat{\sigma}(\lambda_i), \tag{1.2}$$

where $\bar{F}(\lambda_i)$ denotes the highest flux measured in all FP-bands of the respective window (A, B or C), and $\hat{\sigma}(\lambda_i)$ is its true overall error which takes into account both the calibration error and the scatter of the flux between the individual images. The appropriate significance level η_f is determined from the noise distribution as measured on "blank" positions on the sky. Objects with a pre-filter flux less than 1σ are selected, excluding objects identified as stars or reflections. For each such object and Fabry-Perot interval the histogram of $\bar{F}(\lambda_i)/\hat{\sigma}(\lambda_i)$ (denoted as F_{FPI}/σ_F in Fig. 1.4) is fitted by a Gaussian. The limiting value of $\eta_f = F_{lim}/\sigma$ is the value above which only 1 object/$[\Delta(F_{FPI}/\sigma_F) = 0.1]$ is detected as blank sky noise. η_f is determined for each field and FP window separately, and its values are given in Tab. 1.3.
Since the FP scans are sparsely sampled (distance between two adjacent wavelength settings $\delta\lambda_{ij} \simeq 0.8\Delta\lambda$, where $\Delta\lambda$ is the FWHM of the transmission), the requirement expressed by equation 1.2 misses those objects where the emission lines fall in between two adjacent settings $\lambda_i,\ \lambda_j$. In order to recover them, we also select objects which exhibit significant flux when averaging over each two adjacent settings $\lambda_i,\ \lambda_j$:

$$\bar{F}(\lambda_i, \lambda_j) \geq \eta_f \cdot \bar{\sigma}(\lambda_i, \lambda_j), \tag{1.3}$$

with

$$\bar{F}(\lambda_i, \lambda_j) = \tfrac{1}{2}(\bar{F}(\lambda_i) + \bar{F}(\lambda_j)), \text{ and}$$
$$\bar{\sigma}(\lambda_i, \lambda_j) = \tfrac{1}{2}\sqrt{(\hat{\sigma}^2(\lambda_i) + \hat{\sigma}^2(\lambda_j))}.$$

(S2) An *emission line* object must also show a significant line flux *above* the continuum level:

$$S_{line}(\lambda_i) \equiv \frac{\Delta\lambda}{1 - \Delta\lambda/\Delta\lambda(prefilter)}[\bar{F}(\lambda_i) - \bar{F}(prefilter)] \tag{1.4}$$

(measured in photon $\mathrm{m^{-2}\ s^{-1}}$), where the prefilter flux $\bar{F}(prefilter)$ serves as continuum measure, and $\Delta\lambda$ is the width of the FP transmission. The factor $\frac{1}{1-\Delta\lambda/\Delta\lambda(prefilter)}$ accounts for the fact that the emission line is contained in the prefilter, and has to be subtracted in order to get the *true* continuum level. Since $\Delta\lambda(prefilter) > 10 \times \Delta\lambda$, the expression

$$\sigma_{line}(\lambda_i) \equiv \Delta\lambda\sqrt{\hat{\sigma}^2(\lambda_i) + \hat{\sigma}^2(prefilter)}$$

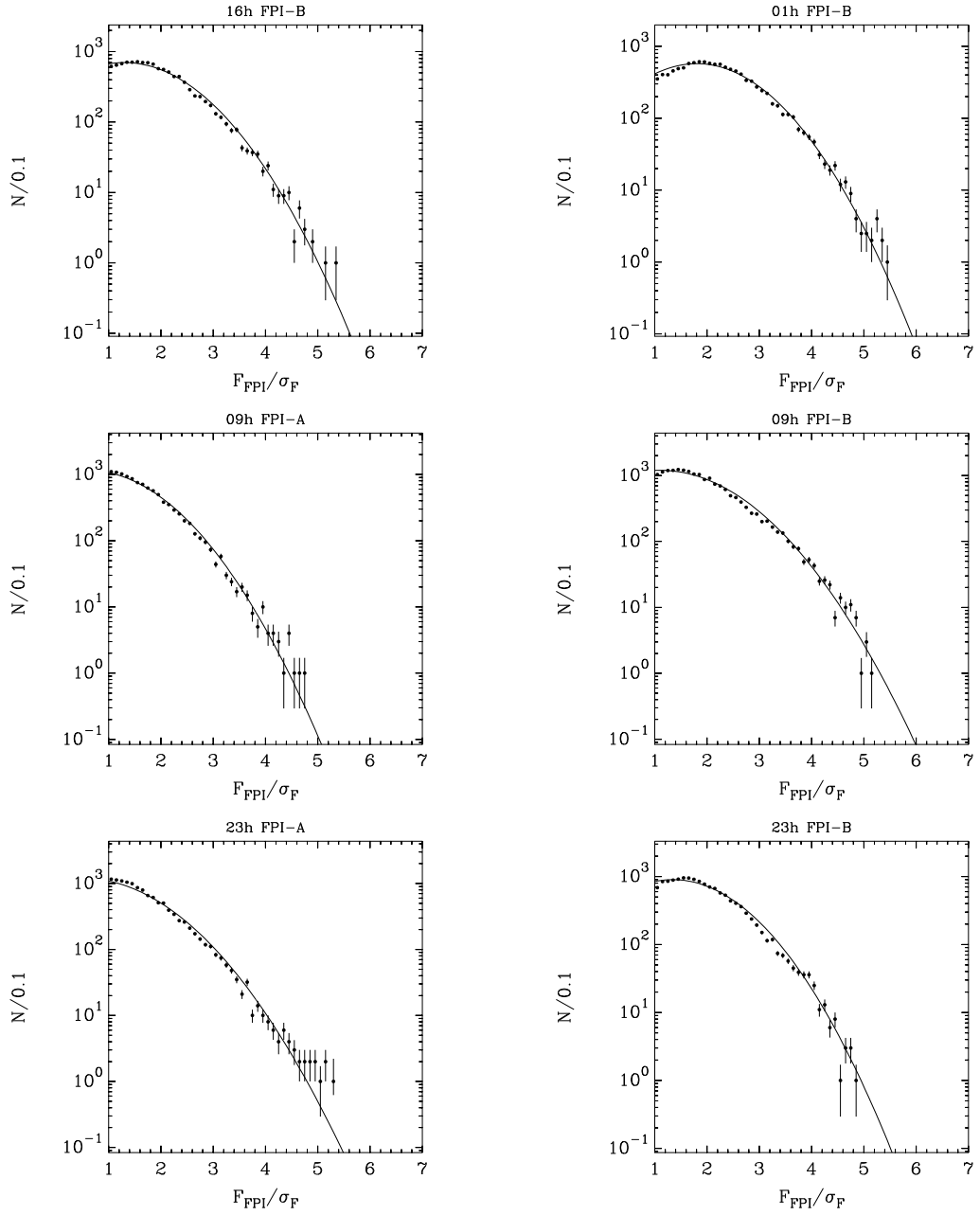

Figure 1.4 Distribution of Fabry-Perot flux significance in apertures measuring blank sky for 01h-field FP-B ($F_{lim}/\sigma = 5.3$), 09h-field FP-A ($F_{lim}/\sigma = 4.5$), 09h-field FP-B ($F_{lim}/\sigma = 5.5$), 16h-field FP-B ($F_{lim}/\sigma = 5.1$), 23h-field FP-A ($F_{lim}/\sigma = 4.6$) and 23h-field FP-B ($F_{lim}/\sigma = 5.0$).

provides a sufficiently accurate estimate of the (statistical) error of $S_{line}(\lambda_i)$. A significant line detection can therefore be secured by demanding

$$S_{line}(\lambda_i) \geq \eta_{line} \cdot \sigma_{line}(\lambda_i). \tag{1.5}$$

We choose a relatively low significance level $2.5 \leq \eta_{line} \leq 3.0$ in order not to miss any faint emission line objects before a proper analysis of the emission line flux, which is based on a *line fit* (see section 1.7). In order to illustrate η_f and η_{line} consider the faint galaxy 01h-00979 in Fig. 1.2 for which $\eta_{line} = 5.7$ and $F(821.5\,nm)/\hat{\sigma}(821.5\,nm) = 9.1$, which is larger than $\eta_f = 5.3$.
(S3) For the final selection of emission line galaxies, we choose objects with $F_{line}/\sigma_{line} > K_{line}$. F_{line} and σ_{line} are derived by fitting the Fabry-Perot instrument profile to the observed flux points (see section 1.7; for example the object 01h-00979 in Fig. 1.2 has $F_{line}/\sigma_{line} = 5.7$). Follow-up spectroscopy of CADIS emission line candidates (section 1.10.1) showed that $K_{line} = 3.8$ yields a (very) save choice of emission line objects.

Table 1.3 Number of CADIS found emission line galaxies (N_{Elgal}) in each field and FP-interval with the criteria described in the text ($K_{line} = 3.8$).

Field	FPI	$\Delta\Omega$ ($\Box'$)	$F_{lim}(Wm^{-2})$	F_{lim}/σ	N_{Elgal}
01h	B	104.9	$3.0 \cdot 10^{-20}$	5.3	105
09h	A	98.3	$3.0 \cdot 10^{-20}$	4.5	90
09h	B	98.3	$3.5 \cdot 10^{-20}$	5.5	92
16h	B	106.5	$3.2 \cdot 10^{-20}$	5.1	108
23h	A	102.8	$3.5 \cdot 10^{-20}$	4.6	67
23h	B	102.8	$3.5 \cdot 10^{-20}$	5.0	152

1.6. Rejection of Reflections and M Stars

Due to **reflections** within the CAFOS Fabry-Perot etalons employed in CADIS, bright objects, mostly stars, are accompanied by features about 6 magnitudes fainter than the bright object, and appear at a fixed offset position ($41''$) away from it. Since in the pre-filter images no object should be seen at the same positions, these ghosts can be easily sorted out and rejected from the candidates list. Another type of ghost on the single FP frames is produced by reflections of bright objects between the FP etalon and the pre-filter. These ghosts appear symmetrically with respect to the optical axes and, due to dithering, the ghosts appear at different positions in every frame. Thus the ghosts are easily identifiable and already strongly suppressed by the correction for cosmic rays in the standard data reduction.
The strong absorption bands in the spectra of **M stars** can mimic emission lines. Particularly, VO and Na absorption lines in the wavelength range 800 to 850 nm can affect measurements in FP window B. M stars show rising spectra to longer wavelengths. Therefore, in order to select emission line objects which can possibly be M stars, objects showing a line in FP-B and a higher flux in the pre-filter B909 than in R filter are selected; respectively, objects with a line detected in FP-A and a higher flux in the pre-filter B815 than in R filter are selected, too. From this group of objects, those classified as "star" by the multi-colour classification are rejected. Also objects where none of the FP-measurements in FP-B (FP-A) show a higher flux than the flux in B909 (B815) are identified as M stars,

since in this case the emission line in FP-B (FP-A) is simulated by strong absorption bands.

1.7. Line Fits

The pre-selection of emission line galaxies (steps (S1) and (S2)) takes into account only a first guess of the continuum level from the pre-filter flux. For a proper assessment of the line flux above a best-guess continuum level, one needs to perform proper *line fits* and to determine the continuum level more reliably by taking not only the prefilter flux but also the overall SED, determined by the multi-filter observations, into account. This has to be carried out in an iterative way consisting of the following three steps:

(LF1) Line fit on the basis of the first guess continuum derived from the prefilter flux;

(LF2) Use fit (LF1) to subtract the line contribution from the prefilter flux and perform a second line fit constrained by this improved continuum;

(LF3) Take both the continuum level from the prefilter and the global SED in the vicinity of the emission line into account when performing a final line fit. Use the parameters of this fit (and their errors) to establish a final "significance level" for the emission line and select reliable emission line galaxies on that basis.

Details of the three steps are as follows.
(LF1) First the measured flux densities $\bar{F}(\lambda_i)$ in an FP-scan are converted to an excess value above the continuum from the pre-filter image. Then the analysis of the FP data is done by line fitting. The width of the line profiles are fixed to the width of the instrumental profile (1.8, 2.0, and 2.4 nm for the windows A, B, and C, respectively) for the particular wavelength window.
Line fluxes are derived from the areas under the fitted line curves. For the fit of single or unresolved lines (e.g. Ly-α, [OII]$\lambda\lambda 3726, 3729$, [SII]$\lambda\lambda 6716, 6731$) a modified Gaussian function is chosen of the form

$$f(\lambda) = f_0 \times \exp\{-1.96|(\lambda - \lambda_0)/\Delta\lambda|^{1.5}\} \tag{1.6}$$

where $\Delta\lambda$ is the instrumental resolution (FWHM). This function has a more pronounced peak and broader wings than a normal Gaussian profile, and provides a very good approximation of the core of the Airy function which describes the FP transmission. The area under this line profile is $A = 1.12 f_0 \times \Delta\lambda$. Accounting for the fact that the wings of the real FP profile are somewhat broader than in the above function, we use $A = 1.25 f_0 \times \Delta\lambda$. This factor was verified by two tests. First, a comparison of the fluxes of the [O III] lines from $z \sim 0.4$ galaxies as determined in the FP scans (window A) with those determined from the excess flux in the medium band filter located at $\lambda \approx 700$ nm above the continuum (Fig. 1.5, left panel) shows a good agreement. Second the fluxes derived by follow up spectroscopy agree quite well with the fluxes measured in the Fabry-Perot (Fig. 1.5, right panel), also if there are some exceptions. The higher flux measured by follow-up spectroscopy for two galaxies can be explained, since the line of these two galaxies was measured at the edge of the FP scan, resulting in a lower FP flux (see details in section 1.10.5). There are also some cases where the flux from spectroscopic follow up is lower

than the FP flux. In these cases the slit probably missed part of the line emitted region (see section 1.10.2 for details).

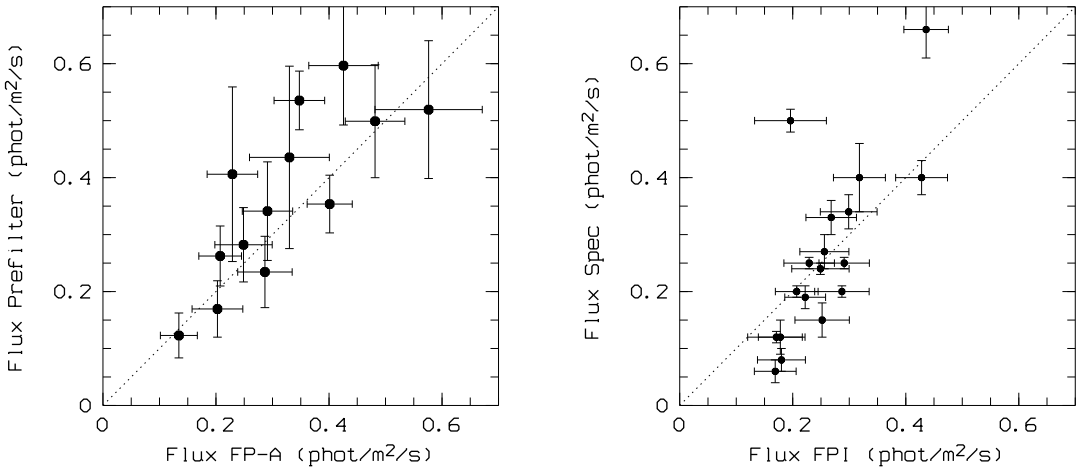

Figure 1.5 **Left panel:** Flux values derived from FP-A vs. line flux from the excess flux in prefilter for galaxies at $z \approx 0.4$ in 09h- and 23h-field. **Right panel:** Flux values from the spectroscopic follow-up vs. the flux derived from FP.

We also perform a double-line fit describing the [O III] doublet at $\lambda\lambda 4959, 5007$ and, in order to account for the (marginally resolved) [N II] $\lambda\lambda 6548, 6584$ doublet close to the Hα line, also a three-line fit.

(LF2) The line flux found in step (LF1) is subtracted from the pre-filter flux allowing for the filter transmission at the specific wavelength of the line (or lines, if it is a multiplet). Then, in an iterative way, the line corrected pre-filter flux - and its error - is introduced into the line fit as an additional data point outside of the scan interval. Examples for fits to different lines are depicted in the panels showing the FP-measurements in Fig. 1.2. Here the observed pre-filter fluxes are marked as solid bars with their errors, and the corrected pre-filter fluxes as dashed lines. Both values are also marked in the SED plots in the left panels.

(LF3) In the third step, for each of the eight redshifts determined above, template spectra published by Kinney et al. (1996) are fitted to the SED derived from the multi-filter photometry. This is done by means of colours, similar to the multi-color classification procedure described in Wolf et al. (2001), yielding a most probable template spectrum. An extra reddening correction of the template spectra up to $E(B-V) = 0.3$ is allowed.

Since we want to determine the fluxes in the emission lines from the signal excesses in the veto filters above the continuum (see section 1.8), line free template spectra are needed. Thus, the Kinney-Calzetti template spectra were altered by cutting out the prominent emission lines. As a consequence, those filter data where secondary emission lines are expected are not usable for the fit. Thus, the SED fit is purely based on the continuum part of the spectra. For the template spectrum which fits best to the observed SED, a reduced χ^2 is derived.

Since the detected line can be any emission line occurring in the observed wavelength window at the appropriate redshift (e.g., Hα at $z = 0.25$, [O III] at $z = 0.64$, etc., for the B window at 820 nm), the classification routine has to investigate the solutions for all bright emission lines. Thus, we consider a total of eight possible line identifications in our fitting procedure: Hα, [O III] λ 5007, [O III] λ 4959, Hβ, [O II] λ 3727, [S II] 6721, Hγ and Ly-α. Actually, a few galaxies were found to be seen by their [O I]λ6300 line, but their number is too insignificant to justify including this line to the list above.
For each of the eight possible line identifications the fit to the continuum spectrum also provides a new continuum level at the wavelength of the FP window, which is marked in either of the line plots in Fig. 1.2 as a dotted horizontal line. The error bar is estimated from the quality of the continuum fit, and is comparable to that of the pre-filter flux. Ideally, this continuum flux level should agree with the corrected prefilter flux (step (LF2)). A high discrepancy between the two values indicates that either the SED fit is bad (due to incorrect line classification), or the line feature seen in the FP scan is awkward. This information is used to produce another χ^2 contributor, calculated from the discrepancy and the intrinsic errors of the two flux levels.
Including the continuum level derived above, a new, better constrained, line fit is performed in the same way as in step (LF2). In this second iteration, however, bad line classifications become visible by large offsets between the continuum level given by the SED fit and the corrected pre-filter baseline, leading to a lower signal-to-noise ratio for the corresponding line fit. This also happens when the line feature in the FP data is in reality a false detection due to a statistical fluctuation of the FP signals.
The new signal-to-noise value is later used as critical indicator for the reality of the line feature seen in the FP scan, and whether the object will be accepted as an emission line galaxy.

1.8. Classification of Emission Line Galaxies

For the classification of emission line galaxies, three criteria are used:

(E1) the shape of the emission line observed with the FPI,

(E2) the emission line spectrum, derived from medium band veto filters placed at wavelengths where prominent secondary lines are expected, and

(E3) the continuum SED.

The continuum fit found in step (LF3) serves as a baseline to determine the fluxes of the other (secondary) emission lines. For each of the eight possible line identifications, the fluxes for the secondary lines were derived from the difference between the flux measured in the 'veto filters', the filters where other emission lines would be expected, and the continuum level predicted from the template fit. For the calculation of the line strength, the excess flux was normalized by the transmission of the filter at the wavelength given by the redshift derived from the FP observation. In cases where the veto filter included more than one emission line which generally happens for the [O III] $\lambda\lambda$ 4959, 5007 doublet, the line flux ratio was fixed to the canonical values. The left panel of Fig. 1.2 shows such fits for objects in whose spectra a number of 'secondary' lines can be seen.

Line identifications are made in the following manner. The measured line flux ratios are compared with a catalog of observed line ratios for (about) 500 nearby galaxies based on data from the literature, ranging from Seyfert galaxies to compact dwarfs, most notably from French (1980), McCall et al. (1985), Popescu & Hopp (2000), Veilleux & Osterbrock (1987), and Vogel et al. (1993).
A χ^2 is estimated in the following way: In the multidimensional space composed of all line ratio combinations possible for the respective classification of the line observed in the FPI window, the mean distance of the considered galaxy to the three closest tabulated ratios has been normalized by the error ellipse of the observed ratios. This method prevents a bias towards the most common line ratios, but also permits the identification of galaxies with extreme line ratios, as long as there are some objects with similar ratios tabulated. Again, a χ^2 for the line ratios is estimated for each of the eight line cases.
To decide between the possible line identifications an overall reduced $\bar{\chi}^2$ is derived which is the mean of the four χ^2 values: the SED fit, the line fit, the discrepancy of the baselines, and the line ratios. This mean reduced $\bar{\chi}^2$ is then converted into an overall probability, P, for the line classification, according to the formula $P = \exp(-\bar{\chi}^2/2)$. The case with highest probability is then selected as the most probable classification.

1.9. The Accuracy of z-Determination

1.9.1. z-Calibration Uncertainty

The wavelengths can be set with the FP etalon to within an accuracy of ± 0.2 nm. Wavelength calibration was checked several times each night using the calibration lamp lines Rb 794.5 nm and Ne 692.95 nm, and was stable to within 0.15 nm during the observations. This is roughly one order of magnitude less than the width of the instrumental profile of ~ 2.0 nm, which was adjusted by selecting the appropriate interference order of the FPI. Towards the edges of the fields, the transmitted wavelengths declined by 0.5 nm, due to the increasing angle of incidence in the FP etalon. In combination with the dithering used for the observations, this leads to an additional wavelength uncertainty of ± 0.1 nm at the edges of the frames. By fitting a line profile to the data obtained in the FP scan as shown in section 1.7, one gets a typical error of the line centre of $\sigma_\lambda \leq 0.3$ nm. Including this error of the line fit, the total uncertainty for a medium strong line thus rises to about ± 0.4 nm in λ, or about ± 0.0008 in redshift. In the following section we test if this is a realistic measure for the error in z or if the actual uncertainty in z is larger.

1.9.2. Comparison between z from FP scan and Spectroscopy

Spectroscopic follow-up of some galaxies at $z \approx 0.4$, where the [O III] $\lambda 5007$ line is detected in FP-A, was done at Telescopio Nazionale Galileo. For some galaxies at $z \approx 0.63$, where the [O III] $\lambda 5007$ line is detected in FP-B, spectroscopic follow-up with the VLT allowed us to measure redshifts. The comparison between spectroscopic and FP-redshifts shown in Fig. 1.6 indicates that the z-uncertainty for the value obtained from the FP can be larger than 0.0008, the value estimated in section 1.9.1. A value of 0.001 seems to describe the uncertainty in z more reliably.
In Fig. 1.7 we compare the z-values from line fits in FP-A with z-values from FP-C, where the Hα line of galaxies at $z \approx 0.4$ is detected. There is a small shift betwen measurements

of z from FP-A and FP-C, which comes partly from lines detected at the edge of the FP-A window (see section 1.10.5), and partly from the Hα line fit in window C, which includes the [N II] $\lambda\lambda 6548, 6584$ doublet; occasionally the fit for [N II] $\lambda\lambda 6548, 6584$ can be overestimated.

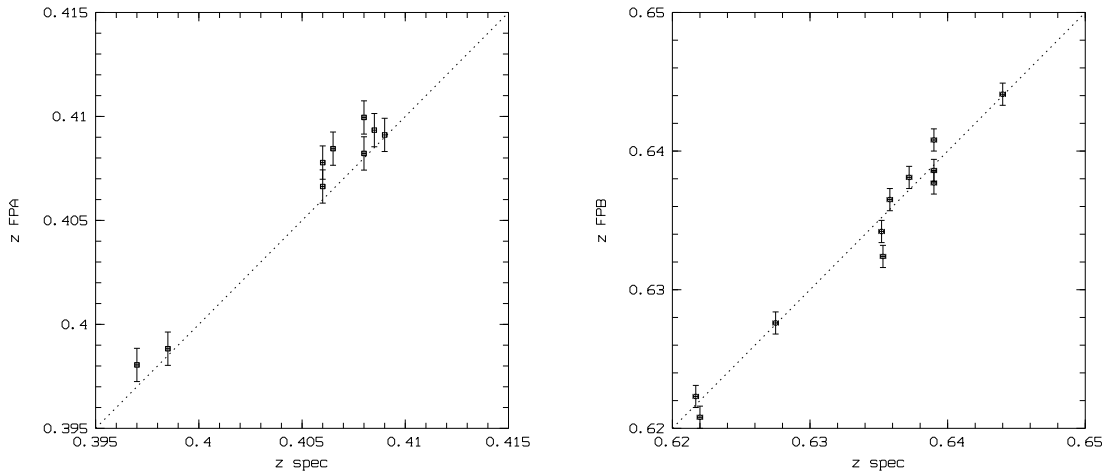

Figure 1.6 Left panel: z values from spectroscopic follow-up vs. z values from FP-A for galaxies at $z \approx 0.4$. **Right panel:** z values from spectroscopic follow-up vs. z values from FP-B for galaxies at $z \approx 0.63$.

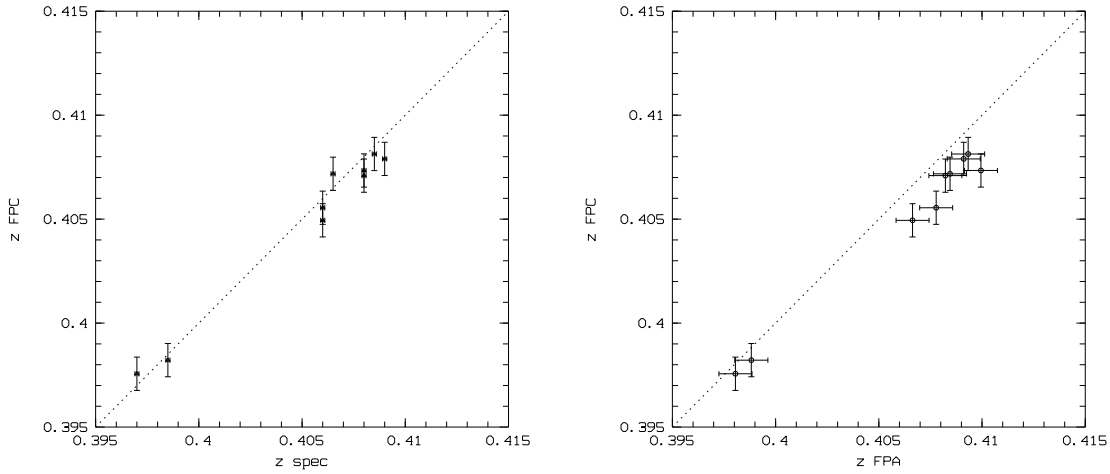

Figure 1.7 Comparison between z values from FP-C, spectroscopic follow-up and FP-A. **Left panel:** z values from spectroscopic follow-up vs. z values from FP-C for galaxies at $z \approx 0.4$. **Right panel:** z values from FP-A vs. z values from FP-C for galaxies at $z \approx 0.4$.

1.9.3. Comparison of z from MC-classification with z from FP scan

The multi-colour (MC) classification (see Wolf et al. 2001) provides a redshift determination, z_{MC}, for every object using the 17 filters of CADIS. Comparing z_{MC} with z_{FP}, the redshift derived from the line seen in FP, we can estimate the reliability of z_{MC}.

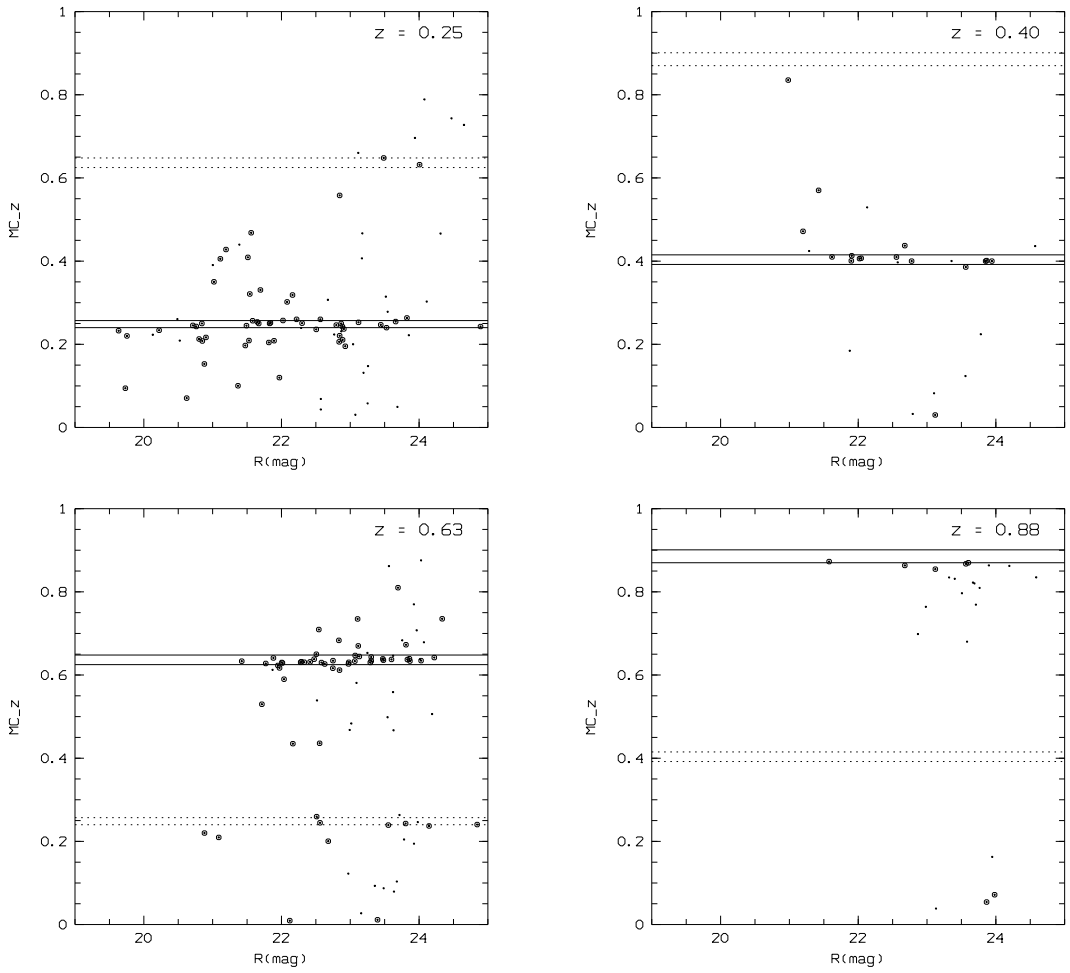

Figure 1.8 Comparison of z from MC-classification with z from FP scan, z_{FP}. z from the MC-classification is plotted vs. R magnitude for galaxies with $z_{FP} \approx 0.25$, 0.40, 0.63 and 0.88. Solid horizontal lines indicate the redshift range found for the most probable identification of the emission lines seen in the FP, dotted horizontal lines indicate the possible redshift range for another possible (but less probable) identification of the emission lines. Circles show galaxies with an uncertainty $\sigma_{MC} < 0.03$ for the redshift obtained from the MC-classification.

Fig. 1.8 shows z_{MC} vs. R magnitude for different z_{FP} bins, corresponding to different identifications of the emission lines seen in FP, Hα at $z \approx 0.25$, [O III] λ 5007 at $z \approx 0.4$, [O III] λ 5007 at $z \approx 0.63$, and [O II] λ 3727 at $z \approx 0.88$. Circles show galaxies with an uncertainty $\sigma_{MC} < 0.03$ for z_{MC}, i.e., galaxies with presumably reliable MC-classifications. One might expect that the MC-classification for these galaxies with $\sigma_{MC} < 0.03$ would deliver the correct interpretation of the emission line seen in the FP. But the diagrams in Fig. 1.8 show that even these galaxies (circles) do not always agree in the redshift interpretation with z_{FP}.

In the diagram for the FP redshift bin $z \approx 0.25$, z_{MC} suggests that another line identification for the line seen in FP, namely [O III] λ 5007 at $z \approx 0.63$, could apply to two galaxies with $\sigma_{MC} < 0.03$ (circles between the dotted lines). The emission line of one of these objects, 01h-3750, was indeed verified with the VLT to be [O III] λ 5007 at $z \approx 0.63$

(see chapter 2). Since the rotation seen in the appearance of the [O III] λ 5007 line (see Fig. 1.13) leads to a broadening of the integrated line, this line is, however, mistakenly classified as Hα/[N II] λ 6584 by the FP classiffication, step (E1). The emission line of the other galaxy, 23h-24538, has a probability for [O III] λ 5007 of 38.91%, and for Hα of 38.94%, derived from the FP classification. Therefore, a classification of the line as [O III] λ 5007, consistent with the MC classification, has the same probability as a classification as Hα. Thus, the two objects, 01h-3750 and 23h-24538, are two special cases, for which the MC classification is better than the FP classification.
In the diagram for the FP redshift bin $z \approx 0.63$, z_{MC} suggests that another line identification for the line seen in the FP, namely Hα at $z \approx 0.25$, could apply to six galaxies with $\sigma_{MC} < 0.03$ (circles between the dotted lines). Two of these galaxies lie near bright objects, so the FP line identification could have been affected by that. The CADIS measurements of the galaxy 23h-5709 suggest that the line seen in the FP scan is indeed [O III] λ 5007 at $z \approx 0.63$, as derived from the FP classification. The line of the remaining three galaxies, 23h-1937, 23h-5159, and 23h-6512, have been verified as [O III] λ 5007 at $z \approx 0.63$, in agreement with the z derived from the FP. This indicates that the redshift derived from FP scans is more reliable than z_{MC}.
Fig. 1.9 shows the histogram of the ratio $(z_{MC} - z_{FP})/\sigma_{MC}$ for objects with an R magnitude brighter than 23.5, which are expected to have a reliable MC-classification. Only objects with $(z_{MC} - z_{FP}) < 0.1$ have been taken into account for this diagram, in order to test the accuracy of z_{MC} for objects with similar z_{MC} and z_{FP}, i.e., galaxies lying between and near the solid lines in Fig. 1.8. The diagram shows that about 40% of these galaxies show a large discrepancy between z_{MC} and z_{FP}, which is not taken into account by σ_{MC}. Therefore, σ_{MC} seems to be underestimated for 40% of the galaxies. This also shows the advantage of the CADIS emission line survey CADIS, which can derive more precise redshifts (from the emission lines detected in the FP scans) than the MC classification.

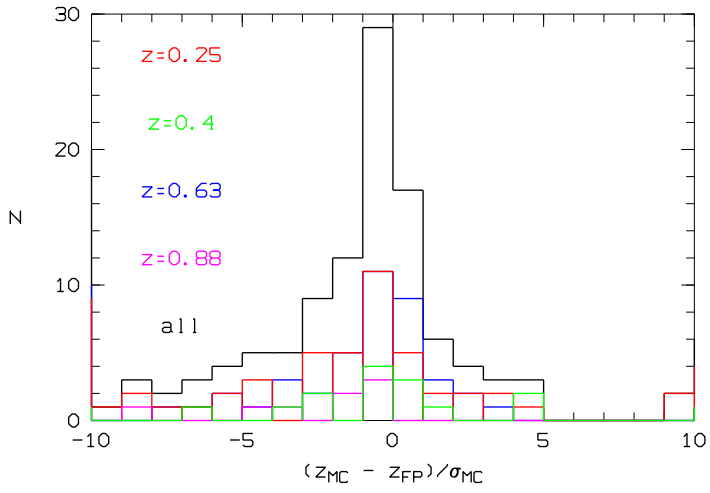

Figure 1.9 The histogram of the ratio $(z_{MC} - z_{FP})/\sigma_{MC}$ for objects with an R magnitude brighter than 23.5.

1.10. Difficulties Concerning the Verification of Lines by Follow-Up Spectroscopy

1.10.1. Comparison with Spectroscopic Observations

The decision on whether an emission line galaxy candidate is considered to be real is based on the signal-to-noise (S/N) ratio of its line fit. To avoid contamination of the galaxy samples by spurious objects and yet be complete as possible, an optimum signal-to-noise cutoff value K_{line} has to be determined (see requirement (S3), section 1.5).
Spectroscopic follow-up observations were carried out for a number of emission line galaxy candidates with the MOSCA instrument at the 3.5-m Calar Alto telescope, with LRIS at Keck, with FORS1 and FORS2 at the VLT, and with DOLORES at TNG. We compared the results of these observations with the predictions from our emission line classification in order to find the optimum S/N for reliable classification.
Fig. 1.10 shows that for a S/N= 3.8 cutoff, i.e. K_{line}=3.8, and for $R < 25$ (dotted lines), the probability for correct classification is of the order of 80%. For fainter galaxies the continuum is too weak and the signal too noisy to allow a reliable continuum fit. For galaxies with brighter R magnitudes, the S/N down to which we were able to verify the emission lines is even lower, e.g., down to $S/N = 3.4$ for $R < 23$. This indicates that we can reliably use a lower limit S/N for galaxies with brighter continua.
Nevertheless, the flux limit down to which we expect to be able to detect an emission line for galaxies with fainter continua in the FP-observations is lower than the result from the follow-up spectroscopy. Some possible explanations for this behaviour are discussed in the next sections.

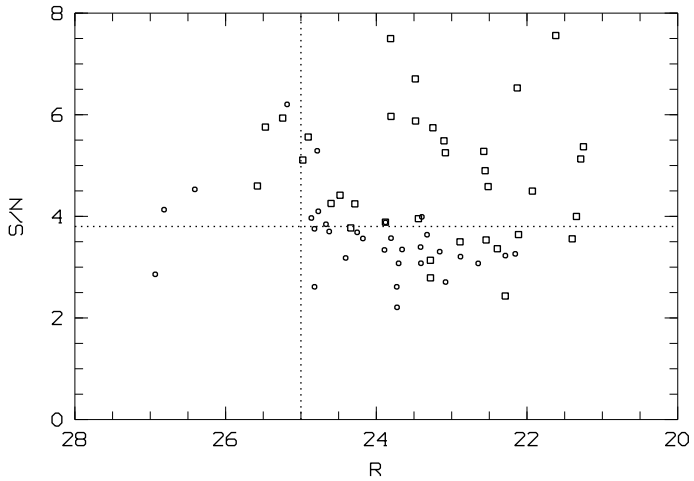

Figure 1.10 Correct and incorrect line identifications for spectroscopically observed galaxies in four CADIS fields, for varying R flux and S/N ratio. □ stands for correct identifications, ∘ indicates that no line could be verified at the predicted wavelength.

1.10.2. Offsets Between Position FP and Continuum

The coordinates of galaxies are used to prepare masks for follow-up spectroscopic observations. Therefore, astrometric accuracy is an important factor which can influence the verification of the emission lines of galaxies observed with the masks.

In order to obtain the absolute astrometry of any object detected in a CADIS field, a Digitized Sky Survey (DSS) red image measuring $15' \times 15'$ at the position of the CADIS field is used to select bright reference stars with known astrometry. These stars are then identified on a distortion-corrected CADIS R image, in order to calculate the coordinate transformation between the DSS and the CADIS images. With this coordinate transformation, a set of faint secondary reference stars in the CADIS field which can be identified on the DSS image is used to obtain coordinates for the other objects in the field. In this manner, we achieve an absolute astrometric accuracy of $0''.5$, and a relative accuracy of $0''.1$ for continuum objects, i.e., objects seen in the R images. However, the astrometric precision could be worse for objects that are only detected in the FP scan, such as faint emission line galaxies (e.g., Ly-α galaxy candidates).

A way to analyse this precision is to check the positions found by SExtractor on FP- and CADIS filter images for a set of test objects, with FP-fluxes typical for the emission lines being searched, i.e., ~ 0.1 phot m^{-2} s^{-1} nm. To this end, I selected galaxies with a continuum flux in the B815 pre-filter of 0.1 phot m^{-2} s^{-1} nm $^{-1}$ which show no emission lines in FP-B, in order to analyse how their detected positions on the FP images scatter around the astrometry-relevant positions found on medium band filters. Fig 1.11 shows the positions found by SExtractor for these galaxies in the summed images for medium-band filters (dots), for FP wavelengths settings (circles), and the averaged position as given in the "masterlist" (cross). The distances between the averaged position from the masterlist and each detected position in different FP wavelength settings are plotted as an histogram in Fig 1.12; the mean value is approximately 0.4. This indicates that a spatial offset of about $0''.4$ is possible between the position of the line emission on the FP images, and the continuum of the object observed in the CADIS filters. Since the offset scales with $1/\sqrt{N}$, where N is the FP flux, we expect a larger offset for a lower FP flux, e.g., an offset of $0''.6$ for a FP flux of ~ 0.05 phot m^{-2} s^{-1} nm.

The fact that the astrometry is used to prepare the masks for follow-up spectroscopic observations could explain why we did not detect some emission line objects seen in the FP; the astrometry delivers more accurate coordinates for objects with multiple detections (FP and continuum) and can be off $0''.4$ (or even up to $1''$) for objects detected only in the FP (faint emission line galaxies). This can play a role in the spectroscopic (non-) verification of Lyman-α candidates, where only the line is detected: if the slit width is too small, the galaxy can be missed. It could also explain the non-verification of emission lines for galaxies with faint continuum in Fig. 1.10.

1.10.3. Extranuclear HII Regions and Object Blending

In a number of cases, the spectra showed a spatial offset between line emission and continuum object of up to $1''$. Fig. 1.13 shows an emission line galaxy spectrum in which we observed two extranuclear HII regions of the galaxy 01h-3750. As another example, galaxy 01h-2057 shows two blended objects, with the brighter object (continuum visible) being a galaxy at $z = 1.2$, and the fainter object a galaxy with detected [O III] $\lambda 5007$ and

[O III] λ 4959 lines with redshift $z = 0.616$ (Fig 1.14). Considering that the slit, generally centered on the continuum source, is only $1''.0$ wide, it is possible that in some cases where an emission line detected in the FP scan could not be verified in the slit spectra, the slit actually missed the line emitting region. In those cases the photometric data derived from the imaging survey would tend to yield more reliable results than slit spectroscopy.

1.10.4. Variability

Variable objects can contaminate our sample of faint emission line galaxies, if the object was bright during the observations in one FP wavelength. In the case of short time variability, the prefilter image can determine if the emission line is real or not, e.g., when the flux in the prefilter is too low to be consistent with an observed emission line. With variability on longer timescales, both the FP image and the prefilter could show a higher flux, and additional observations of the prefilter at another epoch are necessary, in order to check the reliability of the emission line.
In order to check if we can find variable objects by repeated filter observations, broad R-band images in the 09h field were taken several times, at different epochs. To detect variable objects, I used observations from four different epochs of the 09h-field, and measured the fluxes of galaxies in the R filter independently for each epoch. Diagrams in which the flux difference between two epochs is plotted vs. the R-flux in one epoch can be used in order to identify variable objects. The trumpet-shape distribution (similar to that shown in Fig. 1.3) becomes wider for fainter objects, such that one can easily identify brighter outliers as variable objects candidates. After checking these outliers for contamination through bright stars near the object position, I found variability for some objects classified as quasars, but also for some other objects (possibly variable stars), and even a high-redshift supernova candidate with no detectable host galaxy.
Thus, variable objects exist and can be found in the CADIS sample. They can contaminate our sample of faint emission line galaxies, if the object was only bright during the epoch of observations in one FP wavelength. Nevertheless, repeated observations at different epochs, e.g., of the prefilter images, are useful for rejecting such variable objects.

1.10.5. Lines Detected at the FP Scan Edge

Spectroscopic follow-up measurements of galaxies with a line detected at the FP scan edge, e.g., for the line [O III] λ 5007 of the galaxy 09h-8327 (Fig. A.13), yield a higher flux for the line than what is measured in the FP window edge. This behaviour is shown also by some other galaxies with lines detected at the FP scan edge (Fig. 1.5), for which the flux from the FP scan is lower than the flux obtained from spectroscopy or from the prefilter. A small redshift offset between the z derived from spectroscopy and the z from FP scans is also observed for such objects (see Fig. 1.6 and 1.7). These differences in flux and redshift between FP scans and other measurements (prefilter or spectroscopy) can be explained by the fact that the center of the modified Gaussian (equation 1.6) is forced to be inside the FP scan; see, e.g., the [O III] λ 5007 line of the galaxy 09h-8327 in Fig. A.13. Thus, the redshift of the line is shifted to a slightly lower value, and the measured flux decreases, because the part of the line lying outside the FP scan is underestimated.

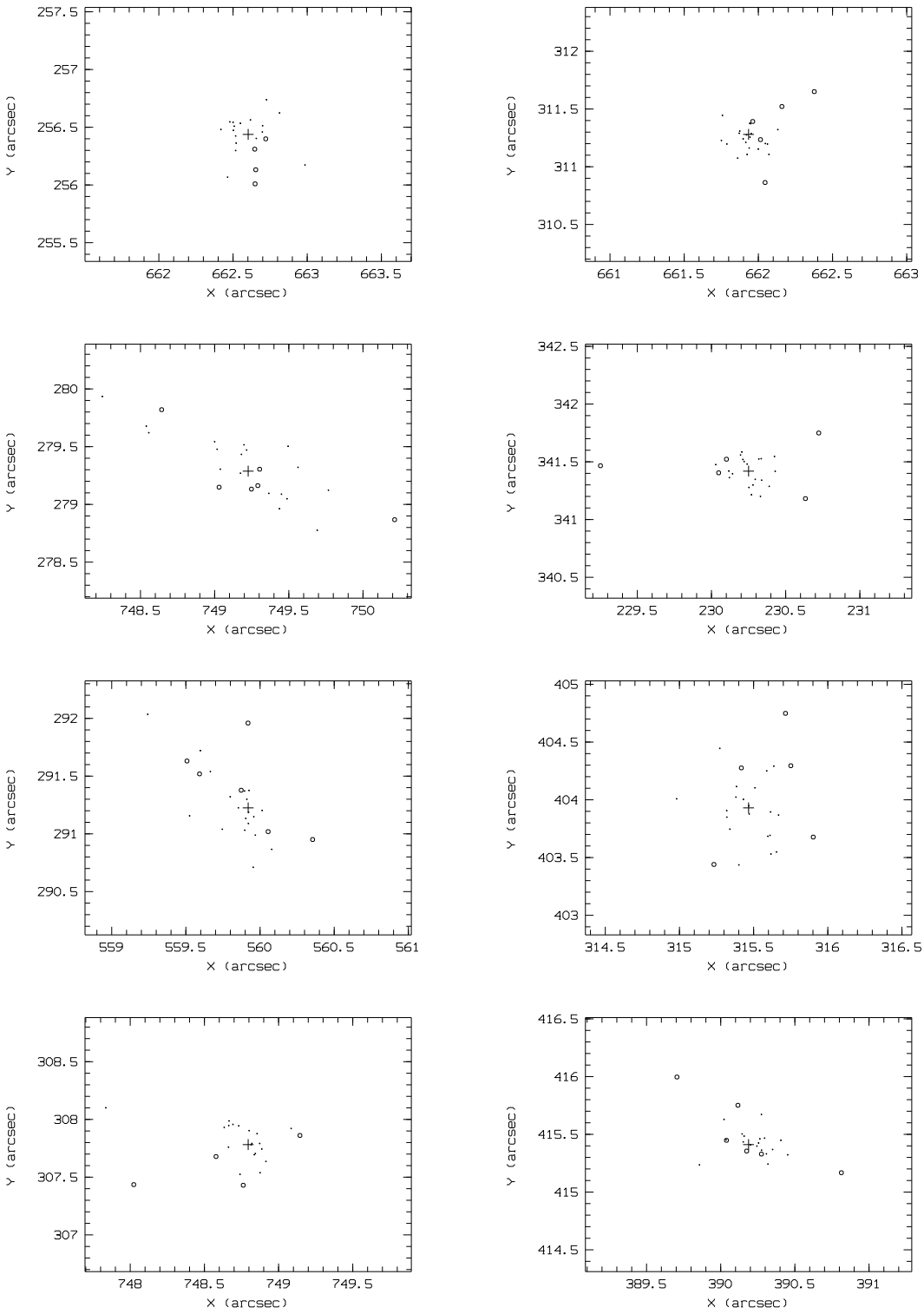

Figure 1.11 X−Y positions of galaxies found by SExtractor in the summed images for medium-band filters (dots), for FP wavelength settings (circles), and the averaged position as given in the masterlist (cross).

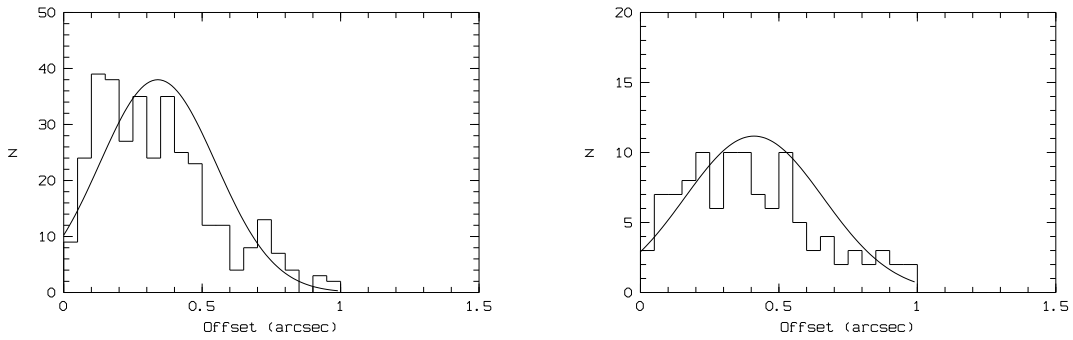

Figure 1.12 Histogram of offsets between the position of the line emission and continuum for objects in 01h-field (left), and 23h-field (right). Details are given in the text.

Figure 1.13 Two extranuclear HII regions in the galaxy 01h-3750, at $z = 0.634$. The spectrum was taken with FORS 2 at the VLT. Wavelength increases to the right.

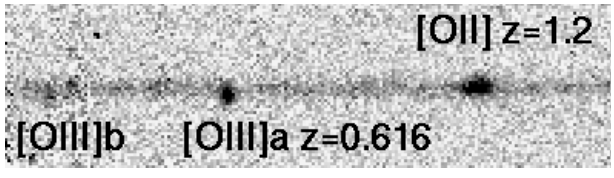

Figure 1.14 Object blending, in the case of galaxy 01h-2057. The spectrum was taken with FORS 2 at the VLT.

1.11. Sample Statistics

1.11.1. Emission Line Galaxies with a line detected in FP-A or FP-B

The emission line galaxy candidate samples, selected according to criteria described in sections 1.5, 1.7, and 1.8, are separated into specific redshift ranges. Objects identified as quasars in the multi-color classification scheme are rejected in order to provide a sample of non-active emission line galaxies. The numbers of objects in the four CADIS fields, classified as Hα galaxies, [O III] λ5007 galaxies, [O II] λ3727 galaxies, and Hβ galaxies (at the appropriate redshifts) are listed in Table 1.4. The number of galaxies detected by emission lines other than [O III] λ5007, [O II] λ3727, or Hα is too small for a useful statistical study. The expected number of galaxies detected by their [O III] λ4959 line in the B window, for example, can be readily estimated from the statistics of the brighter [O III] λ5007 line. Since the line intensity ratio of these lines is 3:1, the expected number is about that of the number of [O III] λ5007 with a S/N greater than $3 \times (S/N)_{lim} = 11.4$, which is only 7 galaxies. Therefore, in the following, [O III] always stands for the brighter [O III] λ5007 line.

Table 1.4 Statistics for the emission line galaxies observed in several redshift intervals.

Line	Window	Total area ($\Box'$)	z range	Δ z	S/N limit	N_{gal}
Hα	A	201	0.062-0.080	0.018	3.8	27
Hα	B	413	0.240-0.257	0.017	3.8	109
[O III]	A	201	0.392-0.415	0.023	3.8	36
Hβ	A	201	0.434-0.458	0.022	3.8	9
[O III]	B	413	0.625-0.648	0.023	3.8	93
Hβ	B	413	0.674-0.697	0.023	3.8	21
[O II]	A	201	0.870-0.901	0.031	3.8	63
[O II]	B	413	1.183-1.214	0.031	3.8	168

1.11.2. Comparison between Line Ratios from CADIS and Local Galaxies

For galaxies in the 09h- and 23h-fields, where FP-A, FP-B, and FP-C data have been reduced and analysed, the [O III] λ5007, Hα, and [O II] λ3727 lines at $z \approx 0.4$ are detected in FP-A, in FP-C, and in the veto filter V522. Thus, we can calculate the line ratios F([O III] λ5007)/F(Hα) vs. F([O II] λ3727)/F([O III] λ5007) for these galaxies at $z \approx 0.4$, and compare them with line ratios for nearby galaxies from the literature (the above mentioned sample in section 1.8). Three objects at $z \approx 0.4$, for which systematic errors in the flux calculation were detected, have been excluded from the comparison: The object 09h-25275 lies very close to another galaxy (09h-4319) at $z \approx 0.4$, so that the measurement of line fluxes was affected by the nearby object. In another case (galaxy 09h-6525) the line flux in FP-C for Hα was underestimated because of an inaccurate measurement at one FP-setting. In the third case the line flux measured in the veto filter V522 for the

[O II] λ3727 line of the galaxy 23h-10445 was too low, because of the strong 400 nm break of this galaxy.

For emission line galaxies at $z \approx 0.25$ with the Hα line detected in FP-B we detect [O III] λ5007, and [O II] λ3727 in the veto filters V628, and V465, respectively. Since line fluxes derived from veto filters have larger error bars than those detected by the Fabry-Perot, we did not include in our analysis galaxies at $z \approx 0.25$ with large error bars in the [O III] λ5007 flux.

Fig. 1.15 shows the comparison between line ratios of local galaxies with line ratios of CADIS galaxies at $z \approx 0.25$ and $z \approx 0.4$. The galaxies at $z \approx 0.4$ in the left panel are selected by their [O III] λ5007 line seen in the FP window A; galaxies at $z \approx 0.4$ in the right panel are selected by their Hα line detected in the FP window C. The plots show that CADIS galaxies occupy a region in the diagnostic diagrams similar to that of local galaxies from the literature sample.

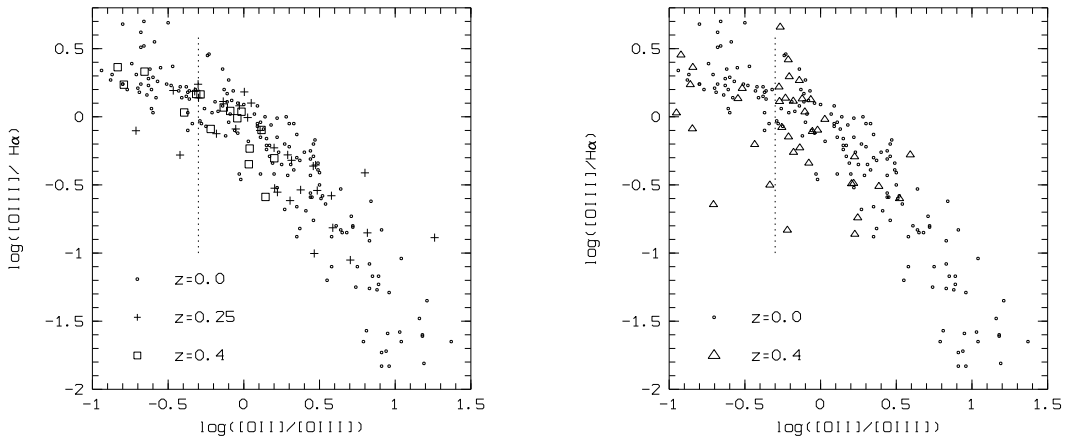

Figure 1.15 Diagnostic diagram F([O III] λ5007)/F(Hα) vs. F([O II] λ3727)/F([O III] λ5007). Small circles denote line ratios from the literature, ranging from Seyfert galaxies to compact dwarfs, most notably from French (1980), McCall et al. (1985), Popescu & Hopp (2000), Veilleux & Osterbrock (1987), and Vogel et al. (1993). The dotted line shows the selection limit of candidate metal poor galaxies with high [O III] λ5007/[O II] λ3727 (section 2.2). **Left panel:** Crosses are CADIS line ratios for galaxies at $z \approx 0.25$. Squares are CADIS line ratios for galaxies at $z \approx 0.4$ selected by their [O III] λ5007 line detected in FP-A. **Right panel:** Triangles are CADIS line ratios for galaxies at $z \approx 0.4$ selected by their Hα line detected in FP-C.

1.12. Luminosity Functions for the Emission Line Galaxies

1.12.1. The Luminosity Function

The luminosity function (LF), i.e., the number of galaxies per unit comoving volume in the luminosity interval from L to $L + dL$, can usually be described by the Schechter function (Schechter 1976):

$$\Phi(L)dL = \phi^* \cdot \left(\frac{L}{L^*}\right)^{\alpha} e^{-L/L^*} d\left(\frac{L}{L^*}\right). \tag{1.7}$$

The parameter ϕ^* is a number per unit volume, and L^* is a "characteristic luminosity" (with an equivalent characteristic magnitude, M^*) at which the luminosity function exhibits a rapid change in the slope in the ($\log\phi$, $\log L$)-plane. The dimensionless parameter α gives the slope of the luminosity function in the ($\log\phi$, $\log L$)-plane when $L << L^*$.
When the luminosity L is transformed into a logarithmic magnitude scale using $\Phi(L)dL = \Phi(M)dM$ and $dM = -2.5\log(\mathrm{e})\,\mathrm{dL/L}$, then the number of galaxies per unit volume in the luminosity interval from M to $M + dM$ is:

$$\Phi(M)dM = 0.4\,\phi^* \cdot \Xi^{\alpha+1} e^{-\Xi} dM \tag{1.8}$$

with $\Xi = 10^{-0.4(M-M^*)}$.

1.12.2. Absolute B-Magnitude

The large wavelength coverage of the CADIS filters allows us to derive precise absolute fluxes without using any K-correction factor. The slope of the spectrum between two measured data points can be considered as linear and the flux value at the restframe wavelength is calculated by linear interpolation between the measurements of two adjacent filters. The B-magnitude is given by

$$M_B = -2.5 \cdot \log\frac{\mathrm{F}(\lambda_{\mathrm{shift}})}{\mathrm{F(Vega)}} - 5 \cdot \log(\mathrm{D_L[pc]}) + 5. \tag{1.9}$$

The Vega flux, F(Vega), of the rest frame filter Johnson B ($\lambda_{\mathrm{B}} = 447.89\,\mathrm{nm}$) is $1.3775 \cdot 10^8$ photons $\mathrm{m^{-2}\,sec^{-1}\,nm^{-1}}$. $\lambda_{\mathrm{shift}} = (1+z) \cdot \lambda_{\mathrm{B}}$ is about 627 nm for galaxies at $z \approx 0.4$ (CADIS Filter V628), and about 730 nm for galaxies at $z \approx 0.63$ (CADIS Filter R and B752). The luminosity distance, $\mathrm{D_L}$, is given by equation B.10.

1.12.3. M_B Luminosity Functions for the CADIS Emission Line Galaxies

The M_B luminosity functions (for the cosmology $\Omega_M = 0.3$, $\Omega_\Lambda = 0.7$) are shown in Fig. 1.16 for galaxies with [O III] λ 5007 and [O II] λ 3727 emission lines detected in FP-A (averaged over the 09h- and 23h-fields), and in Fig. 1.17 for galaxies with the Hα, [O III] λ 5007, and [O II] λ 3727 emission lines detected in FP-B (averaged over four CADIS fields). The data points for the mean density are in agreement with the luminosity function obtained for late-type galaxies (later than Sa) in the respective redshift ranges, derived from the multicolor survey of CADIS (Fried et al. 2001). The Schechter function overlaid in the figures is also adopted from Fried et al., and represents the sum of the two LFs for starburst galaxies and spirals in their paper.

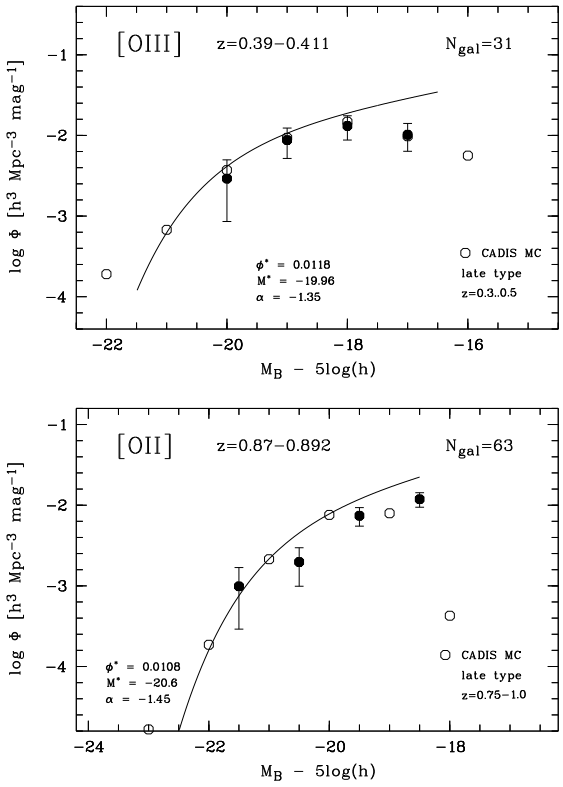

Figure 1.16 M_B luminosity functions for the emission line galaxies at $z \approx 0.4$, and $z \approx 0.88$, with a line detected in FP-A (filled circles). For comparison open circles trace the luminosity functions for late-type galaxies according to the CADIS multicolor survey (Fried et al. 2001), together with the corresponding Schechter functions. Schechter parameters are given near the high luminosity ends of the curves.

This agreement suggests that in principle all late type galaxies at these redshifts are emission line galaxies with lines bright enough to be detected in the CADIS Fabry-Perot observations. Moreover, one can see that CADIS can find galaxies fainter than $M_B - 5\log \mathrm{h} = -19$ at medium redshift by their emission lines. Such faint galaxies might be overlooked in continuum selected samples from other surveys.

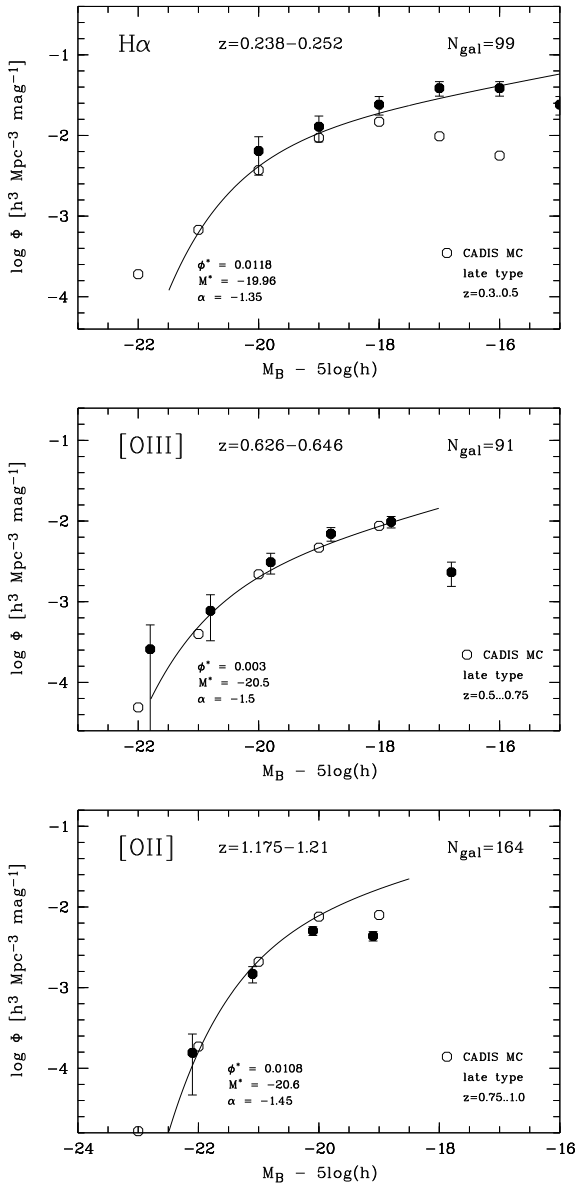

Figure 1.17 M_B luminosity functions for the emission line galaxies at $z \approx 0.25$, $z \approx 0.64$, and $z \approx 1.2$ with a line detected in FP-B (filled circles). For comparison, open circles trace the luminosity functions for late-type galaxies according to the CADIS multicolor survey (Fried et al. 2001), together with the corresponding Schechter functions. Schechter parameters are given near the high luminosity ends of the curves.

1.12.4. Luminosity Functions for the Emission Line Fluxes

The determination of luminosity functions for emission line fluxes is important in order to calculate global star formation rates, since, as shown by Kennicutt (1983), the total number of ionizing photons from newly produced stars is a good measure of the current star formation in a galaxy (see equation B.2). Fig. 1.18 shows luminosity functions for the emission line fluxes of galaxies at $z \approx 0.4$ and 0.88, and Fig. 1.19 shows the same for galaxies at $z \approx 0.25$, 0.63 and 1.2. The sampling interval for the line luminosity was chosen as 0.4 dex in these diagrams, equivalent to a stepsize of one magnitude, in order to allow an easy comparison with the M_B luminosity functions. Open circles are uncorrected, filled circles are extinction corrected values. The extinction has been calculated according to the relation found by Jansen et al. (2001, figure 1d): $E_{B-V} = 0.064\,(M_B + 14.8) \pm 0.10$, although we adopted a minimum reddening correction of $E_{B-V} = 0.05$ mag. The $L_{[O\,II]}$ plot of Fig. 1.19 shows that the extinction correction amounts to a factor of about 4 in the total [O II] $\lambda 3727$ line luminosity. In the case of the Hα luminosity at $z = 0.25$ (Fig. 1.19), the correction yields an increase of the total line luminosity by a factor of 1.5.

In several studies (Gallego et al. 1995, Tresse & Maddox 1998, and Yan et al. 1999) line luminosity functions were successfully described by Schechter functions, the parameters of which were derived by the V_{max} method. For small data samples, however, this procedure leads to somewhat arbitrary results.

As can be seen in the plots, the Hα luminosity function ($z \approx 0.25$) can, nevertheless, be described with a Schechter function of the same shape as the respective blue magnitude function. The overplotted curves are actually fits to the observed distribution using the same fixed Φ^* and α parameters as in the corresponding M_B luminosity functions. The reason for this agreement seems to be twofold: on one hand the fainter galaxies are preferentially of type BCD or Irr, leading to a steepening of the line luminosity function relative to the blue magnitude function. On the other hand, the internal extinction acts preferentially on massive galaxies, and thus its correction yields a stretching of the luminosity function at its bright end, partly cancelling the other effect. Consequently, we use the same shape parameters for the line luminosity Schechter functions as those describing the blue magnitude luminosity functions (Fig. 1.16 and 1.17).

In the $L_{H\alpha}$ plot of Fig. 1.19, the extinction-uncorrected line luminosity data of Tresse & Maddox (1998) for $z < 0.3$, and of Cowie et al. (1997), converted to the cosmological parameters used for CADIS data ($\Omega_M = 0.3$, $\Omega_\Lambda = 0.7$), are also plotted. The Tresse & Maddox and the Cowie data agree reasonably well with our data.

The M^* values from Fig. 1.16 and Fig. 1.17 can be compared with the corresponding L^* values from Fig. 1.18 and 1.19, since the Schechter functions for the respective redshift intervals have identical ϕ^* and α parameters. The comparison shows that the ratio between blue flux density and emission line flux density (which is a measure of the star formation rate) increases by a factor of ~ 5 between $z = 0.25$ and 1.2. Thus, the star formation rate per blue luminosity unit increases drastically when we look back in time. The slower evolution of the blue luminosity density indicates that the ratio of moderately young stars (age $\simeq 2$ Gyr) to very young stars (age < 100 Myr) evolves with time: at higher redshift starbursts were more frequent than today.

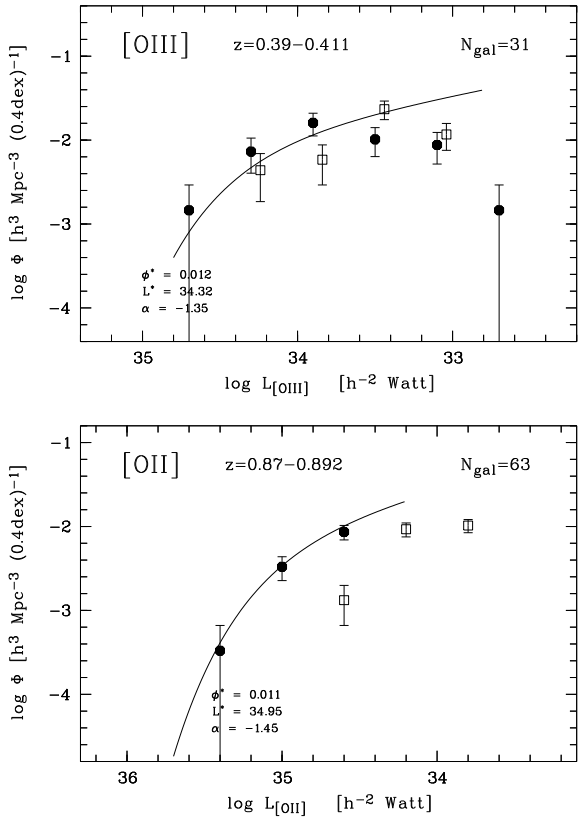

Figure 1.18 Luminosity functions for [O III] λ 5007 line emission at redshift ≈ 0.4 (upper panel), and for the [O II] λ 3727 line at redshift $z \approx 0.88$ (lower panel). Open circles are uncorrected, filled circles are extinction corrected values. The parameters for the overplotted Schechter functions have the same Φ^* and α as the M_B luminosity functions.

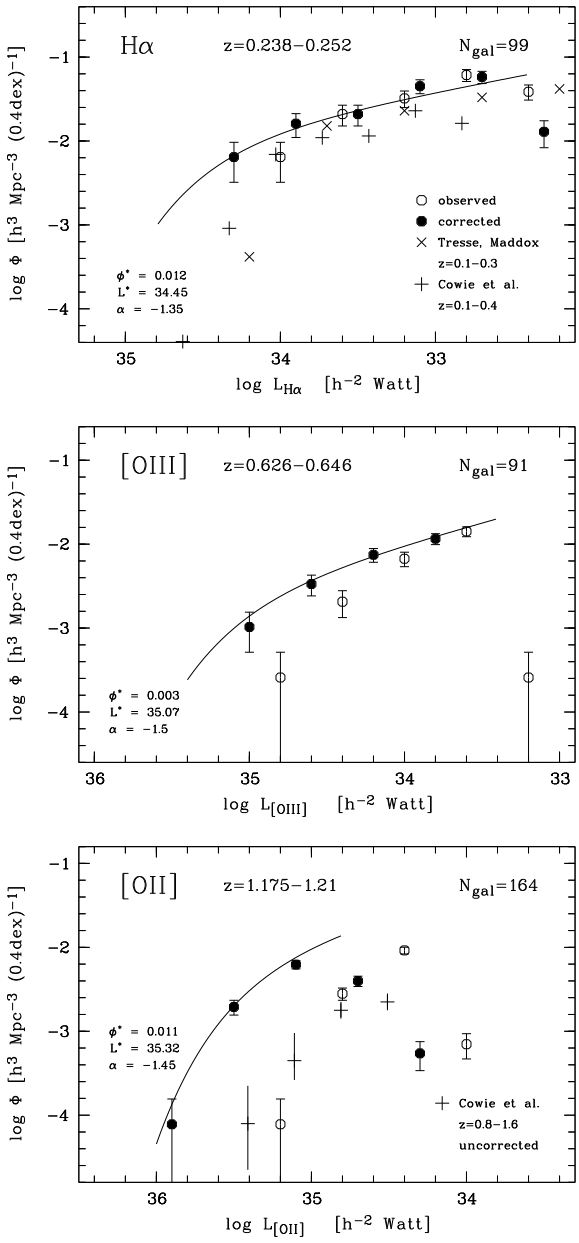

Figure 1.19 Luminosity functions for the Hα line emission at redshift ≈ 0.25 (top), for the [O III] λ5007 line at redshift $z \approx 0.63$ (middle panel), and for the [O II] λ3727 line at redshift $z \approx 1.2$ (bottom). Open circles are uncorrected, filled circles are extinction-corrected values. For comparison, the observed (uncorrected) line luminosity functions from Cowie et al. (1997) and Tresse & Maddox (1998) are shown. The parameters for the Schechter functions plotted over the data have the same Φ^* and α as the M_B luminosity functions.

Metal Abundances of Faint Emission Line Galaxies at Medium Redshift

2.1. Measuring Metallicities of Galaxies at $z > 0$

Optical emission lines from HII regions have long been the primary means of gas-phase chemical diagnosis in galaxies; see, for example, the review by Shields (1990). The advent of large telescopes and sensitive spectrographs enables direct measurement of the chemical properties in the ionized gas of cosmologically–distant galaxies with the same nebular analysis techniques used in local HII regions.

Distant galaxies subtend small angles on the sky, comparable to typical slit widths in a spectrograph; so galaxy spectra tend to be integrated spectra. For example, a typical ground-based resolution element of $1''.0$ corresponding to a linear size of about 7 kpc[1] at $z = 0.5$ (see equation B.12) encompasses entire galaxies. The legitimate question about the utility of *spatially-integrated* emission line spectroscopy for studying the chemical properties of star-forming galaxies at earlier epochs has been investigated by Kobulnicky et al. (1999). They compared physical conditions derived from spectroscopy of individual HII regions with results from global galaxy spectroscopy, and showed that spatially unresolved (i.e., global) emission-line spectra can reliably indicate the chemical properties of distant star-forming galaxies. Fig. 2.1 illustrates the comparison between the empirical abundances derived from integrated spectra with the actual disk abundances from Zaritsky et al. (1994), measured at 0.4 times the corrected isophotal radius. The diagram shows how well the weighted-average mean nebular spectrum characterizes the overall galaxy abundance.

In the local universe, metallicity is well correlated with the absolute luminosity (stellar mass) of galaxies (Skillman et al. 1989, Zaritsky et al. 1994, Richer & McCall 1995, Garnett et al. 1997, Hunter & Hoffman 1999, Melbourne & Salzer 2002, among others) in that more luminous galaxies tend to be more metal rich than less luminous galaxies. The metallicity-luminosity relationship is usually attributed to the action of galactic superwinds. Massive galaxies reach higher metallicities because they have deeper gravitational potentials which are better able to retain their gas against the building thermal pressures from supernovae, whereas low-mass systems eject their gas before high metallicities are attained, because supernovae-driven winds remove large amounts of metal-enriched gas from these low-mass systems (e.g., MacLow & Ferrara 1999).

[1]Note that $H_0 = 62$ km s^{-1} Mpc^{-1}, $\Omega_0 = 0.3$, $\Omega_\Lambda = 0.7$ is used in this chapter

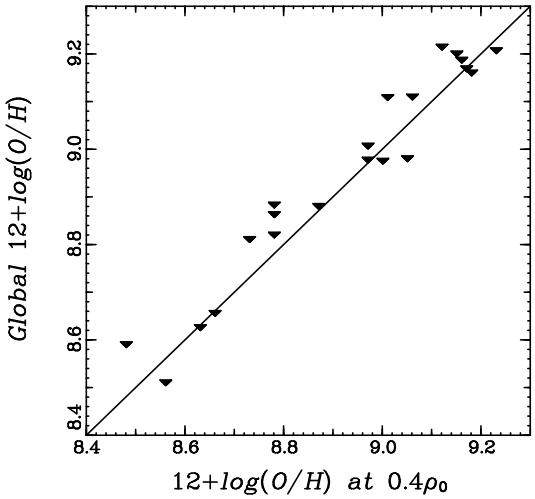

Figure 2.1 Comparison between spectroscopy of individual HII regions with results from global galaxy spectroscopy. The characteristic O/H ratio at a radius of 0.4 isophotal radii as tabulated by Zaritsky et al. (1994) is plotted versus the O/H ratio derived from the global nebular spectrum for each galaxy (from Kobulnicky et al. 1999). The global spectra produce oxygen abundances which are in excellent agreement (0.1 dex) with the value at 0.4 isophotal radii.

At medium redshift, all previous attempts to study the evolution of metallicity with cosmic time (Kobulnicky & Zaritzky 1999, Hammer et al. 2001, Carollo & Lilly 2001, Contini et al. 2002) were based on continuum selected samples, the emission lines of which were identified by spectroscopy. Thus, for instance, the CFRS sample used by Carollo & Lilly (2001), selected using $I < 22.2$, contains only bright galaxies ($M_B < -20$) at redshift $z > 0.6$, the continuum of which is dominated by an evolved stellar population. Kobulnicky & Zaritzky (1999) measured oxygen abundances for galaxies with $M_B < -20$ at $0.1 < z < 0.5$, and only one galaxy with $M_B = -18.5$ at $z = 0.4$; Hammer et al. (2001) measured abundances of galaxies with $M_B < -20$ at $0.4 < z < 0.8$; and Contini et al. 2002 measured abundances of galaxies with $M_B < -19.5$ at $0.2 < z < 0.4$. Altogether, at $0.2 < z < 1$, an oxygen abundance for only one galaxy fainter than $M_B = -19.5$ has been measured so far. All the other galaxies at $0.2 < z < 1$, with measured abundances, are more luminous ($M_B < -20$). At $z \approx 3$, however, oxygen abundances have been measured for some luminous galaxies ($M_B < -22$). Fig. 2.2 shows, for local, intermediate, and high-redshift galaxies, the oxygen abundance vs. absolute restframe B magnitude diagram, from Contini et al. 2002 (left panel), and from Kobulnicky et al. 2000 (right panel).
The mean least-squares fit to the UV-selected and HII galaxies (dashed line in the left panel) shows a slope very close to the one derived for local irregular and spirals galaxies (solid line). UV-selected and HII galaxies appear 2–3 mag brighter than local "normal" galaxies of similar metallicity as might be expected if a strong starburst has temporarily lowered their mass-to-light ratios. High redshift objects ($z \approx 3$) from Kobulnicky et al. 2000 (right panel), and from Pettini et al. 2001 (left panel), are significantly more luminous for their metallicity than local objects. Under the assumption that Lyman-break galaxies evolve into modern day ellipticals and galactic spheroids, arrows in the right panel indicate the tracks of high-redshift galaxies as they fade and become more chemically enriched. The solid arrow shows qualitatively the path of a galaxy which fades

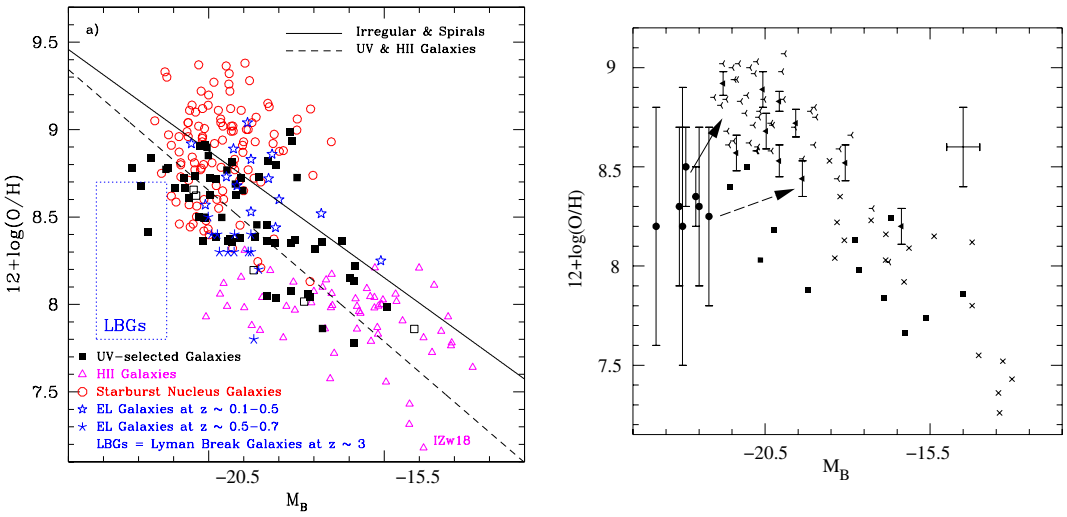

Figure 2.2 Oxygen abundance, 12+log(O/H), vs. the absolute restframe B magnitude M_B.
Left panel Metallicity–luminosity relation for UV-selected galaxies from Contini et al. 2002 (squares), and for comparison samples of local, intermediate, and high redshift galaxies. The local star-forming galaxy samples are HII galaxies (triangles), and starburst nucleus galaxies (circles). The solid line is a linear least-squares fit to local irregular and spiral galaxies (see Kobulnicky & Zaritsky 1999). The dashed line is a mean least-squares fit to the UV-selected and HII galaxies. Two samples of intermediate-redshift galaxies (stars) are also shown for comparison: emission-line (EL) galaxies at $z \sim 0.1 - 0.5$ (Kobulnicky & Zaritsky 1999), and luminous compact EL galaxies at $z \sim 0.5 - 0.7$ (Hammer et al. 2001). The location of high-redshift ($z \sim 3$) Lyman break galaxies (LBGs) is shown as a box encompassing the range of O/H and M_B derived for these objects (Pettini et al. 2001).
Right panel Local irregular and spiral galaxies collected from the literature and Kobulnicky et al. (1999) appear as crosses and inverted Y's, respectively. A representative error bar appears in the upper right. The sample of intermediate-redshift $z \sim 0.4$ emission line galaxies from Kobulnicky & Zaritsky (1999) appears as filled triangles. Filled squares denote local HII galaxies from the sample of Telles & Terlevich (1997). High-redshift objects from Kobulnicky & Koo (2000) appear as filled circles with error bars. For futher explanations see text.

as its interstellar medium becomes more chemically rich by the continued cycles of star formation and metal production. The dashed arrow shows qualitatively the evolution if metal enrichment is surpressed by continued inflow of metal-poor gas as fading processes.

One interpretation of this result could be that Lyman-break galaxies have mass-to-light ratios which are significantly lower than those which apply to the normal galaxy population at the present epoch. Another possibility is that the whole metallicity-luminosity relation is displaced to lower abundances at high redshifts, when the universe was younger, and the total interval of time available for the accumulation of the products of stellar nucleosynthesis was shorter. It should be possible to determine the magnitude of this second effect by measuring the oxygen abundance in known samples of galaxies at medium redshift. This is also a motivation for the study of metal abundances at medium redshift of emission line galaxies of CADIS with *faint* absolute luminosities. Oxygen abundances of *faint* galaxies together with the published abundances of luminous galaxies at medium z should establish the metallicity-luminosity relation at $0.2 < z < 1$.

2.2. CADIS Advantages for Searching Metal Poor Galaxies

The CADIS deep emission line survey allows the selection of galaxies by their emission line fluxes detected via narrow-band (Fabry-Perot) imaging, irrespective of their continuum brightness. Galaxies with the [O III] λ 5007 line detected in FP-A or FP-B offer the best opportunity to select metal-poor objects, since the [O II] λ 3727 line shows up in a veto filter of CADIS; because the ionization decreases with metallicity (Stasinska & Leitherer 1996), the flux ratio F([O III] λ 5007)/F([O II] λ 3727) is useful to select metal-poor galaxies.
The advantage of the CADIS survey compared to other surveys, which aim to determine the metallicities at medium redshift, is that the CADIS survey can reach galaxies with very low continuum brightness (and absolute luminosity), and galaxies which have a such faint continuum that they are only detectable by their emission lines. Fig. 2.3 illustrates this for galaxies selected by their [O III] λ 5007 line seen in FP scan. Thus, the detection of galaxies with faint $M_{\rm B}$ at medium redshift (down to SMC-like objects with $M_B \approx -17$) makes the emission line survey of CADIS much better suited for a study of the metallicity evolution with redshift than previous studies. Due to its faintness and the rejection of AGN-like SEDs in our multi-color analysis, the CADIS emission line galaxy sample is not contaminated by AGNs.

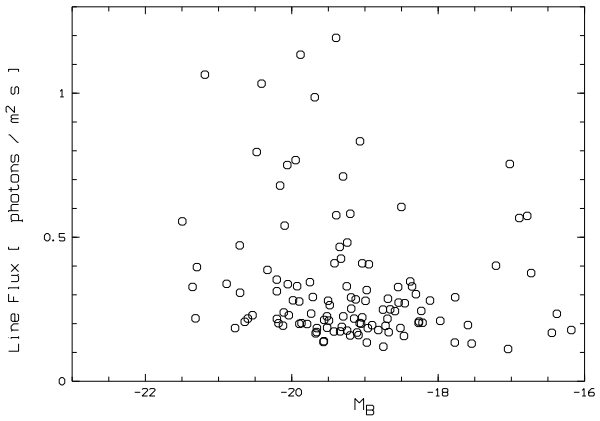

Figure 2.3 The diagram shows the line fluxes versus absolute magnitude M_B for the emission line galaxies in four CADIS fields with an [O III] λ 5007 line detected in FP-A or FP-B. The detection of an emission line is possible also for faint absolute magnitudes of galaxies at medium redshift.

In order to determine oxygen abundances at medium redshift, one needs the [O III] λ 5007, [O II] λ 3727, and Hβ lines (see section 2.6.2.1). For galaxies selected by their [O III] λ 5007 line seen in the FP scan, [O II] λ 3727 is detected by a veto filter (see examples below). However, since the determination of the [O II] λ 3727 flux relies on a medium band filter only, this flux is not accurate enough to determine oxygen abundances. Therefore, spectroscopic follow-up of candidates for metal-poor galaxies is necessary, in order to measure the [O II] λ 3727 and Hβ lines needed to determine oxygen abundances using the R_{23} relation (equation 2.16).
Fig. 2.4 and 2.5 show two examples of galaxies detected by their [O III] λ 5007 emission line detected in the FP scan. The [O III] λ 5007 line of the galaxy 09h-5068 (Fig. 2.4) is

detected in the FP window A, and we detect the [O II] λ 3727 line in the veto filter V522. Moreover, the Hα and [N II] $\lambda\lambda$ 6548, 6584 lines are seen in window C. For the galaxy 01h-979 (Fig. 2.5), the [O III] λ 5007 line is seen by the Fabry-Perot in window B, and we detect the [O II] λ 3727 line in the veto filter V611. Such galaxies selected by [O III] λ 5007 emission in the FP windows A or B have redshifts $z = 0.400 \pm 0.012$, and $z = 0.636 \pm 0.010$, respectively.

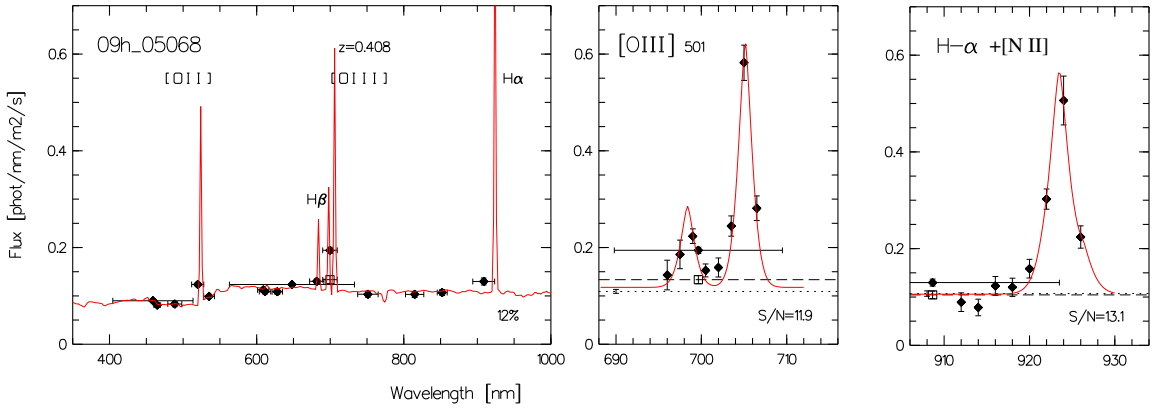

Figure 2.4 The galaxy 09h-5068 at $z = 0.409$: Photometry in all 14 optical CADIS filters fitted by a continuum-model (left panel), the Fabry-Perot measurements in window A with a [OIII] doublet profile fitted to the observed flux data (center), and the Fabry-Perot measurements in window C with a Hα + [N II] $\lambda\lambda$ 6548, 6584 three-line profile fitted to the observed flux data (right panel).

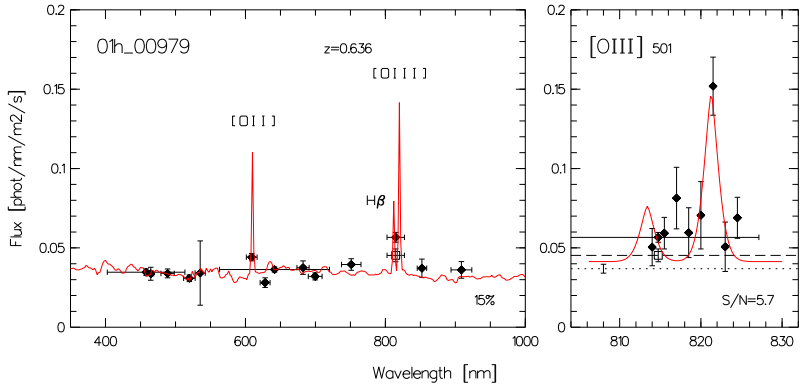

Figure 2.5 The galaxy 01h-979 at $z = 0.636$: Photometry in all 14 optical CADIS filters fitted by a continuum-model (left panel), and the Fabry-Perot measurements in window B with a [OIII] doublet profile fitted to the observed flux data (right panel).

In four reduced fields we have selected 129 galaxies by the [O III] λ 5007 line in FP-A or FP-B, of which 77 galaxies have a F([OIII])/F([OII]) line ratio > 2. As an example, galaxies detected by the [O III] λ 5007 line in FP-A, denoted as squares in the left panel of Fig. 1.15 (chapter 1), are primary candidates for metal poor galaxies if they lie on the left side of the dotted line.

2.3. Spectroscopic Observations

2.3.1. Observations with the VLT

The primary targets in the equatorial fields (01h- and 23h- field) were observed with the **FO**cal **R**educer and low dispersion **S**pectrograph (FORS 2) at the **V**ery **L**arge **T**elescope (VLT) in service mode in summer 2001, and in visitor mode in October 2001. Some properties of FORS 2 are given in Tab. 2.1.

Area CCD	2048×2048
Pixel Size	$24 \mu m$
Pixel Scale	$\sim 0''.2$/pixel
Field of View	$6'.8 \times 6'.8$
Gain	1.85 e^- ADU^{-1}
Read-noise	5.2 e^-

Grism	λ_{cent} [nm]	Wavelength range [nm]	Dispersion [nm/pixel]	Resolution ($\lambda/\Delta\lambda$)	Order separation filters
300I	860	600−1100	0.259	680	OG590+32
600RI	663	530−800	0.132	1011	GG435+81
600R	627	525−745	0.108	1230	GG435+81
600B	465	345−590	0.120	815	none

Table 2.1 Characterstics of the CCD (left) and FORS 2 grisms (right). The table lists the resolution achieved for $1''$ slit with the standard resolution collimator. The wavelength range corresponds to a slit which is located in the field center.

Field	Mask	Date	N	t_{total}(s)	Grism
01h	1	2001 Jul. 16/17	1×2680 s		300I
	1	2001 Sep. 17/18	1×2680 s		300I
	1	2001 Oct. 10/11	3×2500 s	12860	300I
01h	2	2001 Oct. 09/10	4×2500 s		600RI
	2	2001 Oct. 10/11	1×2500 s	12500	600RI
	2	2001 Oct. 09/10	3×1700 s	7500	600R
01h	3	2001 Oct. 10/11	2×2500 s + 1×1085 s	6085	600RI
	3	2001 Oct. 10/11	1×1700 s	5100	600RI
23h	1	2001 Jul. 13/14	4×2680 s		300I
	1	2001 Jul. 14/15	2×2680 s	16080	300I
23h	2	2001 Oct. 09/10	2×2500 s		600RI
	2	2001 Oct. 10/11	1×2500 s+ 1×1500 s	9000	600RI
	2	2001 Oct. 09/10	1×1700 s		600B
	2	2001 Oct. 10/11	1×1700 s	3400	600B

Table 2.2 Spectroscopic follow-up observations of 01h- and 23h-field using FORS 2 at the VLT. Column t_{total} lists the total integration time for each individual mask-grism configuration.

FORS 2 has a Mask eXchange Unit (MXU) which is a magazine holding up to 10 masks, laser-cut by the Mask Manufacturing Unit of the VIMOS and NIRMOS instruments. The masks were designed using the FORS Instrument Mask Simulator (FIMS). FIMS is a graphical user interface which shows the FORS sky field, and allows the precise positioning of MXU masks. Because we wanted to observe emission line galaxies with faint continuum ($R > 26$), which are not visible on pre-images, we had to use an input catalog containing emission line galaxies and reference stars in the "frameless mode" of FIMS. "Autoslit" was used in order to position the slits. The slitmasks contained $1.0''$ wide slits of length between $10''$ and $20''$. The position angle of each mask was chosen to maximize the

number of primary targets in the $6.8' \times 6.8'$ FORS field of view while simultaneously getting the wavelength range required to see the [O III] $\lambda\lambda$ 4959, 5007, [O II] λ 3727, and Hβ lines. These lines are required in order to use the R_{23} relation to determine the oxygen abundance of galaxies (see section 2.6.2.1). Regions of the slitmasks not devoted to primary targets were used to obtain spectra of other emission line galaxies. Table 2.2 shows the exposures time for the different masks and different grisms.
The different grisms and 2048 $\times$ 2048 CCD with $0.2''$ in the spatial direction allowed us to cover the wavelength range 600−830 nm needed to measure the [O III] $\lambda\lambda$ 4959, 5007, Hβ, and [O II] λ 3727 lines of galaxies at $z \approx 0.63$. Depending on the distribution of candidates, we used different grisms. The 300I grism gives a spectral resolution of about 1.2 nm, at 800 nm, for slitlets $1''$ wide. It allows more freedom in target positions than the 600RI grism, if one is interested in measuring the [O III] $\lambda\lambda$ 4959, 5007, [O II] λ 3727, and Hβ lines of a galaxy at $z \approx 0.63$. The 600RI grism gives a higher spectral resolution of about 0.8 nm at 800 nm, for slitlets $1''$ wide. But it allows less freedom in target positions, and one can measure only the [O III] $\lambda\lambda$ 4959, 5007 and Hβ lines of a galaxy at $z \approx 0.63$. In order to get [O II] λ 3727, the 600R grism has to be used additionally to the grism 600RI. The 600R grism gives a spectral resolution of about 0.5 nm FWHM, at 600 nm, for slitlets $1''$ wide. The reason for two grisms instead of one was to get a better resolution for the Hβ line. For galaxies at $z \approx 0.63$, the Hβ line lies between OH night sky lines, so a good resolution is helpful for the purpose of separating Hβ from neighbouring sky lines.
Absolute magnitudes and line ratios for galaxies at $z \approx 0.63$ observed with the VLT are given in Tab. 2.3, and some spectra are showed in Appendix A.

#	z_{spec}	M_B	$I_{[OIII]5007}$	[O III] λ 4959	Hβ	[O II] λ 3727	Hγ	$\log R_{23}$
01h-			phot $m^{-2}s^{-1}$	$I/I_{[OIII]5007}$	$I/I_{[OIII]}$	$I/I_{[OIII]}$	$I/I_{[OIII]}$	
979	0.6358	−19.5	0.34	0.32	0.25	0.63	0.08	0.89
1017	0.6372	−19.4	0.40	0.35	0.27	0.80	0.11	0.90
3517	0.6353	−18.5	0.12	0.36	0.12	0.02	0.06	1.06
3750	0.6352	−18.9	0.66	0.42	0.27	0.43	0.13	0.84
21585	0.6390	−17.6	0.19	0.33	0.21	0.08	0.06	0.83
5085	0.6221	−18.7	3.51	0.44	0.20	0.35	0.12	0.95
23h-								
1937	0.6390	−18.9	0.33	0.28	0.20	0.15	0.08	0.85
3134	0.6275	−21.7	0.50	0.32	1.44	4.60	0.32	0.61
4237	0.6440	−19.5	0.40	0.33	0.30	0.90	0.14	0.87
8843	0.6217	−20.5	0.54	0.29	0.26	1.48	0.08	1.03
21315	0.6390	−17.8	0.27	0.33	0.18	0.10	0.05	0.90

Table 2.3 Emission line galaxies in 01h- and 23h-field with the [O III] λ 5007 detected in window B, and verified by follow-up spectroscopy with FORS 2 at VLT (except 01h-5085 which was observed with DOLORES at TNG). The [O II] λ 3727/[O III] λ 5007 line fluxes of 23h-3134 and 23h-8843 have been corrected for reddening (see text)

Two things should be noted about the fact that we only detected [O III] λ 5007 lines in FP-B with the VLT, and no [O III] λ 5007 line in FP-A. First, only half of the FP-A scan in 23h-field has been analysed by now. Second, there was a problem with the galaxies on the 23h-field mask number 2 observed in October 2001 (see Tab. 2.2), which contained mainly galaxies with an emission line seen in FP-A. The 600RI together with the 600B grism (spectral resolution of about 0.6 nm FWHM, at 500 nm for slitlets $1''$ wide) was

used. But unfortunately, none of the candidates for galaxies at $z = 0.4$ could be confirmed because a problem concerning FP-wavelength settings during survey observations of 23h-field, which was detected after the VLT observations. As a result, a line was mistakenly identified for a number of 23h-field objects in window A which were on the mask. Thus, we could identify only two bright [O II] $\lambda 3727$ emitters, and a probable Ly-α galaxy at $z \approx 4.8$ (see chapter 3) on mask 2 of 23h-field.

2.3.2. Data Reduction

2.3.2.1. Bias and Flatfields

Spectra were reduced using the package LONG provided by MIDAS. Images were bias-subtracted first. Every mask contained $\approx$ 20 single spectra. Every single spectra was extracted, and treated as a long slit spectra, also the respective flatfield.
The lamps used for the internal screen flatfields have had uneven spectral emissivity. Combined with the uneven spectral sensitivity of the spectrograph and detector this results in flatfields which have very different intensities in different spectral regions. In order to remove these low spatial frequencies along the dispersion axis from the flat field, we averaged the original image along the slit, fitted the resulting one-dimensional image by a polynomial of second order, and divided the original flat field by this image to obtain a normalized flatfield. Every spectra was than divided through the respective normalized flatfield. After flatfielding, the cosmic ray rejection was done using a $\kappa\sigma$ clipping.

2.3.2.2. Wavelength Calibration

For the wavelength calibration night sky lines were used, which have the advantage to be taken with the telescope and spectrograph in the same orientation as the science spectra. Night sky emission lines were selected along the dispersion direction. In order to improve the signal-to-noise ratio of each row, some adjacent rows were averaged before searching the line. The line center was determined by fitting Gaussians to the line profiles. Then, in order to compute the dispersion relation, the lines found were cross-identified with a reference catalog containing night sky emission lines from the night-sky spectral atlas of Osterbrock et al. (1996). A two-dimensional polynomial function (a polynom 4th-order in X- and 2nd order in the Y-direction) was fitted to wavelength as a function of pixel position. This was used to transform the spectra to a linear wavelength scale. The accuracy of the wavelength calibration is ~ 0.1 nm for the 300I grism and ~ 0.05 nm for the 600RI, 600R and 300I grisms.

2.3.2.3. Sky Subtraction and Extraction of the Spectrum

The sky was measured in two regions located below and above the object spectrum. Then an independent profile was fitted for every column and the sky was subtracted from the object spectrum using the algorithm by Horne (1986). The one-dimensional spectra of each object were extracted with an aperture of about 10 pixels, i.e., about $2''$. The rows of the spectrum were added with weights which were chosen for optimal S/N-ratio of the resulting spectrum, while simultaneously preserving its photometric accuracy. For objects with faint continuum an artificial continuum has been constructed, with a Gaussian profile in the slit direction, in order to allow the Horne algorithm to work properly, assigning lower weights to the noisy pixels far from the center of the spatial profile.

2.3.2.4. Flux Calibration

Fluxes were calibrated from digital units (ADUs) to physical flux units (phot m^{-2} s^{-1}) using multiple observations of the spectrophotometric standard stars LTT 7379, EG 274 and LTT 7987 (Hamuy et al. 1992, 1994). Since the spatial profile of star spectra are Gaussian, object limits separated by three times the full width at half maximum were chosen for extracting the one-dimensional standard star spectra, which enclose over 99 % of the starlight. Before flux calibration, objects and standard stars spectra were corrected for atmospheric extinction which is about 0.12 mag/airmass at 520 nm, and about 0.02 mag/airmass at 820 nm. The three flux standard stars were measured at widely spaced wavelengths (5 nm), and the sensitivity function of the instrument was determined by fitting a spline to the flux points. The resulting spectrophotometric calibration yielded uncertainties in the relative fluxes of order of $4-5$ %.
Resulting flux calibrated one-dimensional spectra for some emission line galaxies (not corrected for reddening) are shown in Appendix A.

2.3.3. Observations with the Telescopio Nazionale Galileo

Galaxies selected by [O III] λ 5007 emission in the atmospheric window A in 09h-field were observed with the Low Resolution Spectrograph DOLORES at Telescopio Nazionale Galileo (TNG) in the night January 13th/14th, 2002. Some properties of DOLORES are given in Tab. 2.4.

Area CCD	2048 × 2048
Pixel Size	$15\mu m$
Pixel Scale	$\sim 0''.275$/pixel
Field of View	$9'.4 \times 6'.$
Gain	0.97 e^- ADU^{-1}
Read-noise	9 e^-

Grism	λ_{cent} [nm]	Wavelength range [nm]	Dispersion [nm/pixel]	Res.(nm) (for $1''$ slit)	Order separation filters
HR-R	700	620−780	0.08	0.3	none
MR-B	525	350−700	0.17	0.6	none
LR-R	740	447−1037	0.29	1.1	HP5000

Table 2.4 Characterstics of the CCD (left) and DOLORES grisms (right). The wavelength range corresponds to a slit which is located in the field center.

The masks were designed using the "blind mode" which use a catalog of objects with accurate coordinates in order to position the slits. The slitmasks for the 09h-field contained slits of width $1''.6$ and length $\sim 12''$. Tab. 2.5 shows the exposure times for the different masks and different grisms.

Field	Date	N	t_{total}(s)	Grism
09h	2002 Jan. 13/14	4×3000 s + 1×3600 s	15600	HR-R
	2002 Jan. 13/14	1×3000 s	3000	MR-B
	2002 Jan. 13/14	1×3000 s	3000	LR-R
01h	2002 Jan. 13/14	2×3000 s	6000	LR-R

Table 2.5 Spectroscopic follow-up observations of 09h- and 01h-field using TNG with DOLORES.

The average seeing during the observations was $1.3''$. The HRR and the MRB grism allowed us to cover the wavelength range 650−730 nm, and 490−600 nm, respectively, needed to get the lines required to measure oxygen abundances using the R_{23} relation (section 2.6.2.1).

Two exposures (each 3000 s) were taken with the LRR grism and 1.1″slit at the beginning of the night in order to bridge the time gap until the 09h field was observable. This integration time together with the bad seeing allowed us to get enough signal-to-noise only for the galaxy 01h-5085 (see Fig. 2.6), which shows a very bright [O III] λ5007 emission line in window B. This object is emitting $\sim 10^{35}$ W in its [O III] $\lambda\lambda$4959, 5007 line from a giant HII region or nuclear starburst, being one of those rare objects mentioned by Balzano (1983).
Data reduction of the spectra was performed similar to the VLT data reduction. For the flux calibration the spectrophotometric standard star HD93521 measured at 1 nm spaced wavelengths (Oke 1990) was used. Properties of galaxies at $z \approx 0.4$ observed with TNG are given in Tab. 2.6, and some flux calibrated spectra (not corrected for reddening) are showed in Appendix A.

#	z_{spec}	M_B	$I_{[OIII]5007}$	[O III] λ4959	Hβ	[O II] λ3727	log R_{23}
09h-field			phot $m^{-2}s^{-1}$	$I/I_{[OIII]5007}$	$I/I_{[OIII]5007}$	$I/I_{[OIII]5007}$	
3847	0.4060	−19.2	0.25	0.36	0.35	0.52	0.73
3869	0.3975	−20.6	0.25	0.36	0.72	1.76	0.64
4207	0.4060	−19.3	0.24	0.33	0.32	0.83	0.83
4319	0.3985	−18.4	1.45	0.42	0.33	0.09	0.77
4766	0.4080	−19.4	0.12	0.35	0.40	1.42	0.84
5068	0.4080	−19.5	1.13	0.38	0.42	0.67	0.69
8327	0.4090	−18.7	1.45	0.31	0.34	1.10	0.85

Table 2.6 Emission line galaxies in 09h-field with the [O III] λ5007 detected in window A, and verified by follow-up spectroscopy with DOLORES at TNG. The [O II] λ3727/[O III] λ5007 line flux of 09h-3869 has been corrected for reddening (see text).

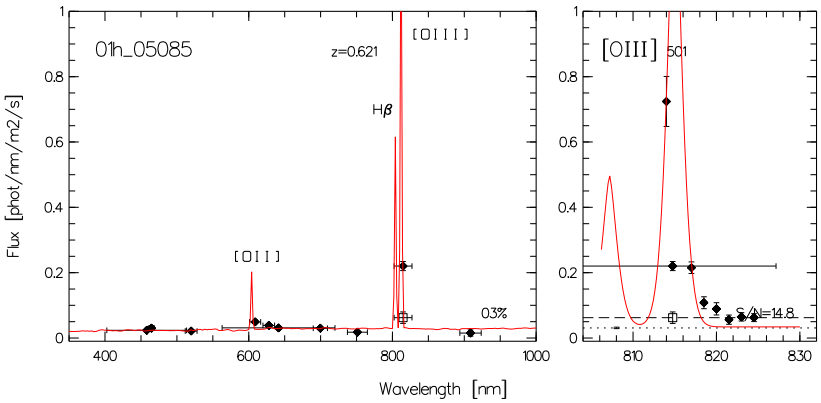

Figure 2.6 The galaxy 01h-5085 at $z = 0.622$ which shows a very bright [O III] λ5007 emission line. Photometry in all 14 optical CADIS filters fitted by a continuum-model (left) and the Fabry-Perot measurements in window B with a [OIII] doublet profile fitted to the observed flux data (right).

2.3.4. Observations with the Keck Telescope

On November 25th 2000, during a programme for EROS spectroscopy in the CADIS 09h-field with the Keck II telescope (D. Thompson), four 09h-field galaxies at $z \approx 0.4$ (09h-

3847, 09h-4207, 09h-4766, and 09h-5068) were put on free slits of one mask observed with the Low Resolution Imaging Spectrometer (LRIS). The backside-illuminated Tek 2048 × 2048 CCD detector providing an imaging scale of $0.215''$/pixel, and the 600/1 grating (0.128 nm/pixel) were used for the observations. 4 exposures of 1200 s each has been taken using a mask with a slit width of $2''$. Data reduction was done similar to the VLT and Galileo observations, but no flux calibration was possible, because no spectrophotometric standard stars have been observed.
For three of the four galaxies (except 09h-4207, where the spectrum does not extend sufficiently towards the red) we could measure the Hα, and the [N II] λ6584 line, showing up at about 920 nm. Because these two lines lie close to each other, their line ratio could be determined without any flux calibration or extinction correction, and serve as additional criterion in order to measure oxygen abundances (see below).

2.4. Extinction

2.4.1. General Remarks about Extinction

The most obvious effect of interstellar dust is its extinction. This extinction in the ordinary optical region is due largely to scattering, but it is also partly due to absorption. It reduces the amount of light from a source shining through interstellar dust according to the equation:

$$I_\lambda = I_{\lambda_0} e^{-\tau_\lambda}, \tag{2.1}$$

where I_{λ_0} is the intensity that would reach the Earth in the absence of interstellar extinction along the line of sight, I_λ is the intensity actually observed, and τ_λ is the optical depth at the wavelength observed.
Measurements over the years for many stars at different wavelengths show that, in the optical region, the form of the wavelength dependence of the interstellar extinction is approximately the same for all stars, and only the amount of extinction varies, so that:

$$\tau(\lambda) = Cf(\lambda), \tag{2.2}$$

where the constatnt factor C depends on the star, but the function $f(\lambda)$ is the same for all stars. This implies physically (to first approximation) that the optical properties of dust are similar everywhere in the observed region of interstellar space. Figure 7.1 in Osterbrock (1989) shows the standard interstellar extinction curve as a function of wavelength.
The effect of reddening can be written as

$$\frac{I(\lambda)}{F(\lambda)} = \frac{I(\mathrm{H}\beta)}{F(\mathrm{H}\beta)} 10^{c(H\beta)f(\lambda)} \tag{2.3}$$

where $I(\lambda)$ is the dereddened flux at a given wavelength, $F(\lambda)$ is the observed flux at each wavelength, $c(\mathrm{H}\beta)$ is the logarithmic reddening parameter that describes the amount of reddening relative to Hβ, and $f(\lambda)$ is the wavelength-dependent reddening function. $f(\lambda)$ can be taken from Whitford (1958), and approximated in the whole spectral range to an accuracy better than 5% with the expression

$$f(\lambda) = 3.15854 \times 10^{-1.02109\lambda} - 1, \tag{2.4}$$

where λ is in units of μm (from Izotov et al. 1994).
The effect of reddening on the ratio Hα/Hβ can be written as

$$\frac{I(\mathrm{H}\alpha)}{I(\mathrm{H}\beta)} = \frac{F(\mathrm{H}\alpha)}{F(\mathrm{H}\beta)} 10^{c[f(H\alpha)-f(H\beta)]}. \tag{2.5}$$

The extinction at Hβ in magnitudes is $A_\beta = 2.5\,c$, where $c = log[I(\mathrm{H}\beta)/F(\mathrm{H}\beta)]$ (Miller & Mathews 1972).
The theoretical Balmer line ratios (Brocklehurst 1971, Hummer & Storey 1987) are not strongly dependent on the electron temperature of the nebula, so an initial guess of 10 000 K always produces reddening estimates not far from the best-fit values.

2.4.2. Extinction of Faint Emission Line Galaxies

The CADIS fields at galactic latitudes $|b| > 40°$are not significantly reddened by interstellar dust absorption in our Galaxy because they are placed in zero-reddening areas, i.e. local minima of the IRAS 100 μm maps with undetected fluxes (< 2MJy/sterad). This should limit the extinction to $A_V < 0.2$, where $A_V = -2.5 \log \mathrm{e}^{-\tau} = 1.08\tau$ gives the visual extinction in magnitudes. Thus, one can assume in a very good approximation that all of the extinction occurs within the target galaxy.
For galaxies at $z \approx 0.4$ we measure the Hα line in FP window C, when [O III] λ5007 is detected in FP window A (see for example Fig. 2.4). The TNG follow-up spectroscopy of galaxies at $z \approx 0.4$ delivered Hβ, so F(Hα)/F(Hβ) could be calculated for these galaxies. Adopting the case B Balmer recombination decrement, I(Hα)/I(Hβ)= 2.85 for T= 10^4K and $N_e = 10^4 \mathrm{cm}^{-3}$ (Brocklerhust 1971), we got from equation 2.5 a value for c, which is a measure of the extinction in the galaxy. It turned out that for all but one galaxy (09h-3869) the extinction can be neglected. 09h-3869 is the brightest galaxy of the $z = 0.4$ sample ($M_B \approx -20.6$), and for this galaxy we got $c = 0.67 \pm 0.17$.
For the line ratio [O III] $\lambda\lambda$ 4959, 5007/Hβ the extinction is negligible, because these lines lie close in wavelength to each other. For the [O II] λ 3727/[O III] λ 5007 ratio:

$$\frac{I([\mathrm{O\,II}]\,\lambda 3727)}{I([\mathrm{O\,III}]\,\lambda 5007)} = \frac{F([\mathrm{O\,II}]\,\lambda 3727)}{F([\mathrm{O\,III}]\,\lambda 5007)} 10^{c\cdot(f([OIII])-f([OII])} \tag{2.6}$$

Thus, the measured line flux F([O II] λ3727)/F([O III] λ5007) of 09h-3869 has to be corrected by a factor of ≈ 2 in order to get its unreddened value, which goes into the R_{23} relation (equation 2.16).
Since extinction is low for the faint galaxies at $z \approx 0.4$ with $M_B > -20$, we assumed that this is the case also for faint galaxies ($M_B > -20$) at $z \approx 0.63$. Moreover, if $F([\mathrm{O\,II}]\,\lambda 3727)/F([\mathrm{O\,III}]\,\lambda 5007)$ is small, which is the case for most of the galaxies of the $z \approx 0.63$ sample, extinction does not have a great effect for calculating R_{23} from equation 2.16, since all the lines except the fainter [O II] λ 3727 line lie close in wavelength to each other. For the two brighter galaxies at $z \approx 0.63$ (23h-3341, 23h-8843) we corrected, accordingly to the result for 09h-3869, the measured [O II] λ 3727 line flux by a factor of 2.

2.5. Measurement Uncertainties of the Emission Line Fluxes

2.5.1. Measurement Uncertainties

Emission line fluxes were measured using the *integrate/line* routine in MIDAS. The errors in the measurements were derived from repeated observations of the lines: for [O III] λ 5007, [O III] λ 4959, and [O II] λ 3727, 5%; for Hβ, 10 % or more, depending on the position of Hβ between the night sky lines. The error of R_{23} is normally dominated by the Hβ line.

2.5.2. Hβ Absorption

The real value of Hβ absorption equivalent width is uncertain,, and dependent on the age of the star formation burst. An equivalent width of 0.2 nm for the hydrogen absorption lines is representative of local irregular, HII and spiral galaxies, and has been calculated by many authors: e.g., McCall et al. (1985), Skillman & Kennicutt (1993), Izotov et al. (1994). Compared to the large equivalent widths of Hβ emission of the galaxies of our sample ($>$ 2 nm), this Hβ absorption can be neglected, because its effect is smaller than the error of Hβ, which is about 10%.

2.5.3. Comparison between Line Ratios from CADIS and Spectroscopy

First important result of the spectroscopic follow-up with VLT and TNG was that the spectroscopic [O III] λ 5007/[O II] λ 3727 line ratios are consistent with those estimated by CADIS. This is shown in Fig. 2.7, where the line ratio [O III] λ 5007/[O II] λ 3727 from CADIS is plotted versus VLT and TNG measurements for galaxies at $z \approx 0.64$ and $z \approx 0.4$, respectively.

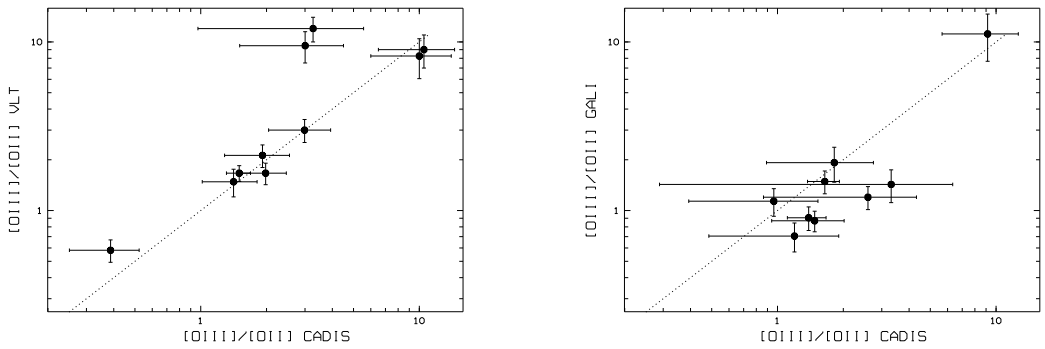

Figure 2.7 The line ratio [O III] λ 5007 / [O II] λ 3727 from CADIS vs. VLT (left panel) and TNG measurements (right panel) for galaxies at $z \approx 0.63$. The spectroscopic [O III]/[O II] line ratios are consistent with those from CADIS. All but two measurements agree within the error with a position on the dotted line, where the line ratio from CADIS is equal to the spectroscopic line ratio. The larger error bars for the CADIS measurements of [O III] λ 5007 / [O II] λ 3727 come from the determination of the [O II] λ 3727 flux, which relies on a medium band veto filter only. The two measurements in the left panel off the dotted line come from two very faint [O II] λ 3727 lines which cannot be measured reliably in the veto filters of CADIS.

2.6. Oxygen Abundance

In this section, the procedures for deriving the oxygen abundances are presented. The direct method of computing oxygen abundances (from [O III] λ 4363) is discussed in section 2.6.1 and the strong-line method of deriving oxygen abundances (in the absence of [O III] λ 4363) is in 2.6.2. Derived oxygen abundances for emission line galaxies at $z \approx 0.4$ and $z \approx 0.63$ are then presented in 2.6.3.

2.6.1. Direct Calibration

Methods to determine the metallicity from emission lines are well understood, and generally more reliable than those based on stellar absorption line data, because radiative transfer problems become less important. From all optical lines, oxygen lines are the most useful for measuring the abundance, since all important ionization stages can be observed, and no ionization correction factor, to account for ionization states without observed emission lines, is necessary.
The abundance of any ion relative to H^+ can be derived from the ratio of the intensity of an emission line at wavelength λ to the intensity of Hβ (see, e.g., Kobulnicky & Skillman 1996):

$$\frac{X(A^{+i})}{X(H^+)} = \frac{I(\lambda)}{I(\mathrm{H}\beta)} \frac{\epsilon(\mathrm{H}\beta)}{\epsilon(\lambda)} \tag{2.7}$$

Here X is the abundance by number of an ion A^{+i}, I is the intensity of a given emission line from that ion corrected for extinction relative to Hβ, and ϵ is the emissivity of the line. Hydrogen is assumed to be completely ionized, so that the abundance of an ion relative to H^+ gives the total abundance relative to hydrogen. Total elemental abundances, relative to H, are obtained by summing over all ionization states.
A few ions, e.g., [O III] and [N II], have energy-level structures that result in emission lines from two different upper levels with considerably different excitation energies occurring in the observable wavelength region. For example, [O III] λ 4363 comes from the upper ^{1}S level, while [O III] λ 5007 and [O III] λ 4959 come from the intermediate ^{1}D level (see Fig. 2.8). The relative rates of excitation of the ^{1}S and ^{1}D levels depend very strongly on temperature T_e, so the relative strength of the lines emitted by these levels may be used to measure the electron temperature.
A numerical approximation for the [O III] line ratio is (Osterbrock 1989):

$$R_{\mathrm{OIII}} = \frac{I_{\lambda 4959} + I_{\lambda 5007}}{I_{\lambda 4363}} = \frac{7.73 e^{32900/T_e}}{1 + 4.5 \times 10^{-4} (N_e / T_e^{1/2})}. \tag{2.8}$$

The average electron density N_e may be measured by observing the effects of collisional de-excitation. This can be done by comparing the intensities of two lines of the same ion emitted by different levels with nearly the same excitation energy, so that the relative excitation rates of the two levels depend only on the ratio of collision strengths. For example [O II] λ3729 and [O II] λ3726 (or [S II] λ6716 and [S II] λ6731) can be used to determine densities (see Osterbrock 1989). The electron densities derived from these lines may be used to correct the observations of the temperature-sensitive line [O III] λ 4363 for collisional

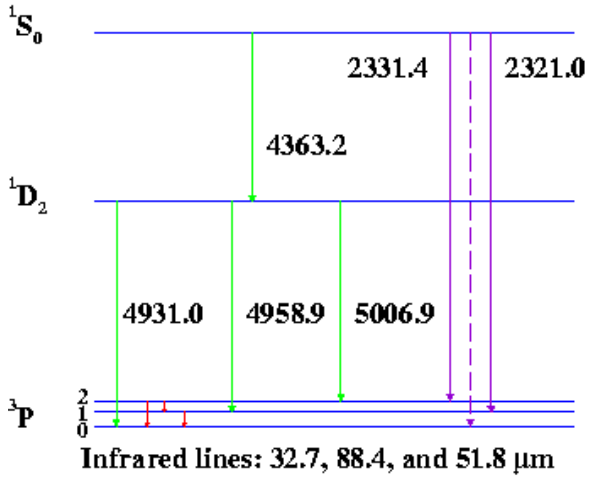

Figure 2.8 Energy-level diagram for O^{2+}.

de-excitation. Since electron densities for HII galaxies are of order $100\,\mathrm{cm}^{-3}$, and T_e of the order 10 000K (Shields 1990), equation 2.8 can be approximated by:

$$R_{\mathrm{OIII}} = \frac{I_{\lambda 4959} + I_{\lambda 5007}}{I_{\lambda 4363}} = 7.73\, e^{32900/T_e} \tag{2.9}$$

When [O III] $\lambda 5007$, [O III] $\lambda 4959$, and an upper limit for the weak [O III] $\lambda 4363$ line has been measured, an upper limit for T_e can be calculated:

$$T_e < 32900 \left(\ln \frac{7.73}{\mathrm{R_{OIII}}} \right)^{-1}. \tag{2.10}$$

Numerical models of HII regions have shown that there are differences between the temperatures in high- and low-ionization zones. To determine T_e([O II]) of the lower ionization zones, one can use the empirical fit to photoionization models form Pagel et al. (1992), and Skillman & Kennicutt (1993):

$$T_e(\mathrm{O}^+) = 2[T_e^{-1}(\mathrm{O}^{+2}) + 8 \times 10^{-5}]^{-1}. \tag{2.11}$$

The volume emission coefficient for a collisionally-excited line is given by (Garnett 2001):

$$\epsilon_{coll}(\lambda) = h\nu q_{coll}(\lambda) = \frac{hc}{\lambda} 8.63 \times 10^{-6} (\Omega/\omega_1) T_e^{-0.5} e^{-\chi/kT_e} \tag{2.12}$$

where Ω is the collision strength for the transition observed, ω_1 is the statistical weight of the lower level, and χ is the excitation energy for the upper level. Ω contains the physics: it represents the electron-ion collision cross-section averaged over a Maxwellian distribution of electron velocities relative to the target ion at the relevant temperature. The collision strengths must be calculated quantum-mechanically, and some of the most important numerical values can be found, e.g., in Osterbrock (1989), and Lennon & Burke (1994).

For recombination lines, the emission coefficient is given by

$$\epsilon_{rec}(\lambda) = h\nu q_{rec}(\lambda) = \frac{hc}{\lambda}\alpha_{\rm eff}(\lambda), \tag{2.13}$$

where $\alpha_{\rm eff}(\lambda)$ is the "effective" recombination coefficient for the recombination line λ. $\alpha_{\rm eff}(\lambda)$ incorporates the physics, including the cross-section for electron-ion recombination, and the probability that a given recombination will produce the given emission line; $\alpha_{\rm eff}$ varies roughly as T_e^{-1}.
When T_e has been determined for both zones, abundances for O^+ and O^{+2} can be derived using equation (7) and (8) from Pagel et al. (1992). The total oxygen abundance N(O)/N(H) is then obtained from the sum:

$$\frac{N(\mathrm{O})}{N(\mathrm{H})} = f \cdot \left(\frac{N(\mathrm{O}^+)}{N(\mathrm{H}^+)} + \frac{N(\mathrm{O}^{+2})}{N(\mathrm{H}^+)} \right), \tag{2.14}$$

where f is a ionization factor to account for unobserved oxygen ions. To correct for species more ionized than O^{+2}, and since the ionization potential of the O^{+2} ion is similar to the ionization potential of He^+, f may be written as

$$f = 1 + \frac{N(\mathrm{He}^{+2})}{N(\mathrm{He}^+)} \tag{2.15}$$

By analogy to ionized hydrogen, the ions He^+ and He^{+2} are traced by line emission from He^0 (He I) and He^+ (He II), respectively, which comes from the recombinations of He^+ and He^{+2} ions. The last term in equation 2.15 is zero, because emission from He II λ4686 is very weak or negligible in typical HII regions. Consequently, the contribution by O^{+3} (or higher ionized species) to the total oxygen abundance is negligible. Thus, the ionization factor for oxygen is $f = 1$.
It turns out that most of the common ions that dominate the nebular cooling rate have ground-state electron configurations with five low-lying levels like [O III] (Fig. 2.8). Higher levels in these ions are not significantly populated through collisions, recombinations or other mechanisms. For such ions, collisional, and radiative transitions can occur between any of the levels. Three-level and five-level atom approximations can be found in the literature, e.g., De Robertis et al. (1987), McCall (1984), and Shaw & Dufour (1995).

2.6.2. Empirical (Strong-Line) Calibrations

2.6.2.1. R_{23}*-method*

The temperature-sensitive [O III] λ4363 line is often too weak to be measured even in the local universe, either because the electron temperature is too low, or because the low signal-to-noise in the spectra of faint objects. Therefore, at higher redshift, empirical abundance indicators that use the strong forbidden lines must be used.
The ratio

$$\mathrm{R}_{23} = \frac{I([\mathrm{O\,II}]\,\lambda 3727) + I([\mathrm{O\,III}]\,\lambda\lambda 4959, 5007)}{I(\mathrm{H}\beta)} \tag{2.16}$$

has first been suggested by Pagel et al. (1979). They noted, based on a sample of extragalactic H II regions, that the measured T_e, O/H and R_{23} were all correlated. This works because of the relationship between O/H and nebular cooling: For metal-rich regions, the cooling in the ionized gas is dominated by emission in IR fine-structure lines

(primarily the [O III] 52 μm and 88 μm lines), so as O/H increases, the nebula becomes cooler. In response to that, the optical forbidden lines, especially the [O III] lines, becomes weaker as O/H increases (excitation goes down as T decreases). At very high abundances, $12+\log(\mathrm{O/H}) > 8.7$, HII regions are very cold ($T_e < 6000\,\mathrm{K}$) and values of R_{23} are small.

For $\log \mathrm{O/H} < -3.8$, the relation between R_{23} and O/H reverses, such that R_{23} decreases with decreasing abundance. This occurs because at very low metallicities the IR fine-structure lines no longer dominate the cooling since there are too few heavy elements. As a result, the forbidden lines more directly reflect the abundance in the gas.

Thus, the R_{23} indicator is not a monotonic function of oxygen abundance. At a given value of R_{23}, there are two possible choices of the oxygen abundance. Roughly, the low abundance or "lower branch" is defined by $12+\log(\mathrm{O/H}) < 8.2$, whereas the high abundance or "upper branch" is defined by $12+\log(\mathrm{O/H}) > 8.5$ (see Fig. 2.9). However, within the "turnaround" region $8.2 < 12+\log(\mathrm{O/H}) < 8.5$, the oxygen abundance changes rapidly with R_{23}. Thus, an additional indicator (e.g., the [N II] λ6584 line) is needed in order to resolve the degeneracy in R_{23}.

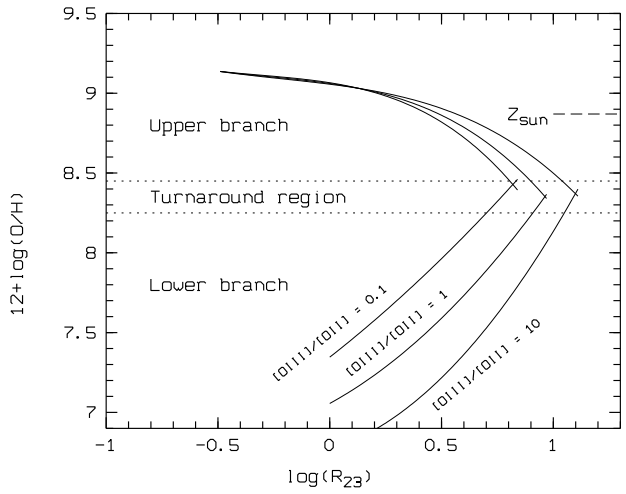

Figure 2.9 The oxygen abundance 12+log(O/H) as a function of the line ratio $\log \mathrm{R}_{23}$. The calibration between R_{23} and O/H (solid lines) using the models from McGaugh (1991) shows the effect of varying the ionization parameter in terms of the observable line ratio [O III] $\lambda\lambda$ 4959, 5007/[O II] λ 3727. On the lower, metal-poor branch, the ionization parameter becomes important. The ratio [O III]/[O II] of 10, 1.0, and 0.1 correspond (very roughly) to ionization parameters U of $10^{-1}, 10^{-2}$, and 10^{-4}. The two horizontal dotted lines separate the different regions of oxygen abundances. The short horizontal dashed line shows the solar oxygen abundance of $12+\log(\mathrm{O/H}) = 8.87$ (Grevesse et al. 1996).

McGaugh (1991) refined the R_{23}-method to take into account the ionization factor U. The calibration between R_{23} and oxygen abundance was done based on a set of photoionisation models. Nebular spectra have been computed using HII region models specified by three parameters: the shape of the ionizing spectrum (T), the geometry of the nebula (U), and the abundance of the chemical elements in the gas (Z). Analytic expressions for the McGaugh (1991) calibration are found in Kobulnicky et al. (1999), both for the metal-poor (lower) branch:

$$\begin{aligned} 12+\log(\mathrm{O/H}) &= 12-4.944+0.767x+0.602x^2 \\ &\quad -y(0.29+0.332x-0.331x^2), \end{aligned} \tag{2.17}$$

and metal-rich (upper) branch:

$$\begin{aligned} 12+\log(\mathrm{O/H}) &= 12-2.939-0.2x-0.237x^2-0.305x^3-0.0283x^4 \\ &\quad -y(0.0047-0.0221x-0.102x^2-0.0817x^3-0.00717x^4), \end{aligned} \tag{2.18}$$

where x =log$\mathrm{R_{23}}$ and y =log(I([O III] $\lambda\lambda$ 4959, 5007)/I([O II] λ3727)). These analytic expression are shown as solid lines in Fig. 2.9.

2.6.3. Oxygen Abundances for our Sample

Because the faintness of the temperature-sensitive line [O III] λ 4363 , the oxygen abundance has to be determined using the empirical calibration between oxygen abundance and $\mathrm{R_{23}}$. The most significant uncertainty of the $\mathrm{R_{23}}$ relation comes from the decision, if an object lies on the upper, metal-rich branch, or on the lower, metal-poor branch of the curve (see Fig. 2.9). In the following we describe how oxygen abundances are derived from measured $\mathrm{R_{23}}$ values.

2.6.3.1. The [N II] λ6584/Hα *Ratio*

The [N II] λ6584/Hα line ratio can be used in order to break the degeneracy of the $\mathrm{R_{23}}$ relation, if one is able to measure and separate [N II] λ6584 from Hα. Denicolo et al. (2002) calibrated the N2 estimator, N2 = log(I([N II] λ6584)/I(Hα)), vs. the oxygen abundance (see solid line in Fig 2.10), using a sample of HII galaxies having accurate oxygen abundances, plus photoionization models covering a wide range of abundances.
When the secondary production of nitrogen dominates, at somewhat higher metallicity, the line ratio [N II] λ6584/Hα increases with oxygen abundance. At very low metallicity, N2 scales simply as the nitrogen abundance, to first order. However, in this metallicity regime, the nitrogen abundance shows a large scatter relative to the oxygen abundance, since the nitrogen abundance is much more sensitive to the history of star formation in the galaxy considered. As a result, this ratio is probably not very useful to estimate oxygen abundance except as a means of determining the branch for the application of the $\mathrm{R_{23}}$ method. The division between the upper and the lower branch of the $\mathrm{R_{23}}$ relation occurs around [N II] λ6584 /Hα $\sim$ 0.1. [N II] λ6584 /Hα line ratios were measured with Keck for three galaxies at $z \approx 0.4$ (09h-3847, 09h-4766, and 09h-5068), being > 0.1 for all of them, and placing these galaxies on the upper branch of the $\mathrm{R_{23}}$ relation (see Fig. 2.10).

2.6.3.2. Extreme [O III] λ5007/[O II] λ3727 *Flux Ratios*

The galaxies 09h-4319, 01h-21585, 23h-1937, and 23h-21315 show a high [O III] λ5007 to [O II] λ3727 flux ratio (> 5). If we put these galaxies on the upper branch, we would get metallicities of $0.5\,Z_\odot < Z < 1Z_\odot$. There are no galaxies in the local universe in this high metallicity range which show a such high [O III] λ5007/[O II] λ3727 ratio. Assuming that the physical properties of the interstellar medium are the same in the local universe and at medium redshift, these galaxies cannot have a such high metallicity. Therefore, we have to put them on the lower branch.

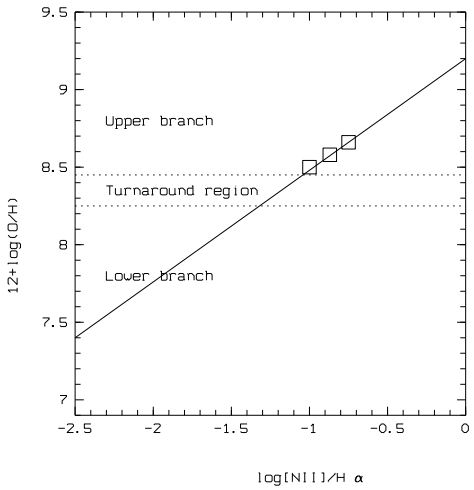

Figure 2.10 The oxygen abundance 12+log(O/H) vs. log([N II] λ6584/Hα). The solid line shows the calibration between 12+log(O/H) and log([N II] λ6584/Hα) from Denicolo et al. (2002); this relation actually has a larger scatter. The diagram can be used, however, to choose between the lower and upper branch of the R_{23} method: the three open squares are three galaxies with the [O III] λ5007 line seen in FP-A, and they can be put on the upper branch of the R_{23} relation.

2.6.3.3. Bright Galaxies

Three galaxies (09h-3869, 23h-3341, and 23h-8843) have absolute magnitudes $M_B < -20$. The R_{23} ratio of 23h-8843 places this galaxy in the turn-around region. The galaxies 09h-3869 and 23h-3341 would have a metallicity of $< 1/10 Z_\odot$ if we placed them on the lower branch. But their bright continuum and the extinction derived for 09h-3869 show that these galaxies already formed generations of stars which chemically enriched these systems, and lead to dust formation, so they cannot have a such a low metallicity. Therefore we placed these two galaxies on the upper branch.

2.6.3.4. Measured Oxygen Abundances

The remaining galaxies lie in (or near) the turn-around region. For every R_{23} ratio we get an upper and a lower value for O/H (vertical bars in Fig 2.11). Two galaxies,09h-2858 and 09h-5766, for which lines other than [O III] λ5007 have a low signal-to-noise, could have any metallicity between one-tenth solar and solar, so that we exclude them from the discussion of metallicities.

Fig. 2.11 shows that we have found galaxies at medium redshift with metallicties down to about $1/15 Z_\odot$. Several facts can explain the fact that we have not found any galaxies with very low metallicities ($< 1/20 Z_\odot$): first, there are only a few of such galaxies also in the local universe. Second, at medium redshift, the gas-to-stellar mass ratio of this type of galaxies can be much lower than in the local universe, resulting in very faint luminosities for these galaxies. Third, HII regions live only $\sim 10 - 50$ Myrs (assuming continuous star formation), so the time when they are visible is rather short. Moreover, bright HII regions are found around short lived massive stars.

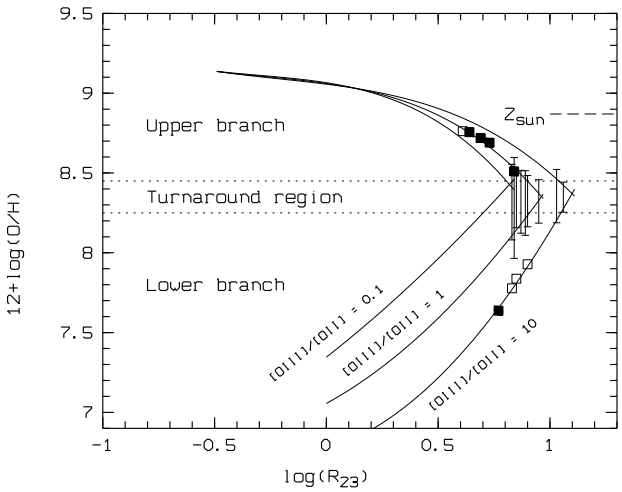

Figure 2.11 The oxygen abundance 12+log(O/H) as a function of the line ratio $\log R_{23}$. Open (filled) squares show oxygen abundances for galaxies observed with VLT (TNG). Vertical bars show the values allowed by the measured R_{23}, for galaxies which could not be definitely placed on the lower or upper branch. Typical uncertainties are 0.1 dex for the R_{23} indicator, and 0.2 dex for the oxygen abundance.

2.6.3.5. Upper Limits for [O III] λ 4363

The temperature-sensitive line [O III] λ 4363 is often too weak to be measured in the local universe, let alone at $z \gg 0$. An upper limit for the electron temperature can be derived from the equations 2.10 and 2.11, when an upper limit for [O III] λ 4363 line has been measured, e.g., for galaxies with detected Hγ line.

A two-sigma upper limit of the [O III] λ 4363 flux can be computed as the product $2.51Aw$, where A is two times the root-mean-square of the underlying continuum immediately surrounding the [O III] λ 4363 line, w is the full width at half maximum of the line obtained from a fit of the nearest strong line, and the numerical factor is the square root of 2π. Because of its close proximity, the width of $H\gamma$ can be adopted for the width of [O III] λ 4363. Then equation 2.7 can be used to calculate a *lower* limit for the oxygen abundance, which can possibly place the galaxy on the upper branch when using the empirical calibration. Unfortunately, the lower limits calculated for galaxies with detected Hγ from our sample still allow either the upper or lower branch, so we cannot use this criterion.

One problem with the measurement of [O III] λ 4363 is that at lower S/N noise spikes near the position of the line are mistaken as detections. Moreover, the [O III] λ 4363 is systematically overestimated in the presence of significant noise, since Gaussian fits to emission lines with very low S/N ratios are systematically biased towards larger values, resulting in a trend toward higher T_e at lower signal-to-noise ratios.

Therefore, we did not use any [O III] λ 4363 upper limits for measuring oxygen abundances.

2.7. Metallicity-Luminosity Relation

2.7.1. Metallicity-Luminosity Relation from Literature

Skillman et al. (1989) used metallicities from 20 nearby galaxies, with absolute magnitude between $M_B = -19$ to -10.5, to study the metallicity-luminosity relation. They calculated metallicities with the T_e method, and distances from Cepheid variables and group associations. A mean least-squares fit to the data (i.e., a fit obtained by treating first the abundance, and then the absolute magnitude as the independent variable, and averaging the results) yielded:

$$12 + \log(\mathrm{O/H}) = 5.50 - 0.153\mathrm{M_B}, \tag{2.19}$$

with an RMS deviation of 0.16 dex. Similary, Richer and McCall (1995) report a metallicity-luminosity relation for 18 nearby dwarf irregulars with $M_B = -18$ to -10.5 of

$$12 + \log(\mathrm{O/H}) = (5.67 \pm 0.48) - (0.147 \pm 0.029)\mathrm{M_B}, \tag{2.20}$$

with a dispersion that increases for $M_B > -15$.
Pilyugin & Ferrini (2000) combined the Richer and McCall data set with 13 objects from Garnett (1997), and included 17 objects from their own observations. These data, ranging in M_B from -21.5 to -10.5 have a metallicity-luminosity relation with a slope of -0.192.
Melbourne & Salzer (2002) combined Zaritsky data for 39 spirals with the Skillman et al. data finding a metallicity-luminosity relation given by

$$12 + \log(\mathrm{O/H}) = 4.53 - 0.210\mathrm{M_B}. \tag{2.21}$$

Melbourne & Salzer (2002) measured metallicities for 519 starburst galaxies, using T_e abundances for 12 galaxies, p-method abundances (Pilyugin 2000) for 13 galaxies and $\mathrm{R_{23}}$ abundances for 46 galaxies. Using the metallicities of these 71 galaxies [O III] $\lambda 5007/\mathrm{H}\beta$ and [N II] $\lambda 6584/\mathrm{H}\alpha$ were related to metallicity and used for measurements of abundances for the remaining 448 galaxies. They found a linear relation between metallicity and absolute magnitude given by:

$$12 + \log(\mathrm{O/H}) = 3.848 - 0.240\mathrm{M_B}. \tag{2.22}$$

2.7.2. Metallicity-Luminosity Relation using CADIS Data

With the analysed CADIS data we can study the metallicity-luminosity (mass) relation at a look-back time of 4.8 Gyr and 6.7 Gyr, for galaxies at $z = 0.4$ and $z = 0.64$, respectively ($H_0 = 62\,\mathrm{km\ s^{-1}\ Mpc^{-1}}$, $\Omega_M = 0.3$, $\Omega_\Lambda = 0.7$). Fig. 2.12 shows the oxygen abundance as a function of absolute magnitude for the two redshift bins, at $z \approx 0.4$, and $z \approx 0.64$, respectively. Filled squares are CADIS data, open squares the data points for brighter galaxies from Carollo & Lilly (2001) and Kobulnicky & Zaritsky (1999), respectively. The lines show the luminosity-metallicity relation from equation 2.19 (Skillman et al.), 2.21 (Zarisky & Skillman) and 2.22 (Melbourne & Salzer) for local irregular, starbursts and spiral galaxies.

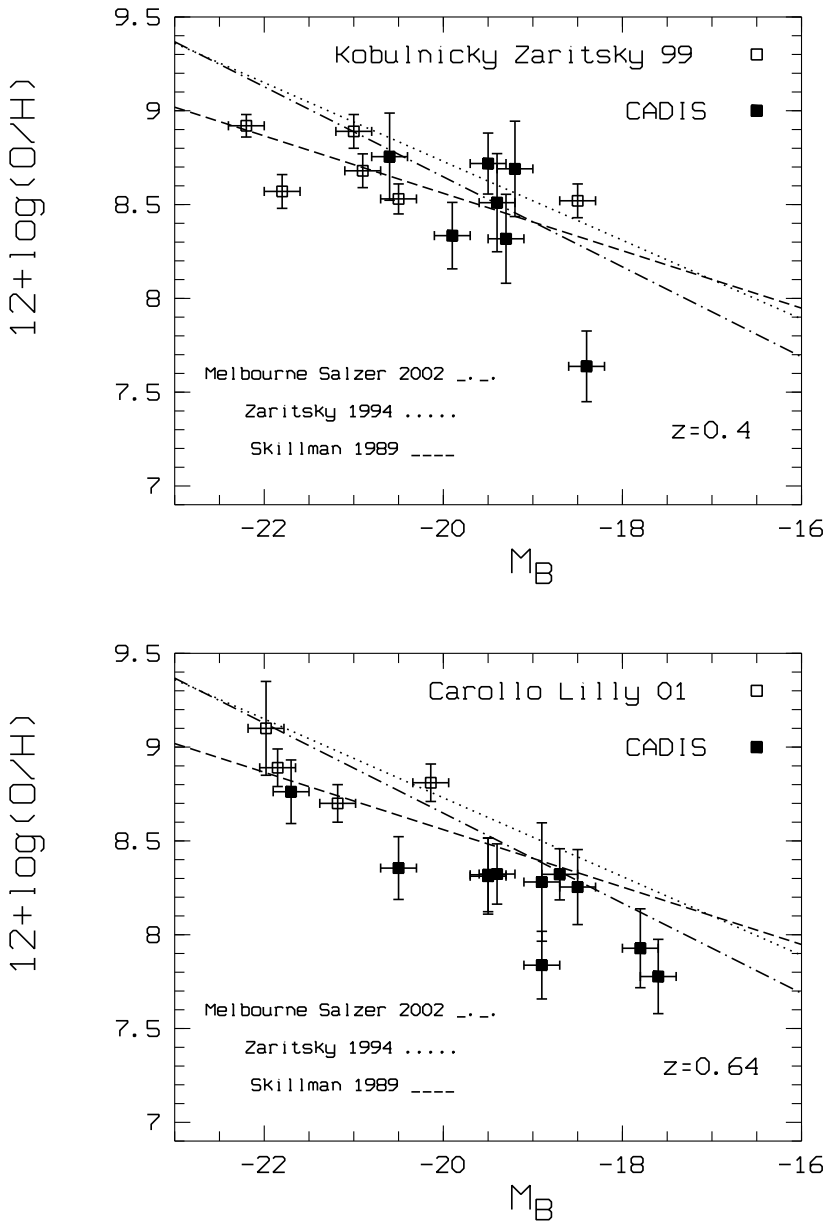

Figure 2.12 The oxygen abundance as a function of absolute magnitude, for $z \approx 0.4$ (upper panel) and $z \approx 0.64$ (lower panel). Filled squares are CADIS data, open squares the data points from literature. The lines show the luminosity-metallicity relation found by some authors for local galaxies; these relations actually show a scatter (see section 2.7.1 for details).

The CADIS galaxies at $z \approx 0.4$ occupy the same region in the $M_B - Z$ diagram as local galaxies, except the faint galaxy 09h-4319. Therefore, with the small sample of galaxies at $z \approx 0.4$, a clear statement about the metallicity - luminosity relation at $z \approx 0.4$ is not possible. Further spectroscopic observations of such galaxies should offer more clues about the behaviour of the metallicity-luminosity relation at $z \approx 0.4$.
On the other hand, for CADIS emission line galaxies at $z \approx 0.64$ we find a metallicity-luminosity relation with a slope very close to the one derived for local galaxies:

$$12 + \log(\mathrm{O/H}) = (4.56 \pm 1.22) - (0.191 \pm 0.064)\mathrm{M_B}. \qquad (2.23)$$

Thus, the correlation between galaxy metallicity and absolute magnitude M_B, known for galaxies in the local universe, apply also at redshift $z = 0.64$, at least for galaxies with absolute magnitudes from $M_B = -22$ to $M_B = -17.5$. It seems that the relation is slightly displaced to lower abundances: the most of the CADIS measurements in Fig.2.12, lower panel, lie under the metallicity-luminosity relation for local galaxies.

2.7.3. The Relation between Metallicity and Apparent K Magnitude

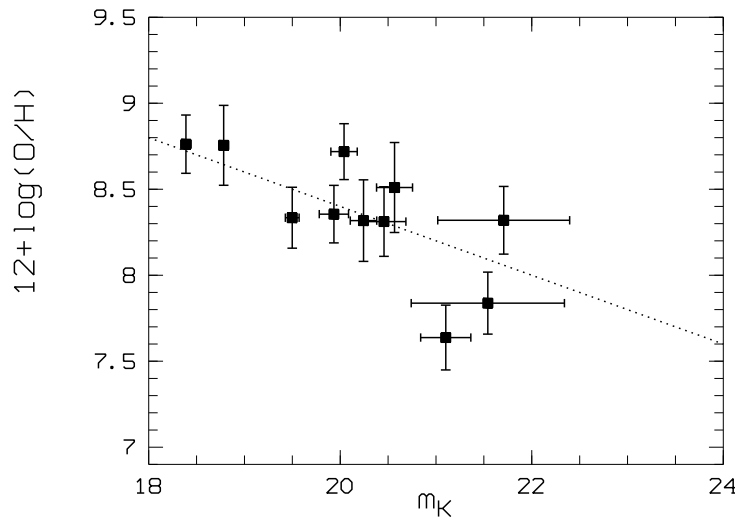

Figure 2.13 Oxygen abundance–m_K relation for CADIS galaxies at medium redshift.

A similar correlation, which can be tested with CADIS data, is the relation between metallicty and mass of galaxies. The determination of the total mass (baryonic plus the dark matter halo) seems out of reach for the moment except for local systems with tracers of the larger halo in which galaxies are thought to reside. Useful tracers here include the dynamical properties of satellite dwarf galaxies (Zaritsky et al. 1998) and globular clusters (Huchra et al. 1998). If one drops the requirement to measure the total mass and is willing to consider only the stellar mass, the near-infrared luminosity is of particular importance. Kauffmann & Charlot (1998) have demonstrated that the observed K luminosity is a good measure of its underlying mass regardless of how the mass assembled itself.
Fig. 2.13 shows the oxygen abundance versus the observed K-magnitude, m_K, for CADIS galaxies with measured metallicities at $z \approx 0.4$ and $z \approx 0.64$. Thus, our observations

indicate a relation between metallicity and $m_{\rm K}$, for galaxies at medium redshift, which can be also understood as a metallicity−stellar mass relation.

2.8. Summary and Discussion

We derived oxygen abundances of faint CADIS emission line galaxies ($M_B > -19$) at redshifts $0.38 < z < 0.42$ and $0.625 < z < 0.645$, using multi-object spectroscopy with FORS2 at VLT and with DOLORES at TNG. For galaxies with $0.38 < z < 0.42$ CADIS Fabry-Perot measurements of the Hα line (and low signal-to-noise [N II] λ 6584) exist. The extinction derived for these faint galaxies does not play a role for calculating R_{23} and deriving the oxygen abundance using the R_{23} method. Consequently, we assumed that the extinction is negligible also for faint galaxies in the redshift bin $0.625 < z < 0.645$ and derived their oxygen abundance. Combining our results with metallicities of brighter galaxies at medium redshift from the literature we have made first steps to study the metallicity-luminosity relation at medium redshift. Our observations indicate that the luminosity−metallicity and mass−metallicity relations apply not only in the local universe, but also at medium redshift. Therefore, oxygen abundances may serve as surrogates for luminosity and mass indicators when the latter are difficult to measure directly.
The emission line galaxies at $z \approx 0.4$ (except 09h-4319) for which we determined oxygen abundances (see upper panel in Fig. 2.12) occupy a similar locus in the metallicity-luminosity correlation as local galaxies. There is no indication of evolution at this look back time of about 5 Gyrs, but the galaxy sample is still to small to allow robust conclusions. In fact, the oxygen abundance for only one galaxy at $z \approx 0.4$ with $M_B > -19$ has been measured. This galaxy, 09h-4319, has the lowest oxygen abundance of all observed galaxies at $z \approx 0.4$. It appears 3 mag brighter than objects of similar metallicity in the local universe, as might be expected if a strong starburst has temporarily lowered its mass-to-light ratio. Another explanation for the location of 09h-4319 in the metallicity-luminosity diagram could be the fact that this galaxy has ejected metal-enriched gas because of galactic superwinds.
More conclusions can be derived from the metallicty-luminosity diagram at $z \approx 0.64$ (Fig. 2.12, lower panel). This diagram indicates that a metallicity-luminosity relation, similar to that found in the local universe, exists also at $z \approx 0.64$. The CADIS observations indicate that the metallicity-luminosity relation is slightly displaced to lower abundances. This could be due to the fact that galaxies at this look back time of about 7 Gyrs are not so evolved compared to the local universe, and had less time to produce metals. The metallicity-luminosity relation could possibly be displaced to even lower abundances at higher redshift, delivering a possible explanation of the lower oxygen abundances of bright galaxies at $z \approx 3$, found by Kobulnicky & Koo (2000), and Pettini et al. (2001).

2.9. Outlook

In order to determine more accurate abundances of a larger sample of CADIS emission line galaxies, the flux of Hα and [N II] λ6584, in addition to [O III] $\lambda\lambda$4959, 5007, [O II] λ3727, and Hβ lines, should be delivered by the next spectroscopic follow-up. The Hα line (together with Hβ) is needed to determine the extinction, and [N II] λ6584 (together with Hα) is important to determine the branch of the R_{23} relation (see Denicolo et al. 2002).

For galaxies at $z \approx 0.4$, follow-up spectroscopy, e.g., with FORS2 at VLT, can detect and measure these two lines (Hα and [N II] λ6584) in a wavelength window at bout 920 nm, which is free of atmospheric night sky emission lines. For emission line galaxies at $z > 0.42$ the Hα and [N II] λ6584 lines move into the wavelength range > 930 nm, such that near-infrared spectroscopy will be required in order to measure these lines.
Moreover, when [N II] λ6584 is detected, nitrogen-to-oxygen abundance ratios (N/O) may be determined using the algorithm proposed by Thurston et al. (1996), which only requires bright emission lines. The behaviour of N/O with increasing metallicity could offer clues about the chemical evolution history of the galaxies and the stellar populations responsible for producing oxygen and nitrogen. If oxygen and carbon are produced in previous generations, then nitrogen produced in new stars should be proportional to the initial heavy element abundance (i.e., *secondary* synthesis); N/O should increase linearly with O/H. On the other hand, if oxygen and carbon are produced in the same stars prior to the CNO cycle rather than in previous generations, then nitrogen production is independent of the initial heavy element abundance (*primary* synthesis); N/O is then constant with O/H. It will be thus interesting to study the behaviour of N/O with oxygen abundance at medium redshift and compare the results with local samples of galaxies to obtain additional clues about the origin of nitrogen, which has been a subject of debate for some years. The most metal poor galaxies should give the most stringent constrains about the origin of nitrogen, since the difference between the theoretical calculated *primary* and *primary* + *secondary* production of nitrogen becomes more obvious for metal poor galaxies (see, e.g., Contini et al. 2002).

The CADIS Search for Lyman-α-Galaxies at z > 4.7

Studies of the microwave background radiation reveal that the Universe is remarkably homogeneous at redshift $z \approx 1000$. Observations of the local Universe indicate that, by $z = 0$, much of the luminous matter had condensed into mature, gravitationally-bound structures. One of the primary challenges to astronomers today is to achieve a solid understanding of this process of galaxy formation and evolution. Locating and studying young galaxies at large look-back times is an essential aspect of this program.
A direct probe of galaxy formation is to determine the number counts and redshift evolution of nascent galaxies. The CADIS survey has been designed and executed to detect Ly-α galaxies at $z > 4.7$ by their strong emission lines which should be visible in the Fabry-Perot scan. The search for Ly-α galaxies with CADIS, a comparison with model predictions and observed number counts of galaxies at high redshift, and the implications for the epoch of galaxy formation are presented in this chapter.

3.1. Galaxies at $z > 5$

In the past couple of years substantial progress has been made in discovering galaxies at redshifts $z > 5$:

(i) Several galaxies at $z > 5$ have been detected and verified spectroscopically, e.g., Dey et al. 1998 (a galaxy at $z = 5.34$); Weyman et al. 1998 ($z = 5.6$); van Breughel et al. 1999; Hu et al. 1999 ($z = 5.74$); Hu et al. 2002 ($z = 6.56$); Ellis et al. 2001 ($z = 5.58$); Dawson et al. 2002 ($z = 5.19$); and Ajiki et al. 2002 ($z = 5.69$). One of these (van Breughel et al. 1999) is a radio galaxy at $z = 5.19$.

(ii) Quasars have been identified out to $z = 6.3$, e.g., Pentericci et al. 2002, and Fan et al. 2001.

These galaxy detections indicate that the first epoch of galaxy formation took place beyond redshifts $z \geq 5$. The existence of radio galaxies and quasars at $z > 5$ proves that even massive black holes had already formed at such high redshifts.

3.2. Spectral Features of Primeval Galaxies (PGs)

Theoretical considerations of the evolution of stellar populations in galaxies (e.g., Charlot & Fall 1993), and of the effects of the intervening intergalactic medium between us and the high-z galaxies (Madau 1995), permit detailed modeling of the expected spectral energy

distributions (SEDs) of primeval galaxies. According to these models, the most important features of the observable spectral energy distribution of high redshift, young star-forming galaxies, are:

(i) **Strong Ly-α emission**

Population synthesis models of Charlot & Fall (1993) predict that a young, dust free, star-forming galaxy (without an AGN) should show strong Ly-α emission with (intrinsic) equivalent widths in the range of 5-25 nm. The flux in the Ly-α line is expected to be directly proportional to the actual star formation rate (SFR) in the PG (see equation B.3), and 3 – 6 per cent of the bolometric luminosity is emitted in Ly-α.

A primeval galaxy can be considered, strongly simplified, as a giant HII region. UV radiation from hot stars, with surface temperatures $T_* \geq 3 \cdot 10^4$ K, photoionizes the hydrogen. Photons with energy greater than 13.6 eV, the ionization potential of H, are absorbed in this process, and the excess energy of each absorbed photon over the ionization potential appears as kinetic energy of a newly liberated photoelectron.

In the recombination process, recaptures of electrons occur to excited levels, and the excited atoms thus formed then decay to lower and lower levels by radiative transitions, eventually ending in the ground level. Recombination directly in the ground level, with principal quantum number $n = 1$, results in emission of a photon with energy > 13.6 eV which can be absorbed somewhere else in the nebula, photoionizing a neutral hydrogen atom. Recombination to excited levels, $n = 2, 3...$, leads to continuum emission: e.g., recombination to levels with $n = 2$ leads to Balmer continuum emission ($\lambda < 364.6$ nm), to levels with $n = 3$ to Paschen continuum emission ($\lambda < 820.3$ nm) etc. After recombination to levels with $n = 2$, a Ly-α photon with an energy of 10.15 eV is emitted because of the $n = 2$ to $n = 1$ transition. This Ly-α photon can be absorbed and emitted by other hydrogen atoms in the nebula, until it escapes after a "random walk". Recombination to levels $n \geq 3$ results in emission of Ly-α photons together with photons of the Balmer (Hα, Hβ, Hγ ...), Paschen etc. series.

The *Case B* approximation, which is a good approximation for HII regions, can be used to calculate the physical conditions within a primeval galaxy. Under *Case B* conditions, any photon emitted in an $n^2P \rightarrow 1^2S$ transition is immediately absorbed in the nebula, thus populating the n^2P level in another atom. *Case B* assumes that every Lyman-line photon is scattered many times and then converted into lower-series photons plus either Ly-α or two continuum photons.

Because Ly-α photons are resonantly scattered (10^6 to 10^7 times before they leave the HII-region), the probability that Ly-α photons are absorbed by dust is much higher than for continuum photons or photons of the Balmer lines. In the very first phase of star formation in galaxies, however, dust should not play a significant role. It has been demonstrated by Kudritzki et al. (2000) that the high Ly-α equivalent width of primeval galaxies can only arise in regions nearly free of dust. The presence of even small amounts of dust is a signature that one generation of stars has already formed. Therefore, strong Ly-α emission should be a property of the youngest objects, which

are just in the stage of forming their first generation of stars, and which have not yet enriched their interstellar medium with dust.

It should be also noted that some Ly-α galaxies (e.g., the galaxy at $z > 5$ found by Ajiki et al. 2002) show a sharp blue cutoff of the Ly-α emission line profile and broad red wing emission, features often observed in star-forming systems with prominent wind outflows. This line profile can be explained as follows. Generally the asymmetric Ly-α emission lines observed in high-redshift galaxies are attributed to the interaction of Lyman continuum photons generated by newborn stars with a galaxy-scale expanding shell of neutral hydrogen. For a sufficiently massive starburst, the hot ionized gas created in the vicinity of the stars vents into the halo of the galaxy, where it sweeps up neutral hydrogen into an optically thick shell. Recombination in the ionized gas converts Lyman continuum photons escaping from the surface of hot stars into line photons. Then, from the observer point of view, the near side of the expanding shell absorbs Ly-α photons on the blue side of the Ly-α emission line, causing a flux decrement on what would otherwhise be the blue wing of Ly-α emission. The far side of the shell scatters back Ly-α photons into the observer's line of sight. As these photons are offset redward from both the rest frame of the galaxy and the approaching side of neutral shell, they escape the galaxy and produce a pronounced red wing on the emission line profile. The net effect is the creation of a P Cygni profile for the Ly-α line.

(ii) **An intrinsically flat spectrum (F_ν) for $\lambda > 121.6$ nm**

The second special spectral feature expected for young star forming galaxies at high redshifts, which is also predicted by population syntheses models (Charlot & Fall 1993), is a remarkable flat spectral energy distribution ($F_\nu \approx$ const) between the Ly-α emission line ($\lambda = 121.6$ nm) and the Balmer-limit ($\lambda = 364.6$ nm), due to UV-radiation from hot, short-lived ($< 10^8$yr) massive stars. In the case of a constant SFR, although these stars have short lifetimes, an equilibrium between newly born and dying stars develops, so that their number, which is directly proportional to the SFR, stays constant. Measuring the intrinsic UV−flux of such a young star forming PG, which is redshifted into the optical or near-infrared for $z > 2$, could be therefore a direct measure of the instantaneous SFR within the system. But it is hard to observe the intrinsic UV spectrum of a primeval galaxy because of absorption from systems along the line of sight (property (iv)) and reddening, whose amount is not known. Therefore, the Ly-α emission line is a better tracer of star formation from primordial material.

(iii) **A pronounced drop of the spectral energy distribution at the Lyman limit**

The drop comes from a complete absence of flux at wavelength below the Lyman limit ($\lambda < 91.2$ nm) because of:

(a) An intrinsic drop in the spectra of hot O and B stars at the Ly-limit (Charlot & Fall 1993),

(b) Absorption by the neutral interstellar medium in the galaxy itself (Leitherer et al. 1995a, 1995b), and

(c) The Lyman-limit foreground systems close to the primeval galaxy, which produce more or less complete absorption below the Lyman limit in their rest frame.

(iv) **A continuum step across the Ly-α line**

The continuum step is due to photoelectric absorption from neutral hydrogen in the Ly-α clouds and Ly-limit systems along the line of sight. Ly-α clouds reside in the intergalactic medium, and have hydrogen column densities $10^{16} < N < 10^{19}\,\mathrm{m}^{-2}$. Lyman limit systems are believed to lie within haloes of dark matter, are optically thick, and have column densities $10^{19} < N < 10^{22}\,\mathrm{m}^{-2}$. Madau (1995) computed the HI opacity of a clumpy universe as a function of redshift, including scattering in resonant lines, such as Ly-α, Ly-β, Ly-γ, and higher order members, and Lyman-continuum absorption. At wavelengths short-ward of Ly-α in the emitter rest frame but long-ward of the Ly-limit, the source's continuum intensity is attenuated by the combined blanketing effect of many absorption lines of the Ly-forest (Ly-α, Ly-β, Ly-γ, Ly-δ ... line blanketing). Photons with wavelengths shorter than the Ly-limit in the emitter rest frame suffer from photoelectric continuum absorption from neutral hydrogen in the systems along the line of sight. Because the line-of-sight intervening HI absorption becomes more severe at higher redshifts, the effective break moves from the 91.2 nm Lyman limit to the Ly-α line at 121.6 nm.

Therefore, in order to find Ly-α galaxies at high redshift, CADIS searches for galaxies with a strong Ly-α emission line (property(i)) which show no flux at shorter wavelengths than the Ly-limit in the restframe of the galaxy (property(iii)). Because of absorption from neutral hydrogen in the line of sight between the Lyman-limit and Ly-α emission line (property (iv)), more or less no flux is expected also at $91.2\,\mathrm{nm} < \lambda < 121.6\,\mathrm{nm}$. At wavelengths between $\lambda > 121.6\,\mathrm{nm}$ and the Balmer-limit ($\lambda = 364.6\,\mathrm{nm}$) we expect a flat spectrum, which can be described by a power-law $I(\nu) \propto \nu^{-\alpha}$ with $\alpha = 0$ (property(ii)).

3.3. Lyman Break Galaxies

Based on the expected spectral property (iii) for high redshift star forming galaxies that they should show an obvious discontinuity in the far UV-spectrum at the limit of the Ly series near 91.2 nm (the so-called *Lyman break*), Steidel & Hamilton (1992, 1993) adopted a three filter system specifically tailored to detect this Lyman break in objects which are at $z \approx 3$. Fig. 3.1 (left panel) illustrates how the 3 filters sample the far – UV continuum of a galaxy near $z \approx 3$. Two of the filters (U_n and G) have passbands respectively below and above the Lyman-limit at $z \approx 3$, while the third filter, R, is further to the red. As Fig. 3.1 (right panel) shows, in deep images of the sky taken through these three filters, $z \approx 3$ galaxies are clearly distinguished from the bulk of lower redshift objects by their red ($U_n - G$) and blue ($G - R$) colours.
Using different filter systems, the original Lyman break selection technique of Steidel et al. can be extended to higher redshifts. Instead of looking for galaxies which exhibit the "break" in the U-band ("U-dropouts", $z \approx 3$) one can look for galaxies which show the

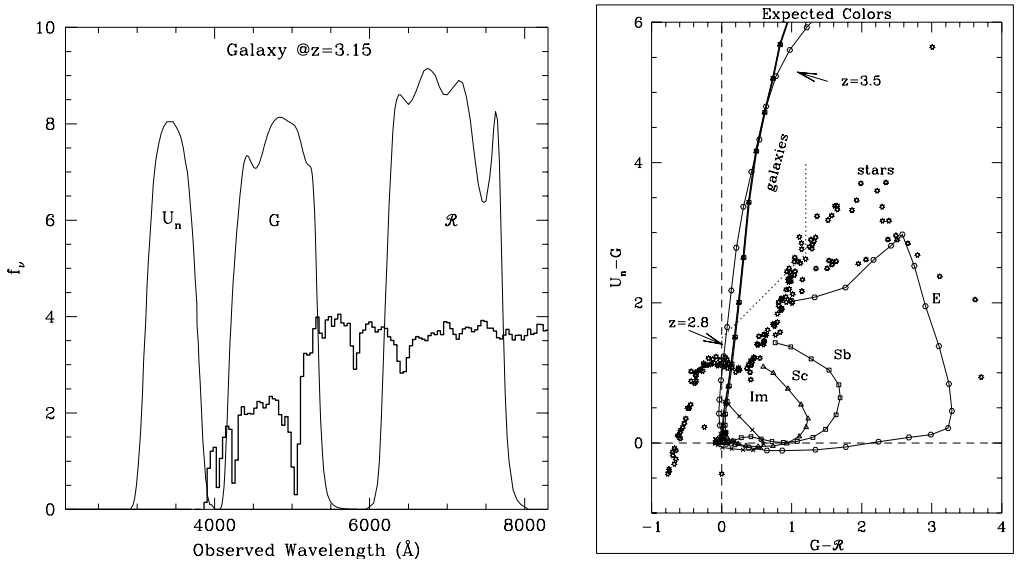

Figure 3.1 Detecting Lyman break galaxies. **Left panel:** Filter system used by Steidel et al. for observing the Lyman continuum break at $z \sim 3$, together with the model spectrum of a young star forming galaxy taking into account absorption properties of neutral hydrogen in the galaxy itself and the statistical effects of the intervening neutral hydrogen (reproduced from Steidel et al. 1998) **Right panel:** Colour evolution with redshift of galaxies of different spectroscopic type in the U_n, G, R filter systems used by Steidel et al. to search for Lyman break galaxies (reproduced from Pettini et al. 1997).

Lyman break in the B-band ("B-dropouts"), implying $z \approx 4$ (e.g., Steidel et al. 1999). Moreover, Weymann et al. (1998) were able to spectroscopically confirm a redshift of 5.60 for the galaxy HDF 4-473.0, which was selected as an "V-band dropout" in the HDF using the NICMOS F110W ($\sim$ J), and F160W ($\sim$H) observations of the HDF, together with the optical F606W (V), and F814W (I) HDF data. Interestingly, the galaxy HDF 4-473.0 turned out to be a Ly-α emitting galaxy. The multi-colour selection of high redshift objects using the Lyman break as a signature can thus be extended to very high redshifts, although spectroscopic verification becomes more difficult.
The Lyman break galaxies do not show, however, the properties expected for primeval galaxies. The strong metal absorption lines in their spectra indicate that they have already formed at least one generation of stars which has chemically enriched the systems and lead to dust formation, making Ly-α emission weak or undetectable. Earlier stages of evolution, before the formation of dust, may have much stronger Ly-α emission and fainter stellar continuua than the Lyman break galaxies at z $\approx$ 2.5...3.5, and may therefore be hard to pick out with the colour-break techniques.

3.4. A Connection Between Lyman Break Galaxies and Lyα Emitting Primeval Galaxies?

A question which naturally arises is about the connection between Lyman break galaxies and Lyα-emitting primeval galaxies. Thommes & Meisenheimer (2002) speculate about a connection between these two populations. They propose that young star forming galaxies

may go through two phases of Lyα emission:

- First there is the evolutionary phase immediately after the onset of star formation, in which dust does not play a role and strong outflowing winds have not yet developed. In this phase most of the Lyα photons are expected to be able to escape although they are resonantly scattered. Restframe Lyα equivalent widths of 10−20 nm are expected, based on the population synthesis models of Charlot & Fall (1993). However, according to the models of Friaça and Terlevich (1999), the interstellar medium will be enriched with metals very quickly after the onset of star formation. Due to ongoing dust formation, Lyα photons will be increasingly absorbed. Thus, this Lyα bright phase might be confined to a short period of only several hundred million years;

- A Lyα-dark phase could follow in which Lyα photons are destroyed by resonant scattering in a metal and dust-enriched interstellar medium. It is during this Lyα dark phase that the SFR might reach its maximum;

- Later on, strong outflowing winds may develop, initiating a second Lyα-bright phase. Lyα photons may now be able to escape again because they are back-scattered from the residing nebula shell and are therefore shifted in frequency space, allowing them to leave the interstellar medium without further resonant scattering. The Lyα line of objects in this second Lyα-bright phase should show a P Cygni profile, as discussed in section 3.2.

Thus, the Lyα-dark phase, together with the possible second Lyα-bright phase, might correspond to the evolutionary phases mainly detected by the Lyman break method. Objects during the first Lyα bright phase should not show strong metal absorption lines and the Lyα line should not show a P Cygni profile. However, the Lyα line is still expected to be asymmetric because parts of the blue side of the line emission will be eaten away by the Lyα-forest. In principle, high resolution, high signal-to-noise spectra of the objects may permit us the differentiation between Lyα emitting objects which are in their first or second Lyα-bright phase.

3.5. CADIS Goal

No galaxy at $z > 5$ was known 1997, the year of the revised proposal of CADIS. Since then, several galaxies at $z > 5$ have been found (see section 3.1), and the initial CADIS goal, to find Ly-α galaxies at high redshift (z $\geq$ 4.7), changed. The main objective of the search for Lyman-α-galaxies has become to determine the abundance of the first bursts of massive star formation in the young universe, which can set constraints to theoretical models of galaxy formation, and to investigate the early phases of the formation of massive galaxies like the Milky Way.
At $z = 4.7$, an $H_0 = 70$ km s^{-1} Mpc^{-1}, $\Omega_M = 0.3$, $\Omega_M = 0.7$ universe is only 1.2 Gyr old, corresponding to a look-back time of 90% of the age of the universe. Any object observed at this or an earlier epoch should be in its early youth.
CADIS selects galaxies by the extreme equivalent widths of their Lyman-α-emission ($W_{\lambda_{rest}} >$ 10 nm). Unlike similar programmes at 8−10 m telescopes, CADIS aims to find *the most*

luminous starbursts, with SFR $\geq 10 M_{\odot}$/year, which were possibly responsible for the formation of the galactic bulge. Even in the age of 10-m telescopes, only these luminous starbursts are accessible for detailed spectroscopic follow-up. With our detection limits in the range of 2.5 to $4 \times 10^{-20} \mathrm{Wm}^{-2}$ we are sensitive to galaxies which are brighter and rarer than those few objects at $z > 5$ found in systematic optical surveys (see below, Fig. 3.10). This bright, high-z region of the parameter space is absolutely essential for determining the luminosity function.

3.6. The CADIS Method

The optimal detection of a weak emission line galaxy superimposed on the bright night sky is reached when the instrumental resolution $\delta\lambda$ is adapted to the expected line width : $\delta\lambda \cong (1+z)(\Delta v/c)\lambda_0 \cong 0.9\,\mathrm{nm}$ for a Lyman-α emission line at $z = 6$. On the other hand, the detection probability increases with the observed volume $\Delta V \sim \Delta z \Delta\Omega \sim \Delta\lambda\Delta\Omega$, where $\Delta\Omega$ denotes the solid angle. Using a Fabry-Perot Etalon with $\Delta\lambda \cong 2\,\mathrm{nm}$, which is tunable in 9 steps and covers an interval of $12 - 15\,\mathrm{nm}$, CADIS provides an optimal mix of both sensitivity and search volume. The three wavelength intervals which are scanned by CADIS, FP-A at 700 nm, FP-B at 820 nm, and FP-C at 920 nm, are placed in windows free of night-sky emission lines and correspond to Lyman-α redshifts of $z \cong 4.8$, 5.7, and 6.6. The field size is $\Delta\Omega \approx 100\ \Box'$. Model predictions (Thommes & Meisenheimer 1995) of the galaxy abundance down to a line flux limit $\mathrm{F_{line}} \geq 3.0 \cdot 10^{-20}\,\mathrm{Wm}^{-2}$ (which can be reached with the Calar Alto 2.2- and 3.5-m telescopes in a few hours) made clear, before the project had even started, that at most a few Lyman-α galaxies would be expected per field and wavelength interval in the case of an open universe, which is indicated by the new measurements of $\Omega_M = 0.3$, $\Omega_\Lambda = 0.7$. Accordingly we are searching Ly-α galaxies in six fields.
After six years of observations on Calar Alto, 90% of the planned Fabry-Perot data have been obtained. The FP wavelength intervals which have been almost completely analysed are given in Tab. 1.3 (chapter 1), and the following results are based on these data. The analysis of interval C (with the aim of finding primeval galaxies) has been postponed for the moment because of technical problems (strong "fringing" in the CCD images), and low expectations of success on the basis of the present results (see section 3.9.3).

3.7. Selection of Lyman-α-Galaxies

The current classification of emission line galaxies shows that $>\sim 97.4\%$ of the emission line galaxies are foreground galaxies ($z < 1.2$), in which we mainly detect the lines Hα, Hβ, [O III] λ5007, and [O II] λ3727. Therefore, the main challenge is to separate the foreground objects from the Ly-α candidates. We identify Lyman-α-galaxy candidates among the emission line galaxies by the following exclusion criteria:
(1) The property (iii) for a primeval galaxy (section 3.2) requires that there is no flux below the Lyman limit. For $z > 4.7$ the Lyman limit lies at $\lambda > 520\,\mathrm{nm}$. Therefore, no flux should be detected in the CADIS B filter ($\lambda_{cent} = 461\,\mathrm{nm}$, FWHM= 113 nm). Accordingly, we require that $F_B < 2 \cdot \hat{\sigma}_B$, where F_B is the flux measured in the B filter, and $\hat{\sigma}_B$ its true overall error which takes into account both the calibration error and the scatter of the flux between the individual images. From 614 emission line galaxies selected

in four fields this criterion yields $N_{Noblue} = 85$ galaxies, i.e. 13.8% of the 614 emission line galaxies.

(2) Every single remained Ly-α candidate has to be carefully checked on the FP, pre-filter and R images because of the possible contamination by nearby bright objects. Candidates which are closer than about $3''$ to a bright object are spurious, and are removed from the list of candidates, since the photometry does not work well near bright objects. After this step, 5.7% of the emission line galaxies remain.

Table 3.1 Selection of Lyman-α-galaxy candidates; the selection steps (1)-(4) are described in the text.

Selection of objects without B-flux						Objects left after (2)		
Field	FP	Δz	N_{Elgal}	N_{Noblue} after (1)	$N_{Noblue-Contam}$ after (2)	N_{veto}	$N_{[O\,II]}$	$N_{Ly\alpha}$
01h	B	0.095	105	13	6	1	2	3
09h	A	0.082	90	27	6	3	1	2
09h	B	0.070	92	4	1	*	1	*
16h	B	0.095	108	8	3	*	1	2
23h	A	0.057	67	13	5	*	2	3
23h	B	0.082	152	20	14	2	6	6

(3) Foreground galaxies, for which we detect one of the prominent emission lines Hα, Hβ, [O III] λ5007, or [O II] λ3727 in the Fabry-Perot, can be excluded as soon a secondary emission line is detected in one of the veto filters (for details see section 1.3), leaving 4.7% of the galaxies.

(4) The distinction between a (rare) galaxy with bright [O II] λ3727 emission but weak UV continuum and a Lyman-α-galaxy is ambiguous based on the CADIS veto filters. Instead, we use the entire spectrum for this decision. Lyman-α galaxies at high redshift should distinguish themselves by a continuum step across the Lyman-α line (property (iv) from section 3.2). Therefore, the candidates which remain after step (3) are classified in two categories: probable Ly-α (see Tab. 3.2), if they show almost no continuum on the blue side of the Ly-α emission line, e.g., no significant flux in the R filter, and probable [O II] λ3727 objects (see Tab. 3.3). However, we need spectroscopic follow up observations of candidates belonging to both categories, since it cannot be excluded for sure, that there are Ly-α galaxies among the probable [O II] λ3727 objects. After this step, 16 Lyman-α-candidates (classified as probable Ly-α) remain, i.e., 2.6% of the emission line galaxies we found in four CADIS fields.

The number of galaxies left over after each selection step is shown in Tab. 3.1. We expect that the remaining list of robust Ly-α candidates is still contaminated by about 50%, predicted by the noise distributions (see Fig. 1.4). One source for the contamination are variable objects, e.g., supenovae or other "flaring" objects, which were only bright during the epoch of observations of one FPI wavelength (see section 1.10.4).

It should be also noted that the requirement (S1) for the selection of emission line galaxies (section 1.5) is more important for the selection of Ly-α candidates than the requirement (S3), i.e., $F_{line}/\sigma_{line} > K_{line}$. Ly$\alpha$ candidates show a very low flux in the pre-filter. Therefore, after the selection of objects with a flux greater than about 5σ for at least one

FPI	Field	NR	z	$F_{line}(Wm^{-2})$	$F(\lambda)/\sigma_F$
A	09h	21556	4.734	$5.7{\cdot}10^{-20}$	4.6
	23h	34751	4.772	$5.0{\cdot}10^{-20}$	4.8
	23h	34105	4.793	$4.2{\cdot}10^{-20}$	4.7
	23h	50707	4.801	$4.0{\cdot}10^{-20}$	5.1
	09h	38114	4.741	$3.7{\cdot}10^{-20}$	5.1
B	23h	40663	5.732	$6.4{\cdot}10^{-20}$	5.2
	23h	23836	5.705	$5.7{\cdot}10^{-20}$	5.1
	23h	28548	5.694	$5.6{\cdot}10^{-20}$	5.9
	23h	45745	5.733	$5.1{\cdot}10^{-20}$	5.6
	23h	9324	5.730	$4.8{\cdot}10^{-20}$	5.4
	16h	3171	5.746	$4.3{\cdot}10^{-20}$	5.0
	01h	3238	5.732	$4.1{\cdot}10^{-20}$	5.4
	23h	45065	5.735	$4.1{\cdot}10^{-20}$	5.1
	16h	2314	5.694	$3.4{\cdot}10^{-20}$	5.0
	01h	27927	5.677	$3.1{\cdot}10^{-20}$	5.3
	01h	28090	5.681	$2.9{\cdot}10^{-20}$	6.0

Table 3.2 The current list of 16 CADIS Lyman-α-candidates.

FPI	Field	NR	$z_{[O\,II]}$ ($z_{Ly\alpha}$)	$F_{line}(Wm^{-2})$	$F(\lambda)/\sigma_F$
A	23h	32692	0.891 (4.795)	$5.4{\cdot}10^{-20}$	4.8
	09h	6595	0.871 (4.736)	$4.5{\cdot}10^{-20}$	5.1
	23h	25107	0.896 (4.813)	$3.7{\cdot}10^{-20}$	4.8
B	23h	48878	1.189 (5.708)	$6.0{\cdot}10^{-20}$	5.3
	23h	30635	1.181 (5.685)	$5.4{\cdot}10^{-20}$	5.2
	23h	8007	1.204 (5.754)	$5.1{\cdot}10^{-20}$	5.0
	23h	31035	1.203 (5.751)	$4.8{\cdot}10^{-20}$	5.0
	23h	10053	1.181 (5.684)	$4.7{\cdot}10^{-20}$	5.0
	16h	1092	1.198 (5.694)	$4.6{\cdot}10^{-20}$	5.5
	09h	985	1.195 (5.728)	$4.4{\cdot}10^{-20}$	6.3
	01h	4616	1.198 (5.739)	$4.4{\cdot}10^{-20}$	5.6
	01h	1495	1.205 (5.759)	$4.2{\cdot}10^{-20}$	5.4
	23h	5705	1.206 (5.761)	$4.1{\cdot}10^{-20}$	5.5

Table 3.3 The current list of 13 CADIS probable [O II] λ3727 galaxies without blue continuum. A few of them could turn out to be Ly-α galaxies.

FP wavelength (criterion (S1)), fitting the Fabry-Perot instrument profile to the observed flux points results in a line flux F_{line} greater than about 4 σ_{line}, which is clear above the safe criterion of $K_{line} = 3.8$ (see section 1.10.1). Therefore, the list of Ly-α candidates does not depend on the choice of K_{line}.
CADIS measurements and images of the probable Ly-α galaxies are shown in Fig. 3.2 and 3.3, and of the probable [O II] λ3727 galaxies in Fig. 3.4 and 3.5.

Figure 3.2 Lyman-α galaxy candidates with the line detected in FP-A. From left to right, panel (1)-(5): (1) Photometry in all 14 optical CADIS filters fitted by a continuum-model; (2) The Fabry-Perot measurements in window A with a Ly-α profile fitted to the observed flux data; (3) Pre-filter image; (4) Fabry-Perot Image; (5) R-image. The size of the images (3)-(5) is $30'' \times 30''$, respectively.

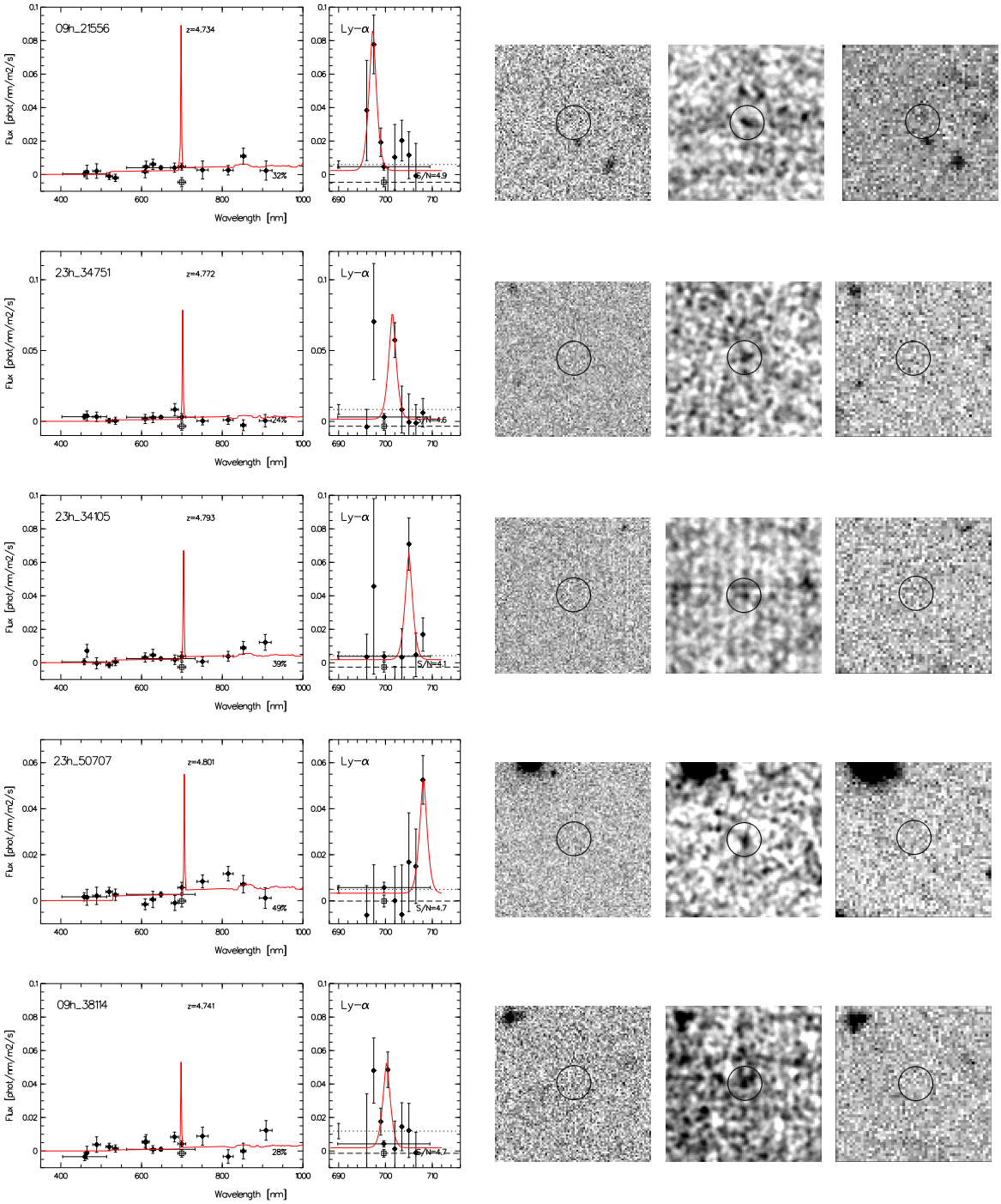

Figure 3.3 Lyman-α galaxy candidates with the line detected in FP-B. From left to right, panel (1)-(5): (1) Photometry in all 14 optical CADIS filters fitted by a continuum-model; (2) The Fabry-Perot measurements in window B with a Ly-α profile fitted to the observed flux data; (3) Pre-filter image; (4) Fabry-Perot Image (in case of 01h-field objects FP image from MOSCA) ; (5) R-image, or, in case of 01h-field galaxies, a second FP image taken with CAFOS. The size of the images (3)-(5) is 30″ ×30″, respectively.

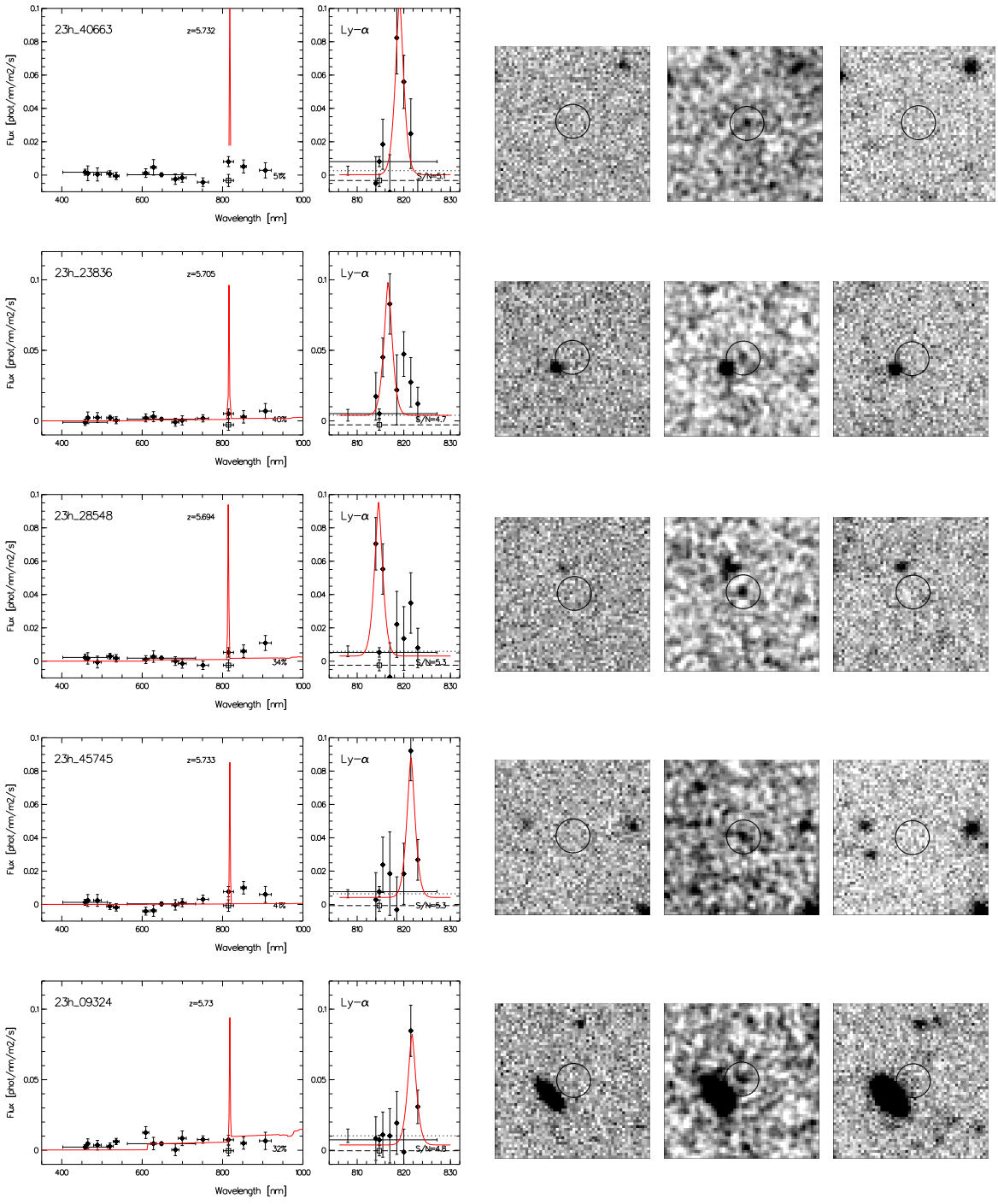

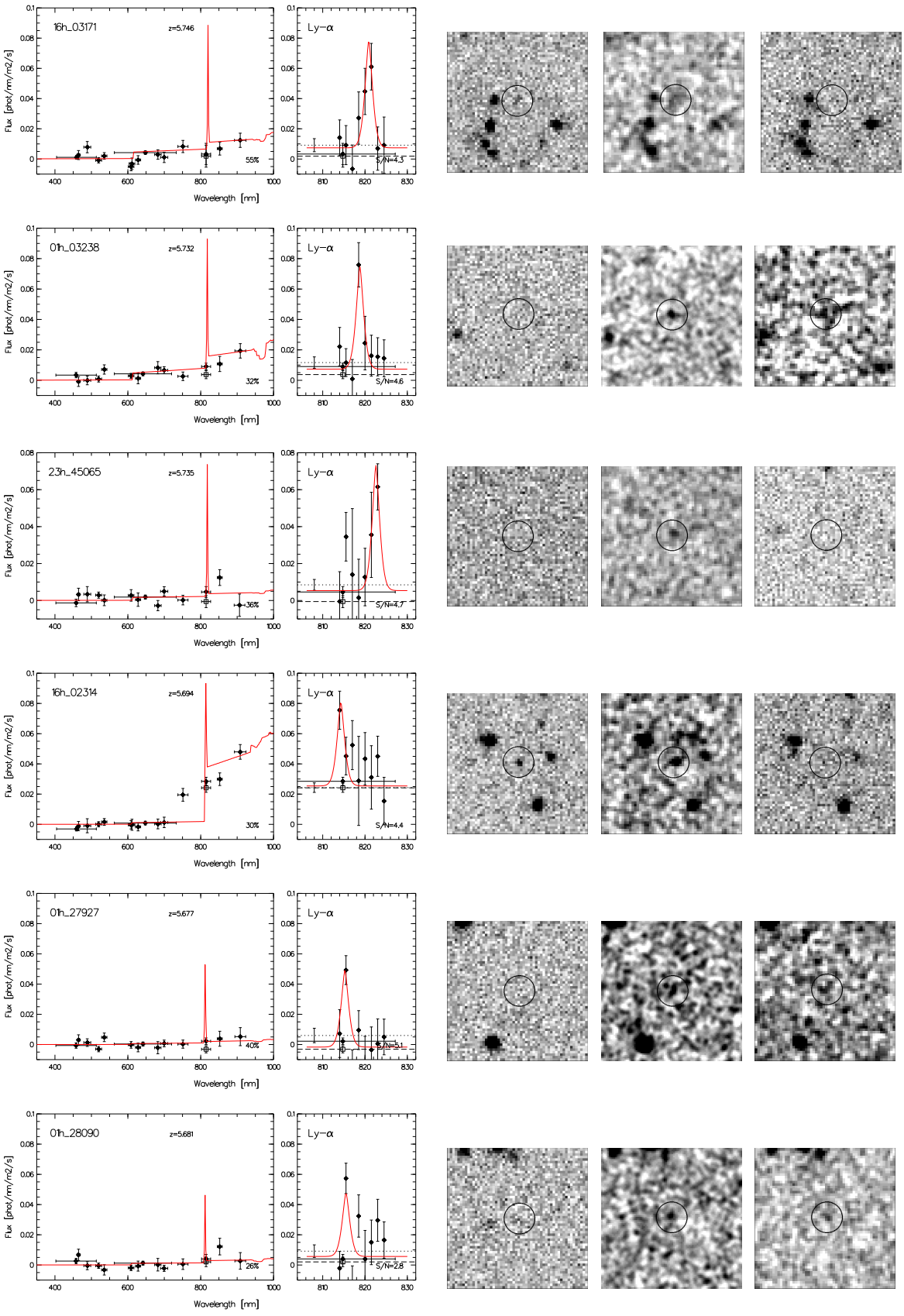
16h_03171
z=5.746
Ly−α
S/N=4.3
55%
01h_03238
z=5.732
Ly−α
S/N=4.6
32%
23h_45065
z=5.735
Ly−α
S/N=4.7
36%
16h_02314
z=5.694
Ly−α
S/N=4.4
30%
01h_27927
z=5.677
Ly−α
S/N=5.1
40%
01h_28090
z=5.681
Ly−α
S/N=2.8
26%
Flux [phot./nm/m2/s]
Wavelength [nm]

Figure 3.4 Probable [O II] λ3727 galaxies without blue continuum with the line detected in FP-A. From left to right, panel (1)-(5): (1) Photometry in all 14 optical CADIS filters fitted by a continuum-model; (2) The Fabry-Perot measurements in window A with a Ly-α profile fitted to the observed flux data; (3) Pre-filter image; (4) Fabry-Perot Image; (5) R-image. The size of the images (3)-(5) is $30'' \times 30''$, respectively.

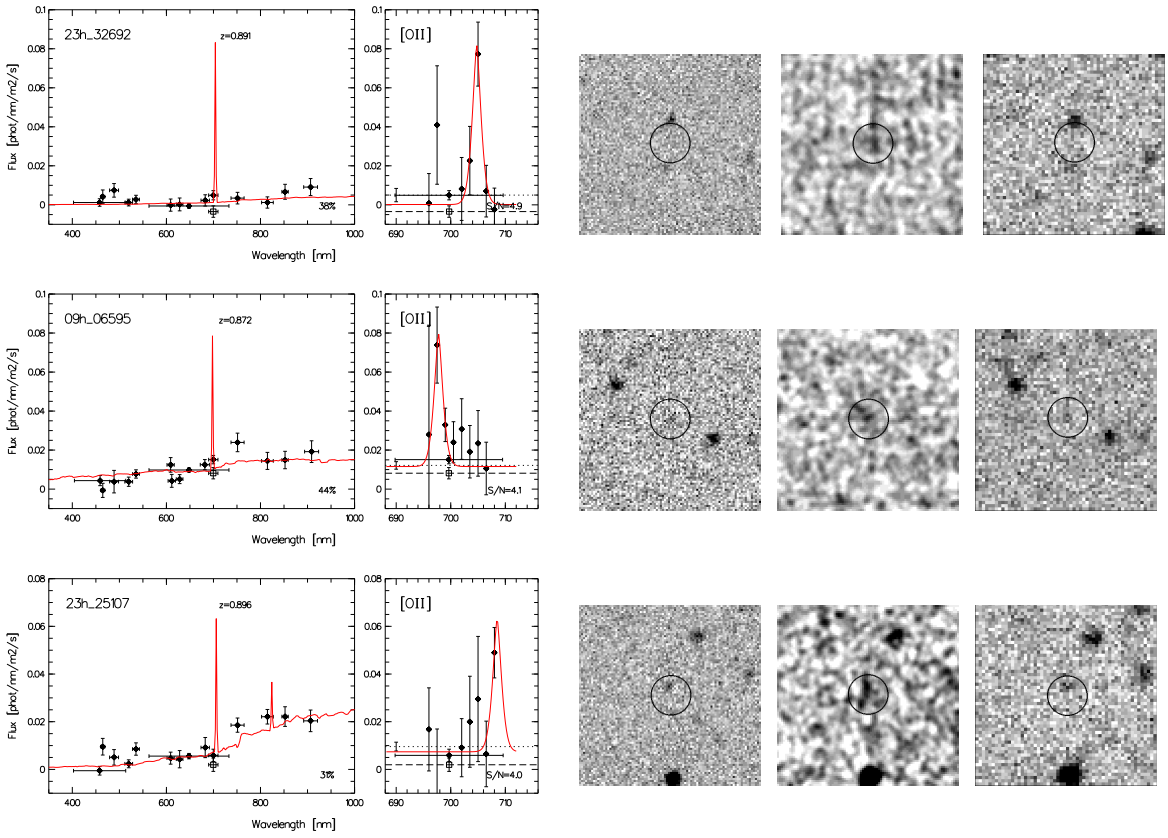

Figure 3.5 Probable [O II] $\lambda 3727$ galaxies without blue continuum with the line detected in FP-B. From left to right, panel (1)-(5): (1) Photometry in all 14 optical CADIS filters fitted by a continuum-model; (2) The Fabry-Perot measurements in window B with a Ly-α profile fitted to the observed flux data; (3) Pre-filter image; (4) Fabry-Perot Image (in case of 01h-field objects FP image from MOSCA) ; (5) R-image, or, in case of 01h-field galaxies, a second FP image taken with CAFOS. The size of the images (3)-(5) is $30'' \times 30''$, respectively.

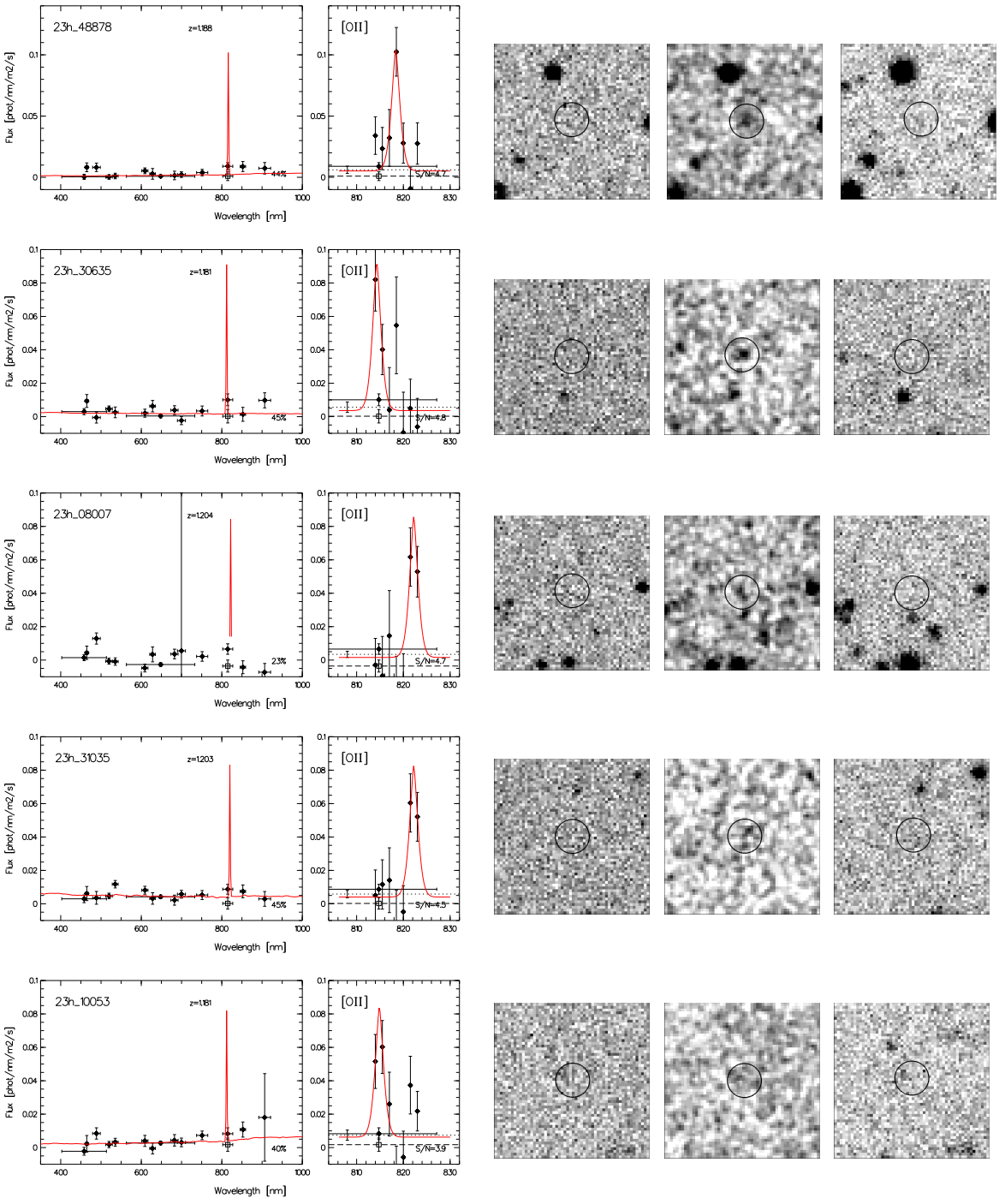

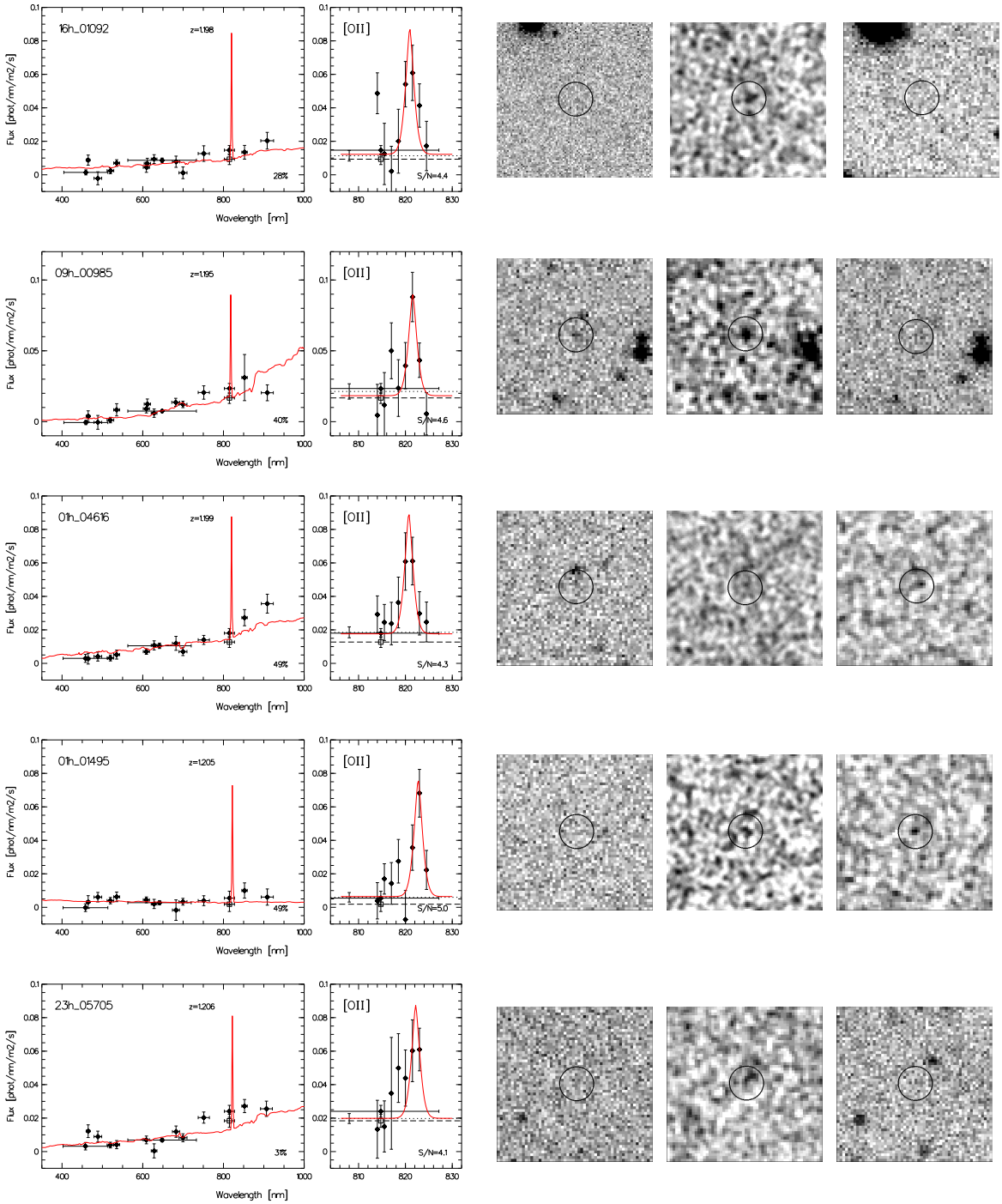
16h_01092
z=1.198
[OII]
28%
S/N=4.4
09h_00985
z=1.195
[OII]
40%
S/N=4.6
01h_04616
z=1.199
[OII]
49%
S/N=4.3
01h_01495
z=1.205
[OII]
49%
S/N=5.0
23h_05705
z=1.206
[OII]
31%
S/N=4.1
Flux [phot/nm/m2/s]
Wavelength [nm]

3.8. Follow-Up Spectroscopy of Ly-α Candidates

Due to the low abundance of Ly-α galaxies (see below, Fig. 3.10), spectroscopic follow-up at large telescopes constitutes an important part of the survey: First, one has to search close to the detection limit, which makes statistical contamination more common, and second, even very rare and unlikely contaminants, like distant supernovae or other transient objects, reach surface densities comparable to that of the Ly-α candidates.
The first goal of the spectroscopic follow-up of probable Ly-α galaxies is therefore to verify the emission line. The line shape and the continuum blue- and red-wards of the emission line might also allow us to decide between Ly-α and [O II] λ 3727. If the line has been verified, but the resolution is not good enough to identify the emission line, a second step is the clear confirmation of the line using higher resolution grisms, in order to see if the line shows the asymetric profile expected for Ly-α. If galaxies with bright Ly-α line at $z > 4.7$ can be confirmed, then the third step is a detailed study of the corresponding galaxy. The investigation of primeval galaxies can give important insights in the galaxy formation.
Because of the restricted access to 8-m telescopes (particularly on the northern hemisphere), only few spectroscopic observations of some CADIS Ly-α candidates have been done by now. Nevertheless, the verification or non-verification of a line for every single Ly-α candidate is very important in order to set more robust upper limits to the number counts of galaxies at high redshift, which can set stringent constraints on theoretical models of galaxy formation.
Spectroscopic follow-up observations of Ly-α candidates in the 01h- and 23h-field were obtained in the summer and autumn of 2001, using FORS 2 at the VLT (see section 2.3.1 for details of the observations). Fig. 3.6 shows the distribution of Ly-α candidates, and [O II] λ 3727 (possible Ly-α) candidates for the four analysed fields.

3.8.1. Non Verification of Ly-α Candidates

From seven observed Ly-α/[O II] λ 3727 candidates (objects which passed the criteria (1)-(3)) we have verified the line for two Ly-α candidates and one probable [O II] λ 3727 (possible Ly-α) candidate. There are several reasons for the non-detections of the other four galaxies.
First, the VLT service mode observations of 23h-field from July 2001 were carried out much too close to the moon, in violation of our specifications. Thus, particularly the background in FP-window A around 700 nm is severly enhanced above "dark night-sky", and shows a significant deterioration of the S/N ratio. Therefore, the signal to noise was too bad in order to detect the emission line seen in FP-A of the Ly-α candidates 23h-34105 and 23h-34751.
Second, offsets between continuum and line emission (see section 1.10 for details) could have caused the $1''$ wide slit to miss the line emitting region of the galaxies. We have not confirmed any line or continuum for the Lyman-α candidates 01h-27927 and 01h-28090, possibly for this reason.
The mask insertion procedure could have produced another offset of up to $0''.3$; this offset has been detected by comparing flatfield and science images, which were taken at different times, i.e., with different mask insertions. This can be another source of signal to noise deterioration, which can lead to the non-detection of faint emission lines.

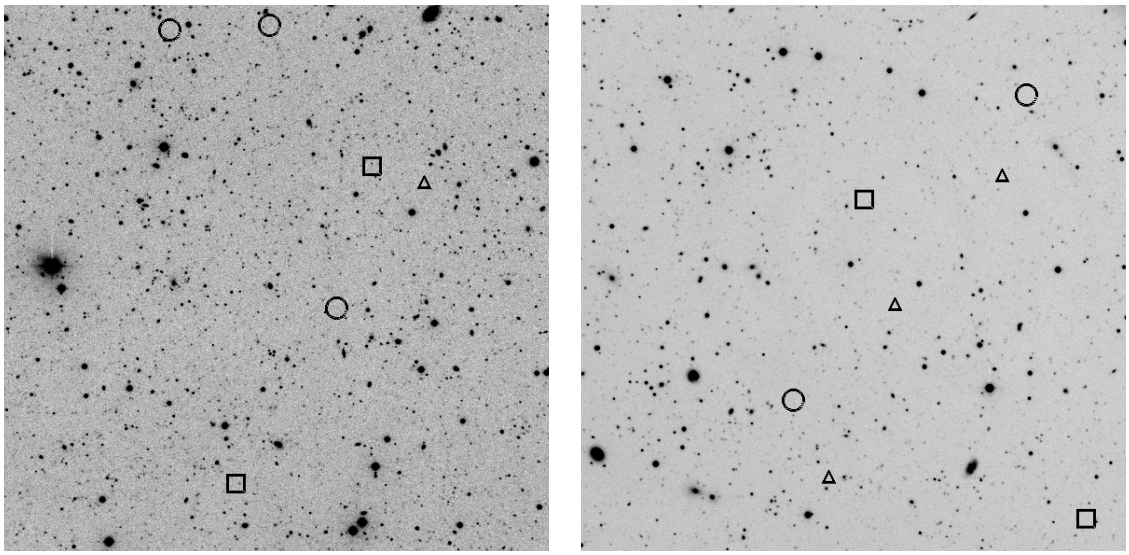

01h field

09h field

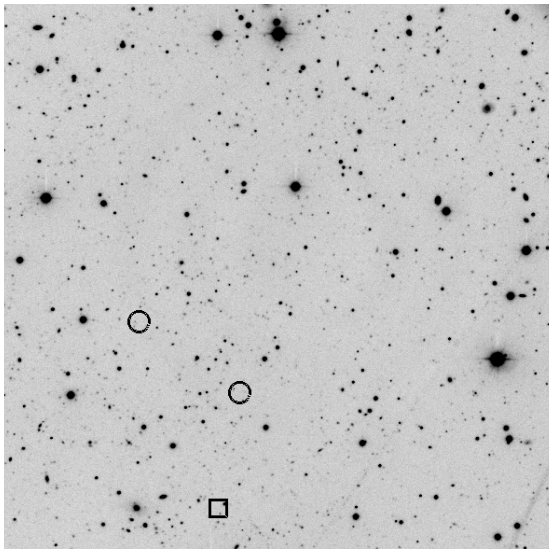

16h field

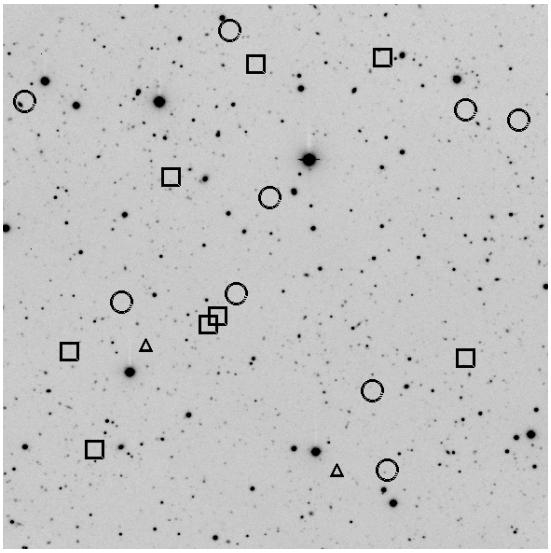

23h field

Figure 3.6 The position in the CADIS fields of objects with no detected B-flux. Circles denote the prime Ly-α candidates, squares probable [O II] λ3727, possible Ly-α galaxies, and triangles galaxies with no B-flux which show a veto signal (probable foreground galaxies). The showed images are 10 $\times$ 10 arcmin^2.

Last but not least, the line of some Ly-α/[O II] λ3727 candidates can be indeed spurious, since we expect a residual contamination of about 50% in our list of Ly-α candidates, as discussed in section 3.7.

3.8.2. Verification of Ly-α Candidates

For two Lyman-α candidates we verified the emission line seen in FP scan: the galaxy 01h-3238 shows an emission line at 819.0 ± 0.3 nm, and the object 23h-50707 shows an emission line at 705.7 ± 0.3 nm (see Fig. 3.7 and 3.8). No continuum and no additional emission lines are seen on the VLT spectra. According to the CADIS measurements, these two objects satisfy the properties (iii) and (iv) of a primeval galaxy, since almost no flux is seen on the blue side of the emission line. Therefore, we conclude that the two emission lines are very probable Ly-α lines of two high redshift galaxies, 01h-3238 at $z = 5.735 \pm 0.003$, and 23h-50707 at $z = 4.803 \pm 0.003$, respectively.
The galaxy 01h-4616, which shows no flux in the B filter and in the veto filters, passed the criteria (1)-(3) for selection of Ly-α candidates, but was classified as a probable [O II] $\lambda 3727$ galaxy at $z \approx 1.2$ according to criterion (4). With the VLT we could verify an emission line at 820.9 ± 0.3 nm for this galaxy. No other lines are seen on the VLT spectrum and a continuum on both sides of the line is detected (Fig. 3.9). Therefore, the emission line is likely to be [O II] $\lambda 3727$ at $z = 1.202 \pm 0.001$.

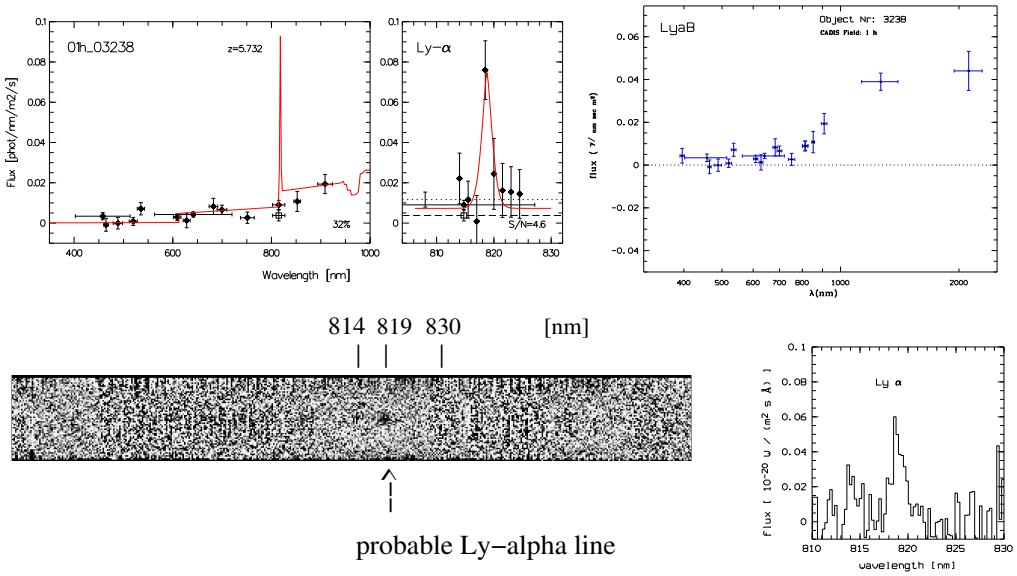

Figure 3.7 CADIS photometry (top) and VLT spectrum (bottom) of CADIS 01h-3238, a probable Ly-α galaxy at $z = 5.735$.

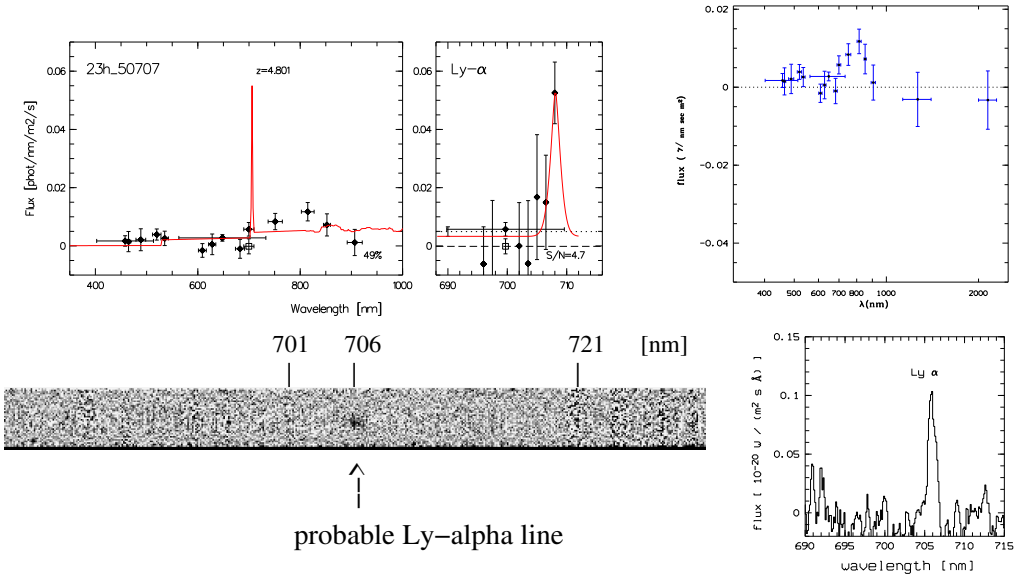

Figure 3.8 CADIS photometry (top) and VLT spectrum (bottom) of CADIS 23h-50707, a probable Ly-α galaxy at $z = 4.803$.

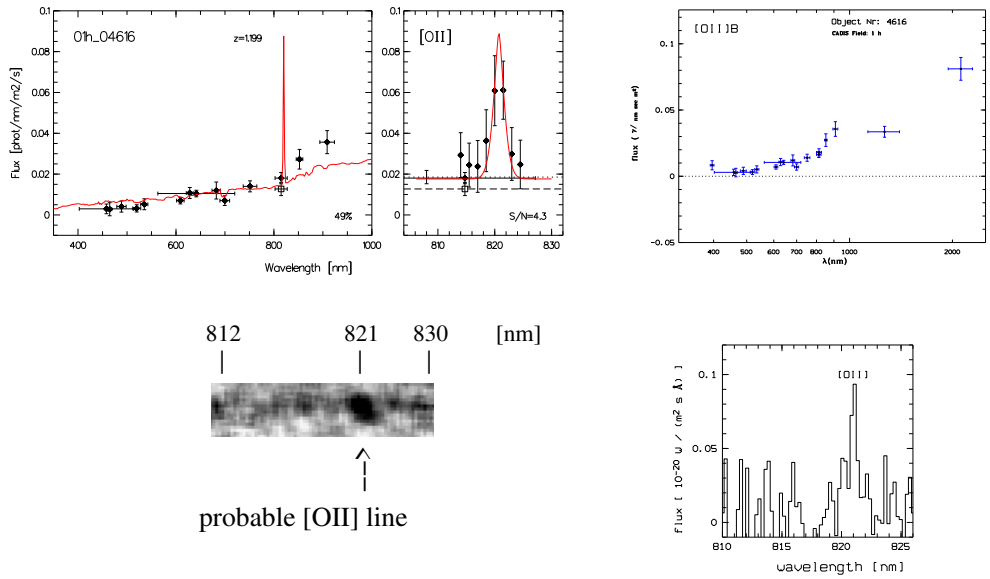

Figure 3.9 CADIS photometry (top) and VLT spectrum (bottom) of CADIS 01h-4616, a galaxy at $z = 1.202$ with a detected [O II] $\lambda 3727$ line in FP-B.

3.8.3. Properties of Verified Ly-α Candidates

The slit width during the VLT observations was possibly too narrow and we may have thus measured only a fraction of the line flux as indicated, e.g., by objects in Fig. 1.5, right panel, which have a spectroscopic flux smaller than the CADIS flux. Therefore, we calculate the absolute Ly-α luminosity of 01h-3238 and 23h-50707 from the observed fluxes measured in the FP scan. The Lyα flux is $f(\mathrm{Ly}\alpha) = (4.1 \pm 0.8) \times 10^{-20}$ W m^{-2} for 01h-3238, and $f(\mathrm{Ly}\alpha) = (4.0 \pm 0.8) \times 10^{-20}$ W m^{-2} for 23h-50707, based on these data. Using a $\Omega_0 = 0.3$, $\Omega_\Lambda = 0.7$, and $\mathrm{H}_0 = 70\,\mathrm{km\ s^{-1}\ Mpc^{-1}}$ cosmology, we obtain an absolute Lyα luminosity of $L(\mathrm{Ly}\alpha) \simeq (14.5 \pm 3.0) \times 10^{35}$ W for 01h-3238, and $L(\mathrm{Ly}\alpha) \simeq (9.5 \pm 1.9) \times 10^{35}$ W for 23h-50707. These Lyα luminosities are higher compared to those of other $z > 5$ galaxies (luminosities are estimated by using the same cosmology): e.g., 3.3×10^{35} W for HCM 6A at $z = 6.56$ (Hu et al. 2002); 6.1×10^{35} W for SSA22-HCM1 at $z = 5.74$ (Hu et al. 1999); 3.4×10^{35} W for HDF 4-473.0 at $z = 5.60$ (Weymann et al. 1998). The derived SFR for the two Ly-α galaxies (using equation B.3) is $(14.5 \pm 3.0) M_\odot \mathrm{yr}^{-1}$ for 01h-3238, and $(9.5 \pm 1.9) M_\odot \mathrm{yr}^{-1}$ for 23h-50707.
It should be noted that, if the two galaxies with verified emission lines, 23h-50707 and 01h-3238, are indeed at high redshift, they are the brightest Ly-α galaxies with the highest SFRs known at $z > 4.7$ (apart from the radio galaxies, where the emission very probable is not driven by stars, but by active nuclei).

3.9. The Abundance of Ly-α Emitting Primeval Galaxies

3.9.1. Model Predictions

Thommes & Meisenheimer (2002) estimate the expected abundances of Ly-α galaxies at high redshift, extrapolating the local luminosity function of galaxies and their stellar content back into the past. They assume that elliptical galaxies and the bulges of spiral galaxies, both called spheroids, have been formed early in the universe, while the disks formed as intergalactic gas accretes on the preexisting bulges. In the model, the PGs are these spheroids during their first burst of star formation.
Thommes & Meisenheimer calculate the surface number density of Ly-α-emitting PGs (primeval galaxies) on the sky per solid angle $\Delta\Omega$ which have detectable Ly-α fluxes greater than a certain flux limit F_{lim} and which have redshifts z_0 in an interval $[z_0 - \Delta z/2, z_0 + \Delta z/2]$. z_0 is given by the central wavelength of the narrow band filter, Δz by the band width of the filter $\Delta\lambda$ ($\Delta z = \Delta\lambda/\lambda_{Ly\alpha}$; $\lambda_{Ly\alpha} = 121.6\,\mathrm{nm}$), and $\Delta\Omega$ by the area covered by the survey. $\Delta\Omega, \Delta z$ and z_0 define a certain comoving volume ΔV of the universe.
The number N of PGs in the volume ΔV with $L_{Ly\alpha} \geq L_{min}(z_0)$ at the epoch $t_0 = t(z_0)$ was calculated, where $L_{min}(z_0)$ is the intrinsic Ly-α flux of PGs at z_0 which produce observable fluxes of F_{lim}:

$$L_{min}(z_0) = 4\pi F_{lim} D_L(z_0)^2, \tag{3.1}$$

with the luminosity distance $D_L(z_0)$.
N depends on the evolution of the Ly-α luminosity as a function of time and mass of the galaxy, the galaxy formation history and the total number density of halos as a function of their mass (mass function). It is assumed that:

- the Ly-α emitting PGs are the precursors of the present day spheroids (bulges and ellipticals) in the phase of their first star burst, and that they form at the peaks of the underlying density field;

- the first star formation starts in a dust-free environment, but the IGM is enriched with dust in the first couple of hundred million years, leading to attenuation of the Ly-α emission. The time evolution of the Lyα emission is described by a Gaussian with FWHM $\Delta t_{Ly\alpha}$, which gives the typical duration of the Lyα bright phase;

- the SFR (and therefore the Ly-α emission) is proportional to the baryonic mass M_b of the PG;

- the PGs form from peaks of the underlying density field with a distribution of 'ignition times' $P_M(t_s)$. The parameters t_* and M_* (the characteristic mass scale, which just collapses at the time t_*) are fixed so that $P_M(t_s)$ peaks at a certain redshift z_{max} for $M_* = 4 \times 10^{10} \mathrm{M}_\odot$, which corresponds roughly to the (baryonic) bulge mass of a Milky Way-like galaxy today. z_{max} is a free parameter of the models. For $M < M_*$ the PGs have their first star formation at higher redshift, for $M > M_*$ at lower redshift than z_{max}, in agreement to a 'bottom up' hierarchical stucture formation;

- an approximation of the mass function of PGs can be deduced from the current (baryonic) mass function of spheroids.

For more details about the model predictions see Thommes & Meisenheimer (2002).

3.9.2. Recent Published Systematic Searches for Galaxies at High Redshift

In order to compare the theoretical predictions with observations, we want to include not only the CADIS results, but also results from other systematic searches for galaxies at high redshift. In the last few years, the advance of large telescopes has allowed the discovery of galaxies up to $z \approx 6$. This section gives an overview of published systematic searches for galaxies at $z > 3$.

3.9.2.1. Galaxies at $z \sim 3.5$

$z \approx 3.5$ is the highest redshift at which a substantial number of Ly-α emitting galaxies has been found. The luminosity function at $z \approx 3.5$ can be used as a reference for comparison with higher redshifts; e.g., the parameters of the models of Thommes & Meisenheimer (2002) were fixed with the observed surface density of Lyα emitters at $z \approx 3.5$.
Using the 10m Keck II telescope, Cowie & Hu (1998) performed a narrowband and spectroscopic search for strong Ly-α emitting star forming galaxies in the redshift range 3–6 (see also Hu et al. 1998). They reached faint flux levels of $\approx 1.5 \times 10^{-20}$ W m^{-2} (5σ). Their main selection criterion to discriminate high redshift Ly-α candidates from foreground emission line objects was an extremely high equivalent width of the emission line ($W_\lambda > 10\,\mathrm{nm}$) together with additional broad-band colour criteria. In order to find galaxies in the redshift range $z = 3.405 - 3.470$, in and around the Hubble Deep Field and the Hawaii Deep Field SSA 22 (total area of 46 arcmin^2), they performed deep narrow band images with a 539/7.7 nm filter, and selected 12 objects. Multi-object spectroscopy

of these 12 galaxies with LRIS on Keck II confirmed the strong emission lines to be Ly-α at $z \approx 3.4$. Two galaxies have also strong C IV emission, suggesting AGN activity.
Kudritzki et al. (2000) found high-redshift $z \sim 3.1$ Ly-α emitters with Ly-α fluxes between 2×10^{-20} and $2 \times 10^{-19}\mathrm{Wm}^{-2}$, during a narrowband imaging survey aimed at detecting the faint emission from the [O III] $\lambda\,5007$ line of intracluster planetary nebulae in Virgo. They were looking in a small redshift range of about $\Delta z = 0.04$, and their survey area was 50 arcmin^2.
In order to calculate the cumulative number counts of Lyman-α-galaxies at $z \approx 3.5$, $N\,\mathrm{deg}^{-2}$ per $\Delta z = 0.1$, we used Tab. 1 from Cowie & Hu (1998), and Tab. 1 from Kudritzki et al. (2000). Because the galaxies observed by Kudritzki et al. have a redshift $z \approx 3.1$, we transformed their observed fluxes, taking into account the different luminosity distance, to the flux which would have been observed if these galaxies were at $z \approx 3.5$.

3.9.2.2. Galaxies at $z \sim 4.8$

Two galaxies with verified Ly-α line and several candidates have been found in systematic searches close to $z = 4.8$, the redshift at which we search Ly-α galaxies with a line detected in CADIS FP-A.
Using narrowband observations of a 24 arcmin^2 field, through a narrowband interference filter centered at 674.1 nm with a bandpass of 7.8 nm, Hu et al. (1998) detected two Ly-α galaxies at $z = 4.52$.
Malhotra & Rhoads (2002) found 157 Ly-α *candidates* at $4.37 < z < 4.57$ in one field of 0.36 deg^2, with a detection limit of $\sim 2 \times 10^{-20}\mathrm{Wm}^{-2}$. This corresponds to a source density at $z \approx 4.8$ of (at most) 2180 deg^{-2} per unit z.
Ouchi et al. (2002) found 87 Ly-α *candidates* at $z = 4.86 \pm 0.03$ in an 0.15 deg^2 field. They expect, however, $\sim 40\%$ contamination by foreground objects. This corresponds (taking into account the contamination) to a source density at $z \approx 4.8$ of about 6000 deg^{-2} per unit z, about 3 $\times$ the number found by Malhotra & Rhoads (2002). The discrepancy could be due to additional contamination by artefacts and foreground galaxies, since we expect from the CADIS experience an even higher contamination of the Ouchi et al. sample. Therefore, we have not included the Ouchi et al. (2002) results in our comparison between observed and theoretical abundances (section 3.9.3).

3.9.2.3. Galaxies at $z \sim 5.7$

Only one (verified) galaxy and a number of candidates have been found in systematic searches near the redshift $z \approx 5.7$. This is the redshift at which we search Ly-α galaxies with a line detected in CADIS FP-B.
Hu et al. (1999) detected and verified one Ly-α galaxy at $z = 5.74$ using narrowband observations of a 30 arcmin^2 field, through a narrowband interference filter centered at 818.5 nm, with a bandpass of 10.5 nm.
Rhoads & Malhotra (2001) reported 13 Ly-α *candidates* at $z \approx 5.7$. They used two narrow-band filters with central wavelengths at 815 and 823 nm, which are each 7.5 nm wide and can pick up Ly-α emission from $z = 5.70 - 5.78$. Because the filter bandpass deteriorated below these specifications outside a central circle of $\sim 30'$ diameter, the outer part of the images was excluded from the analysis, such that the remaining area was $\sim 0.2\,\mathrm{deg}^2$. Their 5σ flux thresholds of $\sim 0.4\mu$Jy correspond to $\mathrm{F}_{\mathrm{lim}} \sim 1.7 \times 10^{-20}\mathrm{Wm}^{-2}$.

3.9.3. Comparison Between the Observed and Theoretical Abundance of Ly-α PGs

The number counts of Ly-α galaxies from CADIS and other systematic searches can be compared with model predictions from Thommes & Meisenheimer (2002). Fig. 3.10 shows the cumulative number counts of Lyman-α-galaxies from observations and theory, presented as the total number of galaxies N deg^{-2} per $\Delta z = 0.1$ which are brighter than a certain observed flux F_{lim}.

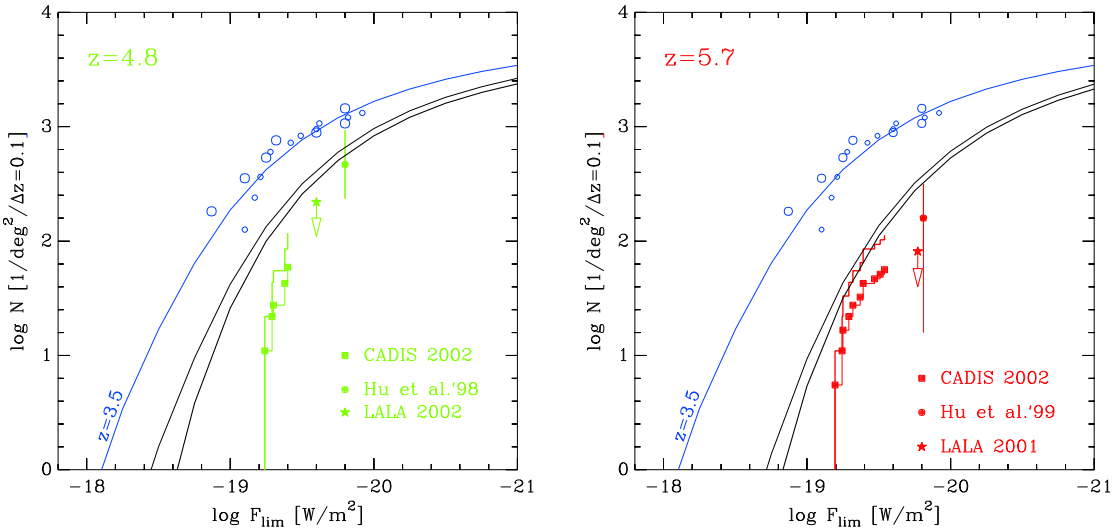

Figure 3.10 Cumulative number counts of Lyman-α-galaxies, N deg^{-2} per $\Delta z = 0.1$, which are brighter than a certain observed flux F_{lim}, at $z = 4.8$ (left panel) and $z = 5.7$ (right panel). In the cumulative histogram the upper edge represents the number of candidates, while the squares take into account the likely residual contamination by noise. Additional values of the number density are from Hu et al. (1998) for $z = 4.5$, and from Hu et al. (1999) at $z = 5.7$. The arrows show upper limits of the number density from the candidate lists of galaxies found by the Large Area Lyman Alpha Survey (LALA) at $z = 4.6$ (Malhotra & Rhoads 2002), and at $z = 5.7$ (Rhoads & Malhotra 2001). For comparison, we show the measured abundance of Lyman-α-galaxies at $z = 3.5$ through emission-line-surveys from Hu et al. (1998, small circles), and Kudritzki et al. (2000, large circles). A model luminosity function from Thommes & Meisenheimer (2002), adapted to the values at $z = 3.5$, has been converted to the redshifts searched by CADIS assuming *no* evolution between $z = 5.7$ und $z = 3.5$.

A model luminosity function has been adapted to the cumulative number counts of Lyman-α-galaxies at $z = 3.5$, which seem to be rather well determined through emission-line-surveys from Hu et al. (1998, small circles) and Kudritzki et al. (2000, large circles). Assuming *no* evolution between $z = 5.7$ – or $z = 4.8$, respectively – and $z = 3.5$, this model luminosity function has been converted, taking into account the higher luminosity distance and different comoving volume, to the redshifts searched by CADIS. The thin black line shows the model including all galaxies, the thick line shows the model without the predecessors of elliptical galaxies. In the cumulative histogram of CADIS Ly-α galaxy candidates, the upper edge represents the number of CADIS candidates deg^{-2} and per $\Delta z = 0.1$, brighter than the respective F_{lim}, while the squares take into account the likely residual contamination by noise. One can see that CADIS actually probes the very bright end of the luminosity function. While the number counts of Hu et al. at both $z = 4.8$ (2 galaxies found by Hu et al. 1998) and 5.7 (1 galaxy found by Hu et al. 1999) seem

still compatible with a no-evolution model extrapolating the abundance, even the total number of candidates found by the LALA survey and CADIS falls short of the model. A model of Thommes & Meisenheimer (2002) which is in agreement with the CADIS and LALA measurements at $z = 5.7$ (see Fig. 3.11) gives a typical duration of the Ly-α bright phase, $\Delta t_{Ly\alpha}$, of 471 Myrs, and $z_{max} = 4.4$.

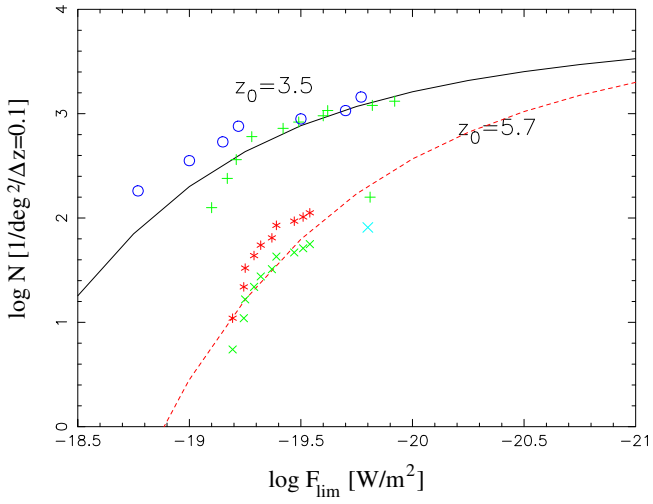

Figure 3.11 Cumulative number counts of Ly-α galaxies compared with the model of Thommes & Meisenheimer (2002). Blue circles are the number counts of galaxies at $z = 3.5$ from Hu et al. (1998), green crosses from Kudritzki et al. (2000). The blue X is the point from LALA survey (Rhoads & Malhotra 2001), the green cross close to it is the point from Hu et al. (1999). Red stars are upper limits for the CADIS Ly-α galaxy number counts, while the green Xs take into account the likely residual contamination. The model luminosity function adapted to the cumulative number counts of Ly-α galaxies at $z = 3.5$ is showed by the solid black line; the dotted red line shows the evolution of the luminosity function to $z = 5.7$ for a model of Thommes & Meisenheimer (2002) with the parameters given in the text.

3.10. Conclusions and Discussion

In summary, we have found 16 robust bright Ly-α candidates at $z > 4.7$: 5 Ly-α candidates at $z \approx 4.8$ and 11 Ly-α candidates at $z \approx 5.7$. Moreover, 13 probable [O II] λ3727 candidates can possibly be also Ly-α galaxies at $z > 4.7$, so we have a total of 29 galaxy candidates at $z > 4.7$ in the four CADIS fields analysed by now. The line of three candidates has been confirmed with VLT, but the line shape is not clearly seen because of the low signal to noise, so the distinction between [O II] λ3727 and Ly-α has to be ensured by higher resolution spectroscopy.

Nevertheless, decisive first conclusions can be drawn from the CADIS search for Ly-α galaxies at $z > 4.7$. From comparison of model predictions, our results, and published data on fainter Ly-α galaxies at $z > 4.7$, we conclude that Lyman-α-galaxies at $z = 4.8$ and 5.7 are at most as abundant as at $z = 3.5$, and the abundance probably decreases at $z > 4$. Since our results at $z \approx 4.8$ rely on the FP-A window in 09h-field, and only half of the FP-A window in the 23h-field, whereas the Ly-α candidates at $z \approx 5.7$ come

from four reduced fields in window B, at least the conclusion that the number count of Lyman-α-galaxies at $z \approx 5.7$ decreases is robust.
Large-scale structure can influence galaxy counts even at high redshifts (Steidel et al. 1998). Nevertheless, for obtaining the number counts of Ly-α galaxies at $z \approx 5.7$, large scale structure should average out when combining four CADIS fields ($\approx 14\times$ the size of the field searched by Hu et al. 1999). Small fields like those searched by Hu et al. (1998, 1999) in order to find galaxies at $z \approx 4.5$ and $z \approx 5.7$ (see Fig. 3.10) could, however, be biased because of large scale structure.
Two things should be noted about the comparison of the luminosity function at $z \approx 3.5$ with that at higher redshifts. First, the most luminous Ly-α *observed* line fluxes for galaxies at $z \approx 3.5$ found by Hu et al. (1998) and Kudritzki et al. (2000) are of order of $10^{-19}\mathrm{Wm}^{-2}$. Taking into account the higher luminosity distance at $z = 4.8$ and $z = 5.7$ (compared to $z = 3.5$) these galaxies have apparent line fluxes of $\sim 5 \times 10^{-20}\mathrm{Wm}^{-2}$ at $z = 4.8$, and $\sim 3 \times 10^{-20}\mathrm{Wm}^{-2}$ at $z = 5.7$ (using a $\Omega_0 = 0.3$, $\Omega_\Lambda = 0.7$ and $\mathrm{H}_0 = 70\,\mathrm{km\ s}^{-1}\ \mathrm{Mpc}^{-1}$ cosmology); i.e., galaxies with intrinsic bright Ly-α emission, corresponding to observed line fluxes $> 3 \times 10^{-20}\mathrm{Wm}^{-2}$ at $z \approx 5.7$ – as searched by CADIS – have not been found at $z \approx 3.5$. Thus, very little is actually known about the shape of the high luminosity end of the luminosity function at high redshift.
Second, the number counts at the bright end of the luminosity function at $z = 3.5$, resulting from two brighter galaxies detected by Kudritzki et al. (2000, large circles), are higher than the results of Hu et al. (1998, small circles). Since large-scale structure can influence galaxy counts even at high redshifts (Steidel et al. 1998), the Kudritzki et al. number counts could be biased, because Kudritzki et al. searched only one field – whereas Hu et al. survey goes over two fields. Not taking into account these two points from Kudritzki et al. would result in a steeper luminosity function at the bright end at $z = 3.5$. This would decrease the discrepancy between the no-evolution model luminosity function at $z \approx 4.8$ and $z \approx 5.7$ and the CADIS upper limits for the number counts of Ly-α galaxies.
Nevertheless, the assumption that the luminosity function does not evolve between $z \approx 3.5$ and $z \approx 5.7$ (or $z = 4.8$, respectively) seems not to be supported, since the total numbers of candidates found in the CADIS and LALA survey fall short of the model luminosity function assuming *no* evolution between $z = 5.7$ ($z = 4.8$) and $z = 3.5$.
Lyα galaxies offer a particularly direct and solid test of the reionization epoch (Haiman & Spaans 1999). Because Ly-α photons are resonantly scattered in the neutral universe before reionization, the Ly-α-line is strongly spread in both angle and frequency. This produce a peak line intensity too weak for practical detection with present instruments and telescopes. Therefore, the reionization redshift should be marked by a sharp decrease in the number counts of Ly-α emitters. The CADIS results allows the conclusion that the Lyman-α bright phase of primeval galaxies had its peak after $z = 6$. This is consistent with SDSS results, that $z \sim 6$ marks the end of the reionization epoch (Fan et al. 2002).

3.11. Outlook

More CADIS data will be obtained and reduced in the near future. With the inclusion of data from window C in several fields, we will be also able to search for Ly-α galaxy candidates at $z \approx 6.5$, even though only one such galaxy is expected in the six CADIS fields according to the Thommes & Meisenheimer (2002) models. Candidates for Ly-α

galaxies in the 09h- and 16h-fields, which are not visible from the VLT, must be observed with large telescopes in the northern hemisphere (Keck, Gemini, Subaru). Moreover, high-resolution spectroscopy of CADIS Ly-α galaxies with verified lines should enable detailed studies of these objects (e.g. kinematic studies).

Appendix A
CADIS, VLT, and TNG Spectra

Spectra 01H-Field

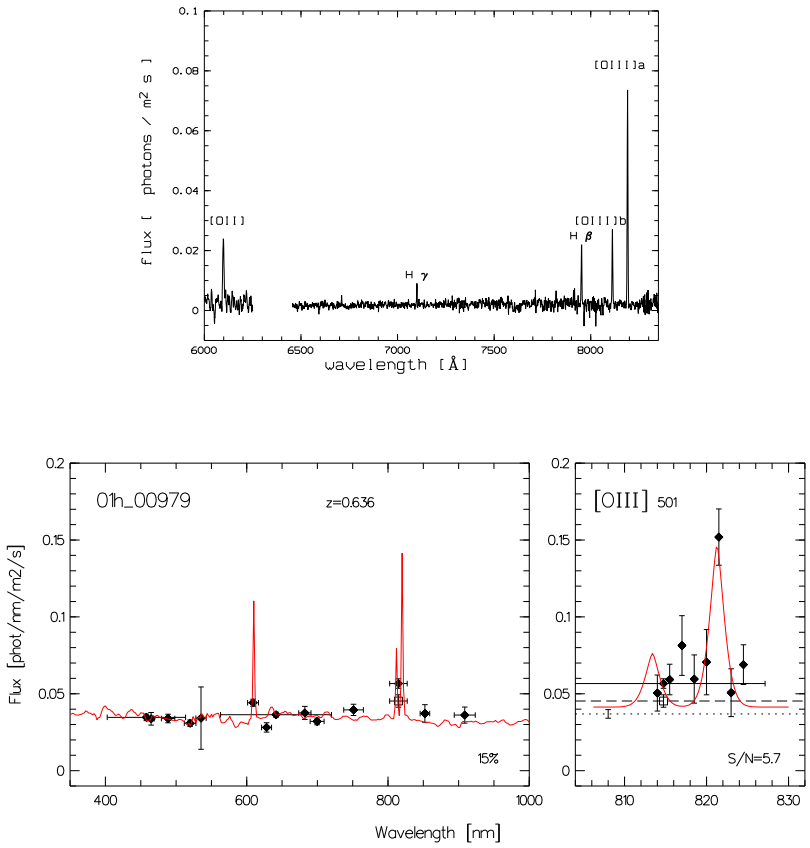

Figure A.1 The galaxy 01h-979 at $z = 0.636$. **Upper panel**: VLT spectra of this galaxy using FORS2 with the 600RI and 600R grisms. **Lower panel**: Photometry in all 14 optical CADIS filters fitted by a continuum-model (left) and the Fabry-Perot measurements in window B with a [O III] doublet profile fitted to the observed flux data (right).

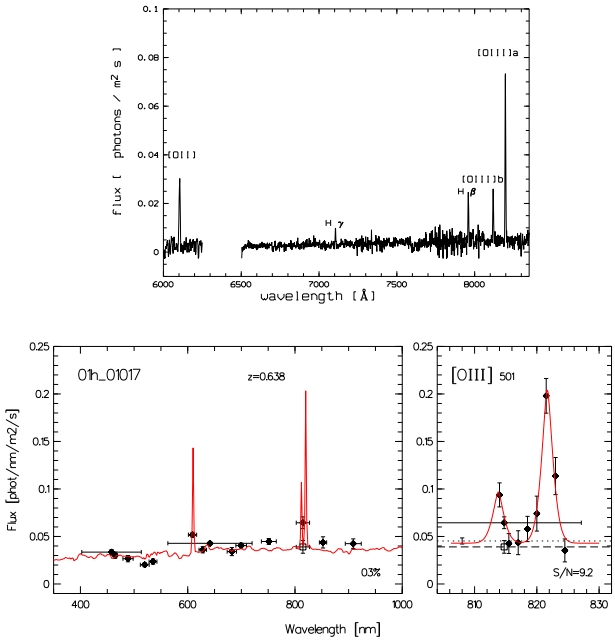

Figure A.2 Same as Fig. A.1 for the galaxy 01h-1017 at $z = 0.638$.

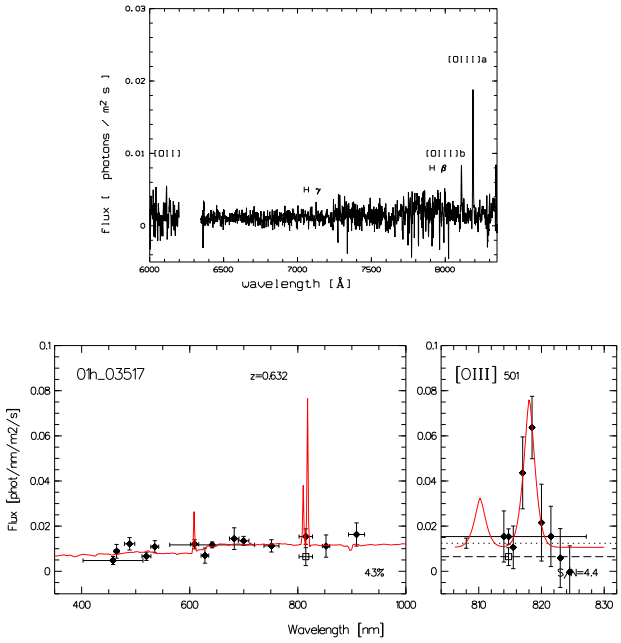

Figure A.3 Same as Fig. A.1 for the galaxy 01h-3517 at $z = 0.635$.

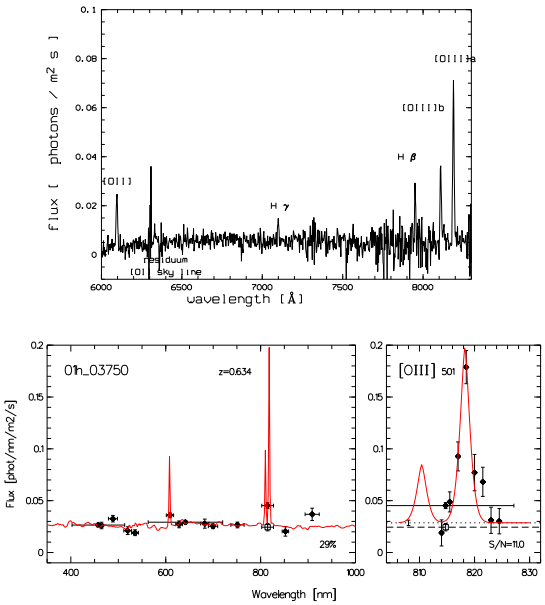

Figure A.4 Same as Fig. A.1 for the galaxy 01h-3750 at $z = 0.635$. The VLT spectra was taken with the 300I grism.

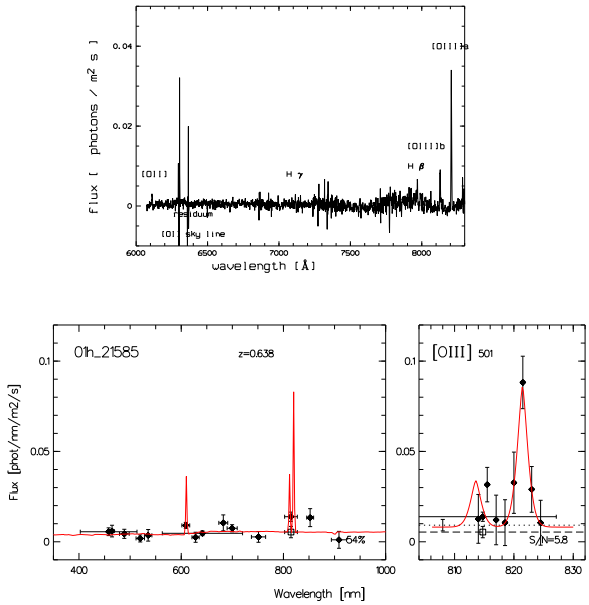

Figure A.5 Same as Fig. A.1 for the galaxy 01h-21585 at $z = 0.639$. The VLT spectra was taken with the 600RI grism.

Spectra 23H-Field

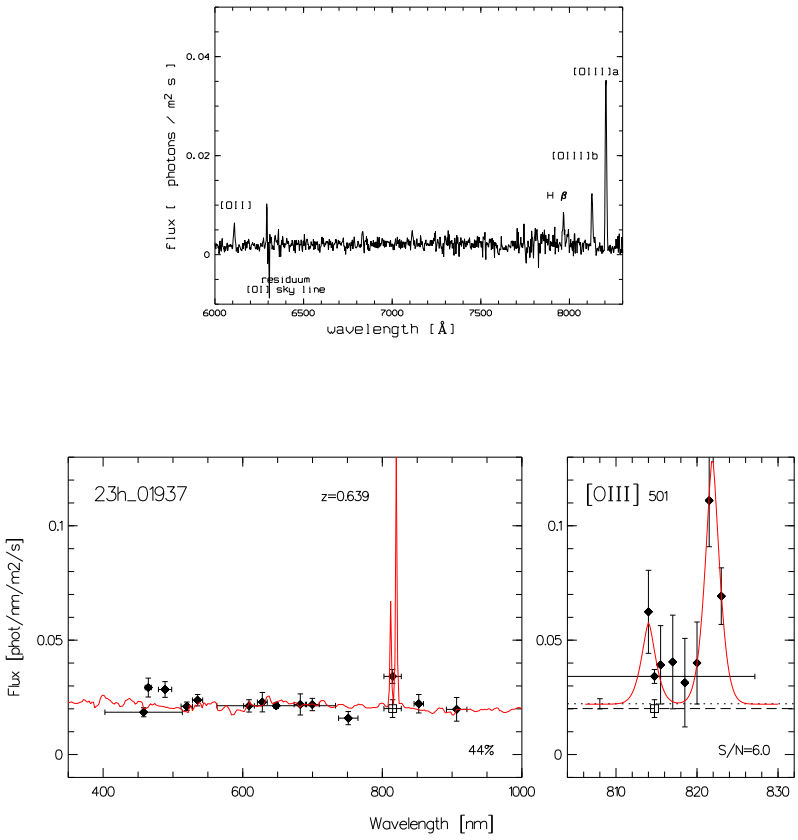

Figure A.6 Same as Fig. A.1 for the galaxy 23h-1937 at $z = 0.639$. The VLT spectra was taken with the 300I grism.

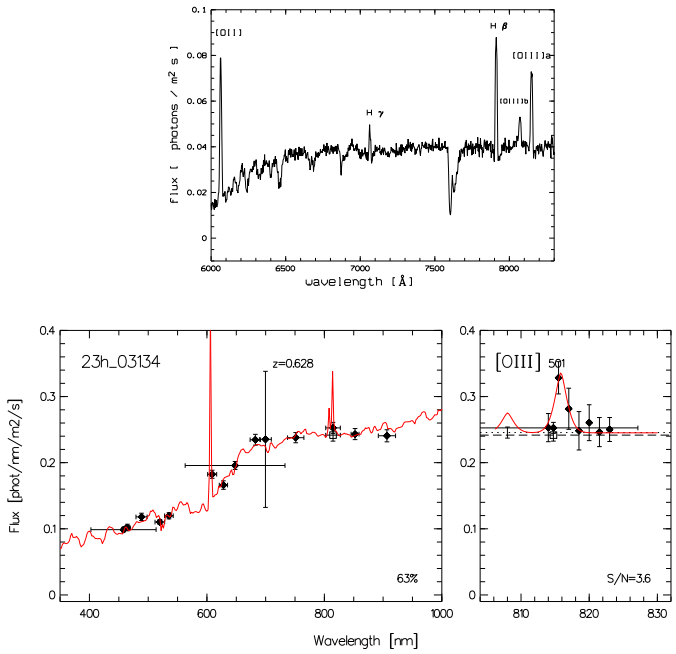

Figure A.7 Same as Fig. A.6 for the galaxy 23h-3134 at $z = 0.628$.

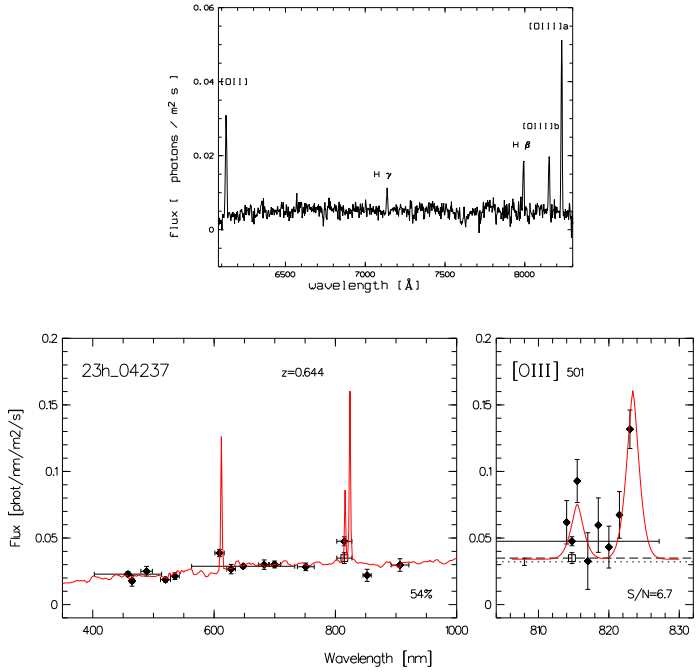

Figure A.8 Same as Fig. A.6 for the galaxy 23h-4237 at $z = 0.644$.

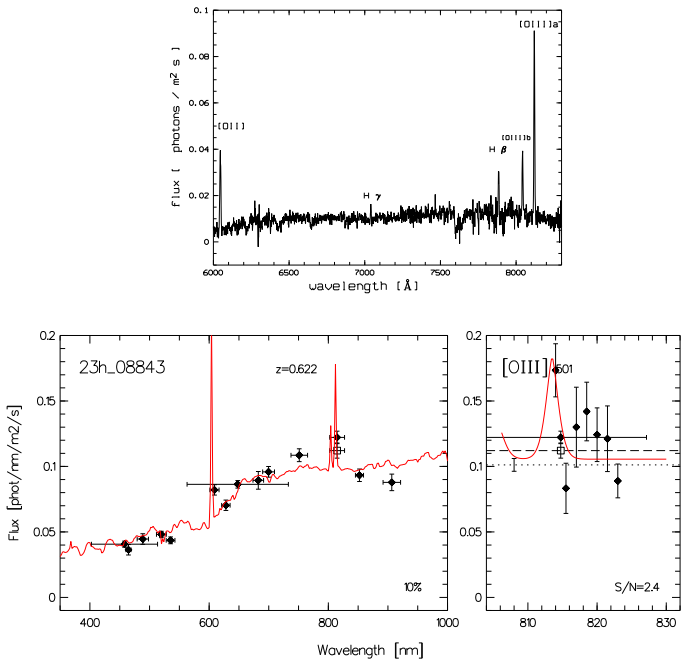

Figure A.9 Same as Fig. A.6 for the galaxy 23h-8843 at $z = 0.622$. The VLT spectra was taken with the 600RI grism.

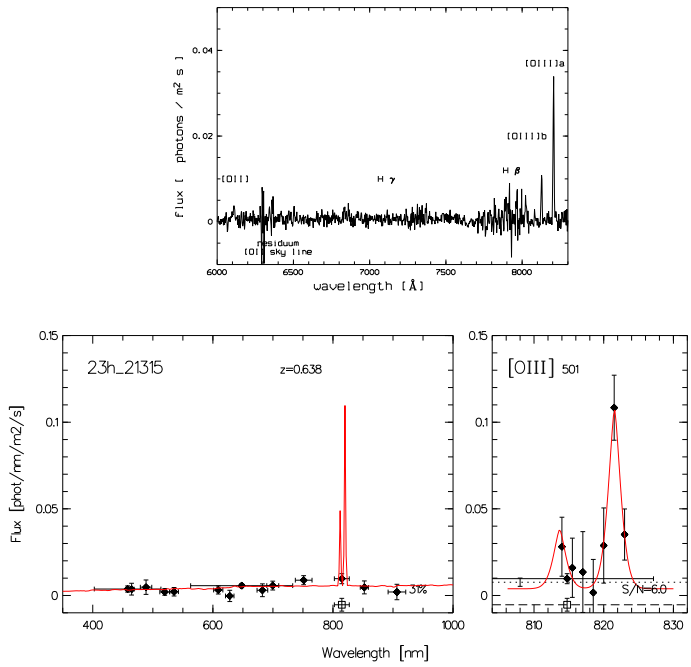

Figure A.10 Same as Fig. A.6 for the galaxy 23h-21315 at $z = 0.639$.

Spectra 09H-Field

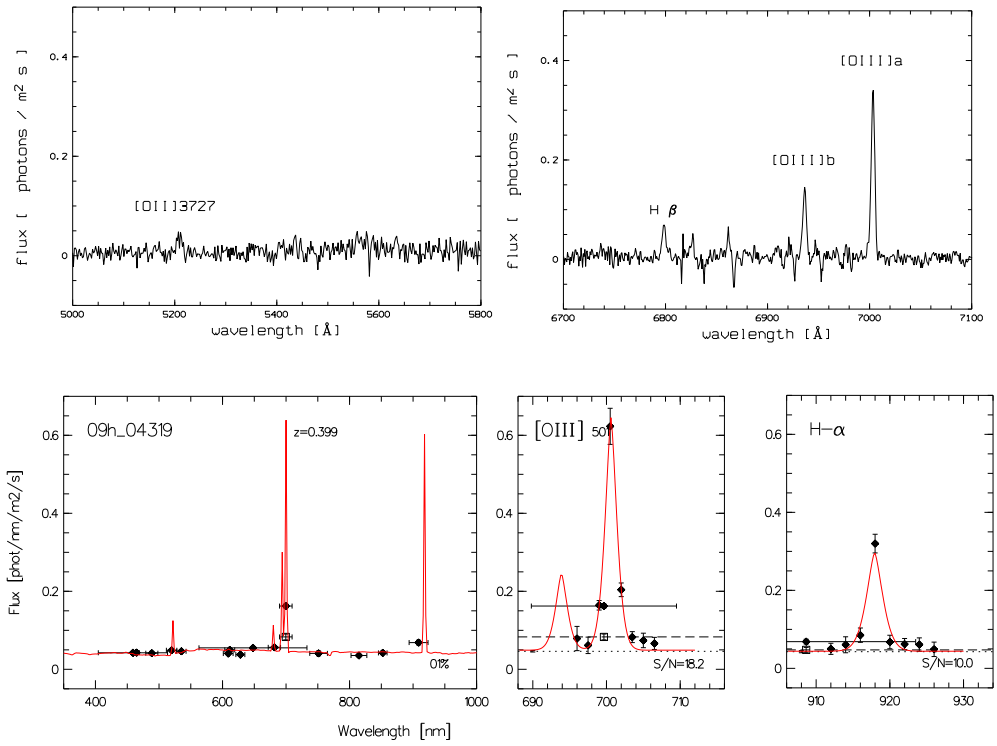

Figure A.11 The galaxy 09h-4319 at $z = 0.399$. **Upper panel**: The GALILEO spectra taken with DOLORES and the HR-R and MR-B grisms. **Lower panel**: Photometry in all 14 optical CADIS filters fitted by a continuum-model (left), the Fabry-Perot measurements in window A with an [O III] doublet profile fitted to the observed flux data (center) and the Fabry-Perot measurements in window C with a Hα profile fitted to the observed flux data (right)

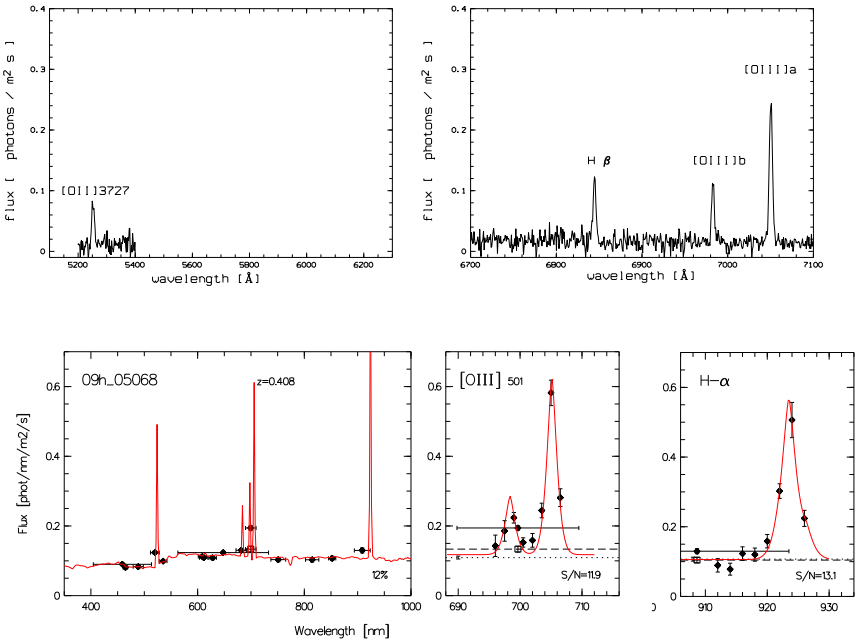

Figure A.12 Same as Fig. A.11 for the galaxy 09h-5068 at $z = 0.409$.

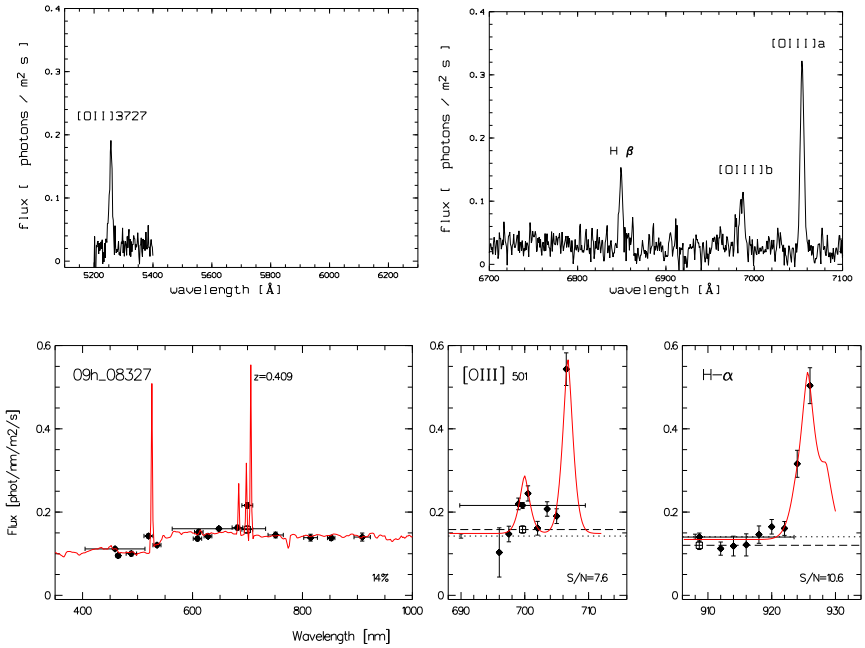

Figure A.13 Same as Fig. A.11 for the galaxy 09h-8327 at $z = 0.409$.

Appendix B
Some Formula

B.1. Deriving the Star Forming Rate from the Ly-α Line

Assuming Case B recombination gives (Brocklehurst 1971):

$$L(\mathrm{Ly}\alpha) = 8.7 \times \mathrm{L}(\mathrm{H}\alpha) \tag{B.1}$$

As shown by Kennicutt (1983), the total number of ionizing photons from newly produced stars is a good measure of the current star formation in a galaxy. Using the Kennicutt translation of $\dot{M}$ from Hα luminosity

$$\dot{M} = SFR = \frac{L(\mathrm{H}\alpha)}{1.12 \times 10^{34}\,\mathrm{W}} M_{\odot}\mathrm{yr}^{-1} \tag{B.2}$$

gives

$$\dot{M} = \frac{L(\mathrm{Ly}\alpha)}{10^{35}\,\mathrm{W}} M_{\odot}\mathrm{yr}^{-1} \tag{B.3}$$

Using updated evolutionary track, and assuming case B recombination and for a Salpeter IMF, Kennicutt (1998) derived a (from equation B.2 slightly different) conversion factor for integral Hα luminosity to star formation rate of

$$SFR = \frac{L(\mathrm{H}\alpha)}{1.27 \times 10^{34}\,\mathrm{W}} M_{\odot}\mathrm{yr}^{-1} \tag{B.4}$$

B.2. Look Back Time

In the standard model the look back time is (from Longair 1998):

$$t(z) = -\frac{1}{H_0} \int_z^0 (1+z)^{-2} (\Omega_0 z + 1)^{-1/2} dz \tag{B.5}$$

For $\Omega_0 = 1$

$$t(z) = \frac{2}{3H_0}(1 - (1+z)^{-3/2}) \tag{B.6}$$

For $z \to \infty$ equation B.6 delivers the age of the universe, $\frac{2}{3\,H_0}$.

For a flat universe ($\Omega_0 + \Omega_\Lambda = 1$) the look back time is:

$$t(z) = 1 - \frac{2}{3\mathrm{H}_0\Omega_\Lambda^{1/2}} \ln\left(\frac{1+\cos\theta}{\sin\theta}\right), \tag{B.7}$$

where $tan\theta = \left(\frac{\Omega_0}{\Omega_\Lambda}\right)^{1/2}(1+z)^{3/2}$.
The present age of the Universe is then:

$$t_{Universe} = \frac{2}{3\mathrm{H}_0\Omega_\Lambda^{1/2}} \ln\left(\frac{1+\Omega_\Lambda^{1/2}}{(1-\Omega_\Lambda)^{1/2}}\right) \tag{B.8}$$

For $H_0 = 70$ km s^{-1} Mpc^{-1}, $\Omega_0 = 0.3$, $\Omega_\Lambda = 0.7$, the present age of the universe is ≈ 13.4 Gyrs.

B.3. Luminosity Distance

The luminosity distance, D_L, is given in the standard model by:

$$\begin{aligned} D_L(z, H_0, q_0) &= \frac{c}{H_0} \cdot \frac{1}{q_0^2} \cdot (zq_0 + (q_0 - 1) \cdot (-1 + \sqrt{2q_0 z + 1})) \\ &= D_P(z, H_0, q_0) \cdot (1+z) \end{aligned} \tag{B.9}$$

where $D_P(z, H_0, q_0)$ is the proper distance.

For a flat universe ($\Omega_0 + \Omega_\Lambda = 1$), D_L is given by:

$$D_L = \frac{c}{H_0} \int_0^z [(1+z)^2(1+\Omega_0 z) - z(2+z)\Omega_\Lambda]^{-1/2} dz. \tag{B.10}$$

B.4. Actual Size of Apparent Angle θ at Redshift z

The proper length d of an objects at redshift z is (from Longair 1998)

$$d = D_P R(t) \Delta\theta = \frac{D_P \Delta\theta}{1+z} = \frac{D_L \Delta\theta}{(1+z)^2} \tag{B.11}$$

d in kpc/arcsec is then given by

$$\begin{aligned} d &= \frac{D_L}{(1+z)^2} \cdot \frac{1000 \cdot 2\pi}{60 \times 60 \times 360} \\ &\approx \frac{D_L}{(1+z)^2} \cdot \frac{1000}{206265}. \end{aligned} \tag{B.12}$$

List of Figures

List of Tables

References

Ajiki, M., Taniguchi Y., Murayama T. et al. 2002, ApJ, 576, 25
Babul A. & Rees M.J. 1992, MNRAS, 255, 346
Balzano, V.A. 1983 ApJ, 268, 602
Bell E. F. & Roelof S.J. 2001 ApJ, 550, 212
Bertin, E. & Arnouts, S, 1996, A&A, 117, 393
Brocklehurst M. 1971 MNRAS, 153, 471
Carollo C. M. & Lilly S. J. 2001, ApJ, 548, 153
Charlot, S. & Fall, S., 1993, ApJ, 415, 580
Contini T., Treyer M. A., Sullivan M. & Ellis R. S. 2002, MNRAS, 330, 75
Cowie, L.L., Hu, E.M., Songaila, A., Egami, E. 1997, ApJ, 481, L9
Cowie L. L. & Hu E. M. 1998, AJ, 115, 1319
Dawson, S., Spinrad, H., Stern, D. et al. 2002, ApJ, 570, 92
Denicolo G., Terlevich R. and Terlevich E. 2002, MNRAS, 330, 69
De Robertis M. M., Dufour R.J. and Hunt R. W. 1987, JRASC, 81, 195
Dey, A., Spinrad, H., Stern, D., Graham, J. R. & Chaffee, F. H., 1998, ApJ, 498, 93
Ellis, R., Santos, M. R., Kneib, J. -P., & Kuijken, K. 2001, ApJ, 560, 119
Fan, X., Narayan, V. K., Lupton, R. H. et al. 2001, AJ, 122, 2833
Fan, X., Narayanan V. K., Strauss, M. A. et al. 2002, AJ, 123, 1247
French, H. 1980, ApJ, 240, 41
Friaça, A.C.S. & Terlevich, R.J., 1999, MNRAS, 305, 90
Fried, J.W., von Kuhlmann, B., Meisenheimer, K. et al. 2001, A&A, 367, 788
Gallego, J., Zamorano, J., Aragon-Salamanca, A., Rego, M. 1995, ApJ, 455, L1
Garnett D. R., Shields G. A., Skillman E. D., Sagan S. P. & Dufour R. J. 1997, ApJ, 489, 63
Garnett D., Lectures Winter School Teneriffe 2001
Grevesse, N., Noels, A., Sauval, A. J. 1996. Standard Abundances; in S. S. Holt and G. Sonneborn (Eds.), *Cosmic Abundances: Proceedings of the 6th annual October Astrophysics Conference*, Volume 99 of *A.S.P. Conference Series*, p.117. San Francisco: Astron. Soc. of the Pacific
Haiman Z. & Spaans M. 1999, ApJ, 518, 138
Hammer F., Gruel N., Thuan T. X. and Infante L. 2001, ApJ, 550, 570
Hamuy, M., Walker, A. R., Suntzeff, N. B. et al. 1992, PASP 104, 533
Hamuy, M, Suntzeff, N. B., Heathcote, S. R. et al. 1994, PASP 106, 566
Hensler G., Rieschick A. & Koeppen J. 1999, ASP Confernece Series
Horne K. 1986, PASP, 98, 609

Hu, E. M., Cowie, L. L. & McMahon, R. G., 1998, ApJ, 502, 99
Hu, E. M., McMahon, R. G., & Cowie, L. L. 1999, ApJ, 522, 9
Hu, E. M., Cowie, L. L., McMahon, R. G. et al. 2002, ApJ, 568, 75
Huang, J. -S., Thompson, D., Kuemmel, M. et al. 2001, A&A, 368, 787
Hummer D. G. & Storey P. J. 1987, MNRAS, 224, 801
Hunter D. A. & Hoffman L. 1999, AJ, 117, 2789
Izotov Y. I., Lipovetsky V.A., Guseva N. G., Kniazev A.Yu & Stephanian J.A. 1991, A&A, 247, 303
Izotov Y. I., Thuan Trinh T. & Lipovetsky V. A. 1994, ApJ, 435, 647
Jansen, R.A., Franx, M., Fabricant, D. 2001, ApJ, 551, 825
Kauffmann G. & Charlot S. 1998, MNRAS, 297, 23
Kennicutt, R. C., Jr. 1983, ApJ, 272, 54
Kennicutt, R. C., Jr. 1998, ARA&A, 36, 189
Kinney, A.L., Calzetti, D., Bohlin, R. et al. 1996, ApJ, 467, 38
Kobulnicky H. A. & Koo D. C. 2000, ApJ, 545, 712
Kobulnicky H. A., Kennicutt R. C. Jr. & Pizagno J. L. 1999, ApJ, 514, 544
Kobulnicky H. A. & Zaritsky D. 1999, ApJ, 511, 118
Kobulnicky H. A. & Skillman E. D. 1996, ApJ, 471, 211
Kudritzki, R.-P., Mendez, R. H., Feldmeier, J. J. et al. 2000, ApJ, 536, 19
Leitherer, C., Robert, C., & Heckman, T. M., 1995a, ApJS, 99, 173
Leitherer, C., Ferguson, H. C., Heckman, T. M. & Lowenthal, J. D. 1995b, ApJ, 454, 19
Lennon, D.J. & Burke, V. M. 1994, A&AS, 103, 273
Lequeux, J., Rayo. J. F., Serrano, A., Peimbert, M.& Torres-Peimbert S. 1979, A&A, 80, 155
Longair, M. S. 1998, *Galaxy formation*
Madau, P. 1995, ApJ, 441, 18
Malhotra S. & Rhoads J. E. 2002, ApJ, 565, 71
McCall L. M. 1984, MNRAS, 208, 253
McCall L. M., Rybski P. M. & Shields G. A. 1985, ApJS, 57, 1
McGaugh, Stacy 1991, ApJ, 380, 140
McLow, M. & Ferrara, A. 1999, ApJ, 513, 142
Melbourne, J. & Salzer, J. J. 2002, AJ, 123, 2302
Meisenheimer, K. & Röser, H.-J. 1993, in Landolt-Börnstein, Extension and Supplement to Volume 2, Subvolume a, 29 (Springer Verlag)
Meisenheimer, K., Beckwith, S., Fockenbrock, H. et al. 1998 in *The Young Universe: Galaxy Formation and Evolution at Intermediate and High Redshift.* Edited by S. D'Odorico, A. Fontana, and E. Giallongo. ASP Conference Series, Vol. 146, p.134
Meisenheimer, K. et al. *The Calar Alto Deep Imaging Survey: Concept, Data Analysis and Calibration*, to be submitted 2002
Miller, J. S. & Mathews, W. G. 1972, ApJ, 172, 593
Oke, J. B. 1990, AJ, 99, 1621
Osterbrock, D.E. 1989, Astrophysics of Gaseous Nebulae and Active Galactic Nuclei (Mill Valley: University Science Books)
Osterbrock, D. E., Fulbright, J. P., Martel, A. R. et al. 1996, PASP, 108, 277
Ouchi M., Shimasaku, K., Furusawa, H. et al. 2002, submitted (astro-ph/0202204)

Pagel B. E. J., Edmunds M. G., Blackwell D. E., Chun M. S. & Smith G. 1979, MNRAS, 189, 95
Pagel B. E. J., Simonson E. A., Terlevich R. J. & Edmunds M. G. 1992, MNRAS, 255, 325
Pei, Y.C., Fall, M. & Hauser M.G. 1999, ApJ, 522, 604
Pettini, M., Steidel, C. C., Adelberger K. L. et al., 1997, "ORIGINS", ed. J.M. Shull, C.E. Woodward, and H. Thronson, (ASP Conference Series) (astro-ph/9708117)
Pilyugin, L.S. 2000, A&A, 362, 325
Pilyugin, L.S. & Ferrini, F. 2000, A&A, 358, 72
Pentericci, L., Fan, X., Rix, H.-W. et al. 2002, AJ, 123, 2151
Popescu, C. C. & Hopp, U. 2000, AASS, 142, 247
Rhoads, J. E., Malhotra, S., Dey, A. et al. 2000, ApJ, 545, 85
Rhoads, J. E. & Malhotra, S. 2001, ApJ, 563, 5
Richer, M. G. & McCall, M. L. 1995, ApJ, 445, 642
Schechter, P. 1976, ApJ, 203, 297
Shaw, R. D. & Dufour, R. J. 1995, PASP, 107, 896
Shields, G. A. ARAA, 1990, 28, 525
Skillman, E. D. & Kennicutt, R C. Jr. 1993, ApJ, 411, 655
Skillman, E. D., Kennicutt, R C. & Hodge, P.W. 1989, ApJ, 347, 875
Spinrad, H., Stern, D., Bunker, A. et al. 1998, AJ, 116, 2617
Stasinska, G. & Leitherer, C. 1996, ApJS, 107,661
Steidel, C. C., & Hamilton, D. 1992, AJ, 104, 941
Steidel, C. C., & Hamilton, D. 1993, AJ, 105, 2017
Steidel, C. C., Giavalisco, M., Dickinson, M. & Adelberger 1996, AJ, 112, 352
Steidel, C. C., Adelberger, K. L., Dickinson, M. et al. 1998, ApJ, 492, 428
Steidel, C. C., Adelberger, K. L., Giavalisco, M., Dickinson, M. & Pettini, M. ApJ, 1999, 519, 1
Tegmark, M., Silk, J., Rees, M. J. et al. 1997, ApJ, 474, 1
Telles, E. & Terlevich, R. 1997, MNRAS, 286, 183
Thommes, E & Meisenheimer, K. 1995, *Number density predictions for primeval galaxies.* In Hippelein et al. (eds.): "Galaxies in the Young Universe", Springer Lect. Notes 463, 242
Thommes, E. & Meisenheimer, K., to be submitted 2002
Thurston, T. R., Edmunds, M. G. & Henry, R. B. C., 1996, MNRAS, 283, 990
Tresse, L. & Maddox, S.J. 1998, ApJ, 495, 691
van Breugel, W. J. M., de Breuck, C., Stanford, S. A. et al. 1999, ApJ, 518, 61
Veilleux, S., Osterbrock, D.E. 1987, ApJS, 63, 295
Vogel, S., Engels, D., Hagen, H.-J. et al. 1993, A&AS, 98, 193
Weymann, R. J., Stern, D., Bunker, A. et al. 1998, ApJ, 505, 95
Whitford, A. E., 1958, AJ, 63, 201
Wolf, C., Meisenheimer, K., Röser, H.-J. et al. 2001, A& A, 365, 681
Yan, L., McCarthy, P.J., Freudling, W. et al. 1999, ApJ, 519, L47
Zaritsky, D., Kennicutt, R.C. & Huchra, J.P. 1994, ApJ, 420, 87
Zaritsky, D., Smith, R., Frenk, C.S. & White, S. D. M. 1998, ApJ, 478, 53

Danksagung

Ich danke...

meinem Betreuer Dr. Klaus Meisenheimer für die spannenden Aufgabenstellungen, für die Betreuung, sowie für die Hilfe, wie man Anträge schreibt

Herrn Prof. Dr. Immo Appenzeller für das Anfertigen des Zweitgutachtens

Hans H. Hippelein für die Hilfe bei der Doktorarbeit, Anträge schreiben, weitere hilfreiche Diskussionen

Henry, Dan, David, Andrea, Stefan U. für das Korrekturlesen

Adrianne, Thilo, Greg, Roland, Stefan U., Mark für die gute Büroatmosphäre

den Nachtassistenten auf dem Calar Alto (besonders Jesus A. und Alberto A.), an der Telescopio Nazionale Galileo auf La Palma und an dem VLT (Yepun) für die Unterstützung, die ich erhalten habe

Francisco Paco Prada für die erfolgreiche Kollaboration für einen Beobachtungsantrag an TNG

Roberto S., Carlos, Elena d'O., Gerhard, Angela, Bernd L., Giorgio, Elena T., Anna G. für schöne Stunden in der Freizeit, die neue Motivation für die Arbeit gebracht haben

meinen Eltern für finanzielle Unterstützung und aufmunternde Telephongespräche

and last but not least Anita, für die schönen Stunden an den Wochenenden, für aufmunternde Worte und die schönen Urlaubstagen nach anstrengenden (aber faszinierenden) Beobachtungsnächten in Andalusien, in Chile und auf La Palma.